Helium Bubbling in the Molten Salt Fast Reactor

An experimental and analytical analysis of particle entrainment in a flotation column

Ies Lakerveld

A thesis presented for the degree of
Master of Science

Student number:	4317769	
Project duration:	October 14th, 2020 - June 14th, 2021	
Defence date:	July 9th, 2021	
Thesis committee:	Dr. ir. M. Rohde	TU Delft, supervisor
	Dr. ir. D. Lathouwers	TU Delft
	Dr. S.R. de Roode	TU Delft

Transport Phenomena in Nuclear Applications
Delft University of Technology
The Netherlands
July 5th 2021

Word of Thanks

This section provides a list of people that have contributed greatly to the research that is presented in this report. Bouke Kaaks helped to familiarize with the Davis software that has played such an important role in the bubble detection and particle extraction measurements. John Vlieland and Dick de Haas were always available to assist with technical problems regarding the equipment, but also helped to improve the measurement setup. As NRG has taken an interest in this research subject, Edo Frederix has been very helpful when discussing the comparison of experimental data with numerical simulations. Martin Rohde, supervising the project, has kept me sharp throughout this research via weekly meetings and always asking the 'why'. Alex Nila from LaVision has guided me through the immense variety of options in the DaVis menu, and has pointed out how to carefully carry out all the imaging processing steps in the right order. A special thanks goes to Thomas Dumaire for being so helpful in all stages of the project, especially providing tips on the direction of the research, preparing samples for the experiments and understanding of the DaVis software.

Abstract

World-wide energy demands are ever increasing and is one of the main challenges of this age. The emission of greenhouse gases through the burning of fossil fuels poses serious problems to the environment and has raised the awareness of renewable energy sources. One source that is often excluded in the list of emission-free alternatives is nuclear energy. Electricity from nuclear power plants is generated through the fission of fissile materials, such as uranium, and does not involve the burning of material of any kind. The MSFR (Molten Salt Fast Reactor) is a Generation IV reactor under investigation in this research. It is part of the SAMOSAFER (Severe Accident MOdelling and Safety Assesment for Fluid-fuel Energy Reactors) project and is connected to many universities, institutions and companies all over the world. The grand objective is that the Molten Salt Reactor can comply with all expected regulations in 30 years' time.

The aim of this research is to investigate one safety aspect of the MSFR, namely the removal efficiency of unwanted metallic nanoparticles that are created during a fission reaction through a process known as helium bubbling. These particles could be poisonous for the reaction and plate out on the cold parts of the reactor core, causing corrosion. To test the particle removal efficiency, or collection efficiency, an experimental bubble facility is available where the interaction between air bubbles and fluorescent polystyrene particles is studied. The method of the measurements is based on the Laser Induced Fluorescence (LIF) technique, meaning a laser beam is formed to a light sheet that intersects the fluid area of interest. The resulting fluorescent light from excited particles in the light sheet is imaged through a selective filter onto a time-gated digital camera and after calibration is monitored to determine the particle concentration during the bubbling process.

The results show that for different nanoparticle sizes in a viscous aqueous glycerol solution a decreasing concentration during a bubbling time of one hour cannot be clearly observed. Moreover, the evolution of bubbles is found to increase over the measurement period. This could counter the expected decrease of particle concentration due to an increment of bubble surface reflections adding to the measured intensity. Finally, experimental results in water are compared to a bubble-particle interaction model that slightly overestimates the experimental data.

Contents

1 Introduction

The introductory chapter of this report is divided into three parts. Firstly, some background information about nuclear energy is given in Chapter 1.1. Secondly, in Chapter 1.2 the operation of the reactor under investigation is explained. Thirdly, Chapter 1.3 concludes the introduction by discussing the specific topic of this research, namely helium bubbling.

1.1 Nuclear energy

Since the discovery of nuclear fission in December 1938 by Otto Hahn, it only took four years before the first nuclear reactor was established. The reactor was built underneath the University of Chicago's First Stagg Field stadium. On December 2$^{\text{nd}}$ 1942, Enrico Fermi and 48 of his colleagues succeed in achieving in this reactor the world's first man-made controlled nuclear chain reaction, thereby establishing the ability of mankind to control the release of nuclear energy [1]. Ever since a lot of research has been conducted to investigate both efficiency and safety of energy production through fission. In this section the physics of nuclear energy and its impact on the environment is discussed.

1.1.1 Nuclear physics

Nuclear energy produces power generated through fission. This is an exothermic reaction where a nucleus of an atom splits into two or more smaller nuclei. The starting point of the most commonly used nuclear fission is an isotope of uranium, U-235. The fission reaction of U-235 is synthesized as follows:

$$^{235}\text{U} + \text{n} \rightarrow \text{X} + \text{Y} + \nu\text{n} + E_k \tag{1}$$

This reaction has some important implications. First of all, the fission products X and Y emerge with very large kinetic energy E_k, about 200 MeV. The kinetic energy is converted into heat as the fission products slow down by banging into neighboring atoms in the reactor fuel [2]. The heat released by fission is used to create steam that spins a turbine to generate electricity. The second important implication is that because neutrons appear on both sides of the reaction, they can be used to propagate a chain reaction. Since usually between two and three neutrons ν are produced during each fission event, there are more than enough neutrons available to sustain the chain reaction. However, most neutrons don't result in another fission, which makes it difficult to keep the reaction going. Two other possible reactions that occur are the capture of a neutron by a nucleus and the neutron scattering off of a nucleus, with a chance of it eventually leaking out of the reactor core. Keeping track of the neutron economy is one of the primary tasks when dealing with nuclear energy.

The most widely used isotope for powering a nuclear reactor is U-235. U-235 is the part of the fuel that is fissile but does not occur freely in nature. Naturally occurring uranium ore is composed of three isotopes: U-238 (99.27%), U-235 (0.71%) and U-234 (0.005%) [3]. The most abundant isotope, namely U-238, is fissionable but non-fissile. 'Fissile' is distinct from 'fissionable'. The term fissionable is referred to as a nuclide that is capable of undergoing fission after capturing high-energy (fast) neutrons, while a fissile nuclide undergoes fission with low-energy (thermal) neutrons. To illustrate the difference, Figure 1 below depicts the fission cross-sections of three isotopes of uranium and one isotope of plutonium as a function of the neutron energy. The fission cross-section of a nuclide is used to describe the probability that a fission will occur. The concept can be quantified physically in terms of 'characteristic area', where a larger area means a larger probability of interaction.

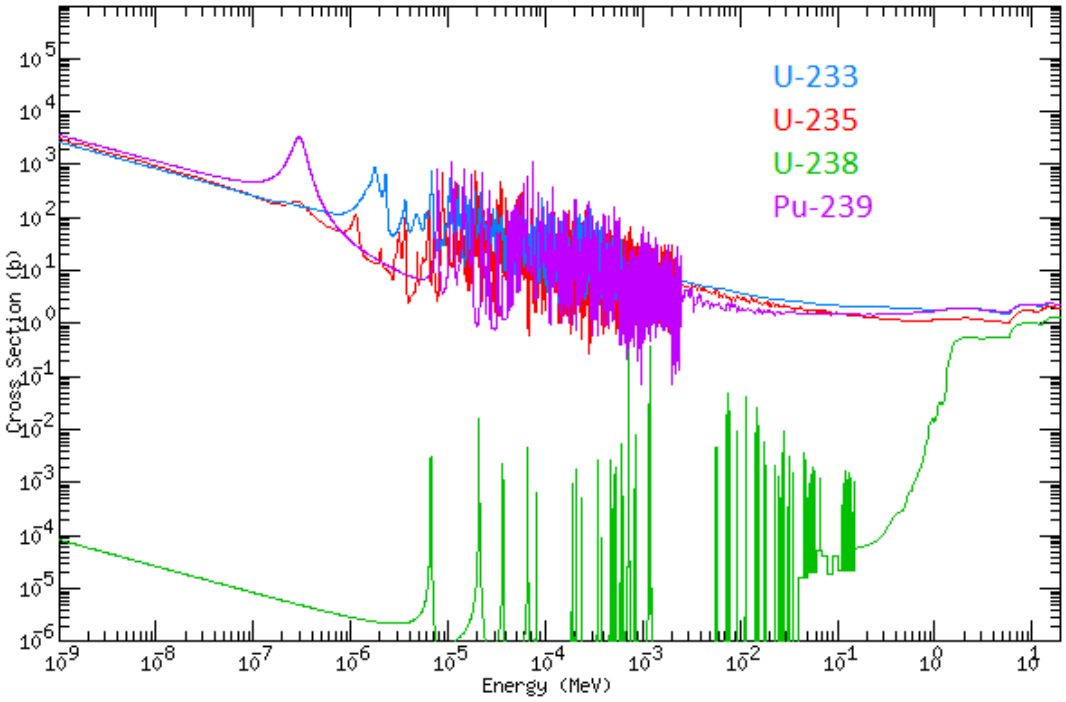

Figure 1: Graph of the fission cross-sections of three fissile (U-233, U-235 and Pu-239) nuclides and one non-fissile (U-238) nuclide and their behavior for different incident neutron energies. The unit of cross-section is barn (b), corresponding to 10^{-24} cm^2.

A peculiar phenomenon is occurring in the intermediate energy spectrum in Figure 1, denoted as resonances. On the ground of quantum-mechanical considerations, the Breit-Wigner equation relates the cross-section to the neutron energy for a single resonance, but will not be discussed here. It is important to note that the fission cross-section of the fissile isotopes is proportional to the reciprocal of the square root of the neutron energy [2], meaning that the more energy the neutron carries, the lower the probability a fission event will take place.

To produce a sufficient amount of energy, most present-day nuclear reactors use U-235 in the thermal neutron energy spectrum [4]. In Light Water Reactors (LWRs), water serves as coolant and moderator, where the task of the moderator material is to slow down the fast neutrons created in equation (1) to enhance the fission process and increase heat production. However, the 0.71% U-235 existing in the mined uranium ore is too low a concentration to be effectively used as nuclear fuel. A process called enrichment is necessary to increase the proportion in the fuel rods [5].

1.1.2 Impact on the environment

From all the renewable energy sources, nuclear energy is probably the most unpopular and often not even listed as one. The first thing that comes to mind is the disaster at Chernobyl on April 26$^{\text{th}}$ 1986. Although it is not known how many people died as a result of the incident, it is estimated that there have been as many as 10,000 deaths from the long-term effects of radiation in the region [6]. The Fukushima power plant crisis in 2011 showed that no matter how safe nuclear power plants are designed to be, accidents can happen, in this case due to extreme weather conditions.

Even though the fission process is carbon-free and produces heat without the harmful byproducts emitted by fossil fuels [7], nuclear energy does have an impact on the environment. The mining and enrichment of uranium are not environmentally friendly processes. Open-pit mining does not produce a massive amount of radioactivity but leaves behind radioactive particles, causes erosion, and even pollutes nearby sources of water. Underground mining isn't much better and exposes miners to high amounts of radiation while producing radioactive waste rock during extraction and processing [6].

These are just some of the downsides, others being the expense to build a reactor, safe storage of

radioactive waste and security threat. Despite these side effects, nuclear energy's land footprint is small, producing more electricity on less land than any other clean-air source. A typical 1000 MW nuclear facility in the United States needs 3.4 km^2 to operate. Wind farms require 360 times more land area to produce the same amount of electricity and solar photovoltaic plants require 75 times more space. To put that in perspective 3 million solar panels would be needed to produce the same amount of power as a typical commercial reactor or more than 430 wind turbines [8]. Moreover, nuclear fuel is extremely energy dense, with one uranium fuel pellet creating as much energy as one tonne of coal [9]. Furthermore, the NEA (Nuclear Energy Agency) and the IAEA (International Atomic Energy Agency) identified that natural uranium resources that can be recovered amount to 8,070,400 tonnes as of January 1st 2019 [10]. The gradient of the total recoverable uranium supply and the exploration costs over time are displayed in Figure 2. This graph implicates that starting in 2003 nuclear growth caused a strong upward movement in world uranium prices, but went into a downward correction, accentuated by the Fukushima accident in 2011. Since the accident, uranium prices have fallen to one of the lowest inflation-adjusted levels ever experienced [11].

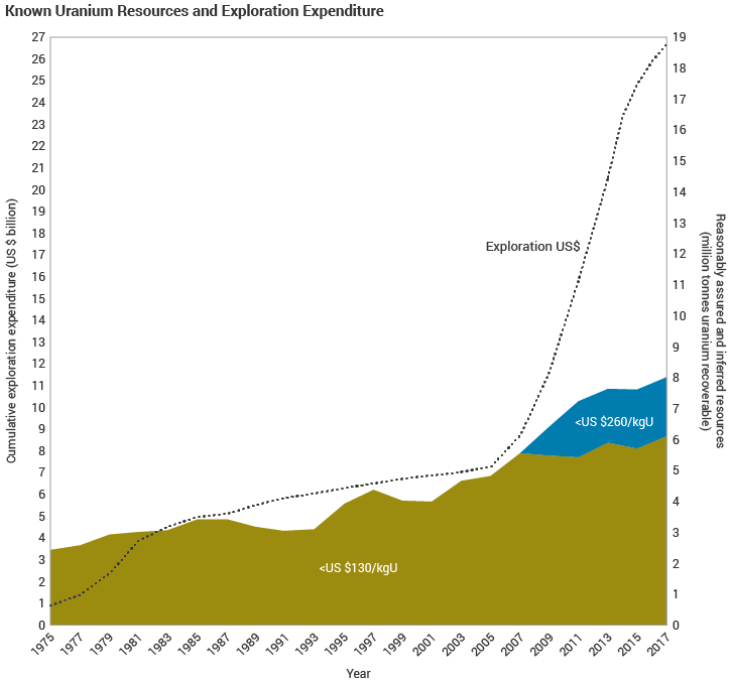

Figure 2: Exploration costs incurred for the search of uranium resources and total recoverable uranium supply over time [11].

With present-day reactors requiring roughly 70,000 tonnes of natural uranium annually worldwide, the accessible resources are sufficient for reactors to run more than 100 years at current rates of consumption. Extraction of uranium from seawater and fuel-recycling fast-breeder reactors could greatly extend the recoverable uranium supply, however neither technology is economically feasible at present [12]. Summarizing, there are a lot of hurdles to overcome, but nuclear energy is an attractive long-term investment.

1.2 Molten Salt Reactor

The Molten Salt Reactor (MSR) is a thorium based breeder reactor moderated with graphite and has its fuel dissolved in the coolant consisting of liquid fluoride salt. In the 1960s the Molten Salt Reactor Experiment (MSRE) was the first research that has been conducted on this type of reactor and will be briefly discussed in Chapter 1.2.1. Then in Chapter 1.2.2 the loop of the Molten Salt Fast Reactor (MSFR), which is the reactor under current development, will be discussed.

1.2.1 Molten Salt Reactor Experiment

The MSRE took place at the Oak Ridge National Laboratory (ORNL), Tennessee. Motivation for the development of alternative types of reactors arose due to the limited supply of natural uranium [13]. Thorium is a fertile material, meaning it can produce fissile U-233 when colliding with a neutron as can be seen in the chemical reaction below. The isotope Th-232 is used for breeding, the term used for generating more fissile material than is consumed. Breeders were at first found attractive because they made more complete use of uranium fuel than LWRs, but interest declined after the 1960s as more uranium reserves were found and new methods of uranium enrichment reduced fuel costs.

$$ {}^{1}_{0}\mathrm{n} \quad + \quad {}^{232}_{90}\mathrm{Th} \quad \rightarrow \quad {}^{233}_{90}\mathrm{Th} \quad \overset{\beta^-}{\rightarrow} \quad {}^{233}_{91}\mathrm{Pa} \quad \overset{\beta^-}{\rightarrow} \quad {}^{233}_{92}\mathrm{U} \tag{2} $$

Unlike in the U-235 fission chain reaction (1), here the starting point of the reaction is U-233 because of beta minus decay of the unstable isotopes Th-233 and Pa-233 in the breeding process. In the MSRE, the used salt-fuel composition is LiF-BeF_2-ZrF_4-UF_4. It was shown that the UF_4 was chemically stable in the salt and that the gaseous (unwanted) fission products were removed automatically by the circulation pumps [13]. The MSRE had a thermal power of 8 MW and operated either with U-233, U-235 or Pu-239. However, the fuel salt did not contain any thorium, where UF4 was the result of breeding from thorium in other reactors. Since this was an engineering test, the large, expensive breeding blanket of thorium salt was omitted in favor of neutron measurements.

The experience gained was used in the design of the Molten Salt Breeder Reactor (MSBR), which had a large core to reduce neutron leakage and a low power density to reduce irradiation damage to the graphite moderator. To achieve net breeding, the produced U-233 was removed by a method called fluorination, and a process flow sheet was designed to separate the thorium from the lanthanides. The salt loop was connected to a drain tank via a freeze plug made of solid salt cooled by air. This plug could thaw in the events of overheating or operator intervention. Unfortunately, the MSBR was never built and the freeze plug and chemical fuel salt processing were never applied [13].

The most important conclusion of the MSRE was that a molten salt fueled reactor concept is viable. However, the experiment has been carried out for only five years (1964-1969) of the planned thirty-year operation time. Therefore, more investigation into the safety aspects is required.

1.2.2 Molten Salt Fast Reactor loop

The MSFR is the Gen-IV reactor under investigation in this research. It is part of the SAMOSAFER (Severe Accident MOdeling and Safety Assessment for Fluid-fuel Energy Reactors) project of the European Union research and innovation programme Horizon 2020. The project started October 1, 2019 and is connected to many universities, institutions and companies all over the world, including the Nuclear Research and consultancy Group (NRG) and the Delft University of Technology (TUD). The grand objective is to ensure that the MSR can comply with all expected regulations in 30 years' time.

The major difference between the reactor experimented on as part of the MSRE and the MSFR is that in the new design the salt acts as both the coolant and the moderator. By adopting a graphite moderator a thermal neutron spectrum is obtained, while otherwise a fast or epithermal neutron spectrum results [13].

The MSFR consists of a core which is more or less a basin filled with the molten fuel salt. At the top and the bottom, the salt respectively leaves and enters through pipelines which are connected to a heat exchanger that cools down the salt and uses the heat to power turbines that generate electricity. A separate loop is present between the heat exchanger and the energy conversion system. The slightly cooler salt, after passing the heat exchanger, enters the basin again and repeats the cycle [14]. A schematic picture of the MSFR is depicted in Figure 3 below.

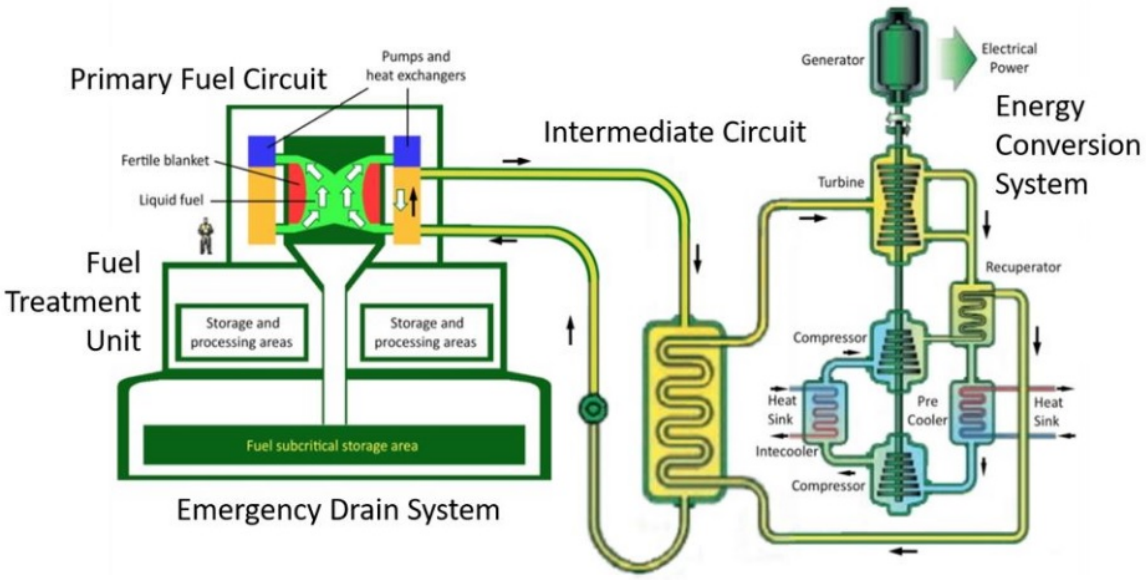

Figure 3: Schematic overview of the various systems in the MSFR [13].

1.2.3 Formed elements in the fuel salt

There is one aspect of the U-235 fission reaction (1) that is not discussed yet, and it has been specifically reserved for this section. It concerns the fission products that are formed. During irradiation, several classes of elements build up in the fuel salt, each one requiring specific treatment. This is indicated in Figure 4 below. The yellow colored elements form fluorides and remain dissolved in the fuel salt during operating conditions. The purple colored elements are the noble metals, which need to be extracted from the fuel salt before they will deposit on the cold parts of the primary circuit (e.g. on the heat exchanger) to prevent corrosion. The investigated process for this is helium bubbling. The blue elements are the Gaseous Fission Products (GFPs), which could be removed from the fuel salt in the helium bubbling process as well. The collection of noble and semi-noble metal particles, GFPs, solid fission products (i.e. Cs, Ba) and corrosion products (such as Cr and Ni) of sub-micron size through helium bubbling is the main interest of this project.

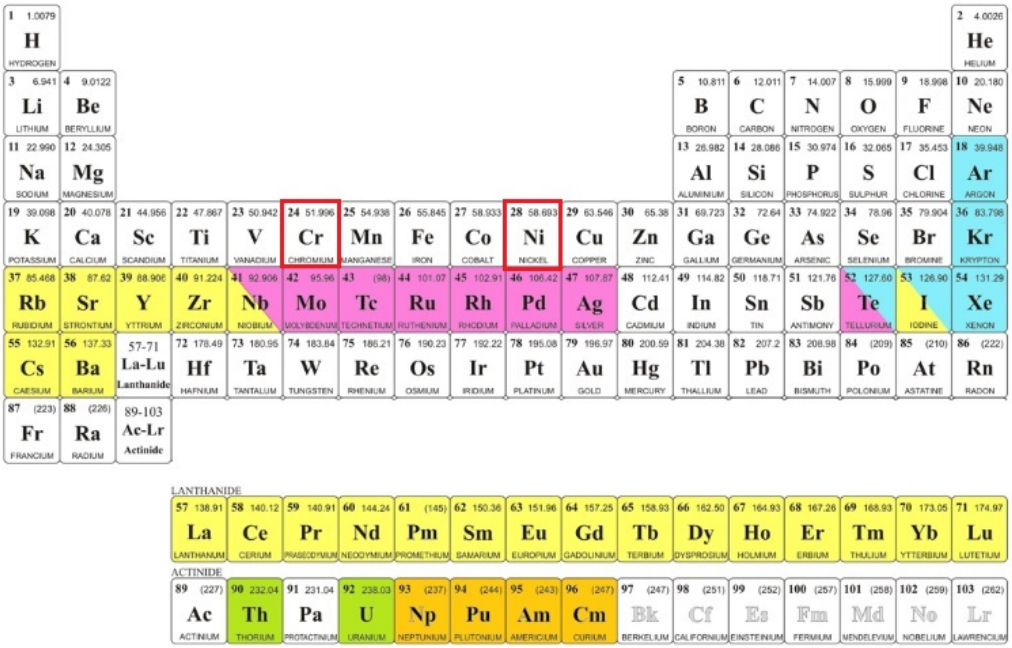

Figure 4: Overview of the elements formed in the fuel salt. Yellow elements remain dissolved in the fuel salt. The noble metals (purple), GFPs (blue) and corrosion products (red) can be removed from the fuel salt via helium bubbling [13].

1.3 Aim of the research

Past attempts to solve this research problem have been carried out by E. Capelli as part of her Post-doc project and L. Rozing for his master thesis project. Capelli studied particle extraction by bubbling of micron sized molybdenum and iron particles [15]. Rozing's research was scheduled to continue and extend the experimental work of Capelli by investigating particles of sub-micron size, but was forced to fall back to a strictly off-campus project due to COVID-19 restrictions. He finished his research by using a two phase Euler method to model the helium bubbling process in OpenFOAM, an open-source computational fluid dynamics program [14].

This master thesis focuses on doing experiments with fluorescent nanoparticles mimicking the noble metal particles and GFPs in the fuel salt, as well as constructing a probabilistic flow model to determine the behaviour of particle-bubble interactions in a fluid. The experimental part of this research will be carried out at the Reactor Institute Delft (RID) and details regarding the measurement setup are explained in Chapter 3.2. The experimental data will serve as a means to validate the model and is further discussed in Chapter 2.2. Moreover, the provided experimental data is used to test numerical models constructed by NRG.

The main research question that I will attempt to answer is the following: How does the recovery efficiency of sub-micron particles change as a function of time and gas flow rate in a bubble column? A large number of parameters make it difficult to answer this question, such as the temperature, pressure, particle/bubble size and velocity, density, viscosity, contact angle, surface tension, hydrophobicity, gas holdup, column geometry and possibly more [14]. It is important to separate the material properties from the flow properties, i.e. the known from the unknown. Furthermore, the flow rate has a direct effect on the flow regime, and in each regime there are different processes that affect the particle extraction efficiency. Finally, the type of simulant fluid is of interest because an experimental setup including the fuel salt composition in the MSFR that operates at temperature $T = 900$ K is not available. For the calibration during the first experiments the fluid will be water. For the final measurements a water-glycerol solution is used as a suitable substitute for the fuel salt [14, 15].

The first step to analyze the recovery process is to accurately measure the position of the particles in the fluid, as well as the sizes of the bubbles for different gas flow rates, and will be the starting point of

this work. This accurate measuring is of crucial importance because bubble-particle interaction depends heavily on their respective sizes [16, 17]. The results of the bubble evolution, particle extraction and the model are presented in Chapter 4.

2 Theory

In order to study the efficiency process of solid particle entrainment by gas bubbles in a liquid, a clear understanding of the flow properties is required. As three different phases play a role, with each having their own characteristics, Chapter 2.1 is devoted to the subject of multiphase flows. In Chapter 2.2 the bubble-particle interaction model that has been chosen to compare the experimental results is discussed.

2.1 Multiphase flows

It has been known for quite some time that bubbles transport from 20 to 50 times more particles then can be transported by average suspension [18]. The impairment of particles through flotation is therefore an effective method. Investigating single phase flows is already a challenging task, but dealing with all three significantly enhances the complexity of the flow. The purpose of this section is to get a better understanding of the problem at hand, making simplifying assumptions to produce some values for comparison of the experimental data that will be discussed in detail in Chapters 3 and 4.

2.1.1 Flow regime

When analyzing properties in fluid mechanics, non-dimensional numbers are often useful to determine the flow characteristics of a fluid. Two of the most commonly known numbers are mentioned here. Let's first discuss the Stokes number, which characterizes the ratio of the inertial forces of a particle to the viscous resistance of the fluid. In the case of a small particle interacting with a bubble, the particle Stokes number K is defined in equation (3):

$$\mathrm{K} = \frac{\rho_p v_b d_p^2}{9\mu d_b} \tag{3}$$

where ρ_p is the density of the particle, v_b is the bubble velocity, μ is the dynamic viscosity of the fluid, and d_p and d_b are the particle and bubble diameter, respectively [19]. In the limit where K is much smaller than unity the particles follow readily the fluid flow including eddy fluctuations. If K is much larger than unity particle inertia is dominant ignoring any fluid fluctuations [20]. In our case using sub-micron particles, it is expected that K is smaller than unity, such that the inertial force of the particles has a negligible contribution.

Also the bubble Reynolds number is of importance, given by the ratio of inertial forces to viscous forces within a fluid and helps predict flow patterns in different fluid flow situations. The bubble Reynolds number Re_b is defined in equation (4):

$$\mathrm{Re}_b = \frac{\rho_l v_b d_b}{\mu} \tag{4}$$

where ρ_l is the density of the liquid and the other parameters as described above. With the help of Re_b, roughly three regimes can be defined as can be seen from equation (5):

$$\begin{cases} \mathrm{Re}_b \ll 1 & \text{Stokes flow} \\ 0.2 < \mathrm{Re}_b < 100 & \text{intermediate flow} \\ \mathrm{Re}_b > 100 & \text{potential flow} \end{cases} \tag{5}$$

Typical bubble Reynolds numbers encountered for the sizes of bubbles employed during flotation fall in the intermediate flow regime [21].

So far, different flow regimes have been discussed using dimensional numbers. This indicates how the phase distributions affect the physical nature of the system. Another way to define flow characteristics is by looking at the flow pattern. This indicates the visible distribution or structure of the phases, in this case between the gas and the liquid. In Figure 5 different flow patterns are shown as a function of

the superficial gas and liquid velocities v_{sg}, v_{sl} in a vertical column, the definition of which is given at the end of Chapter 2.1.2.

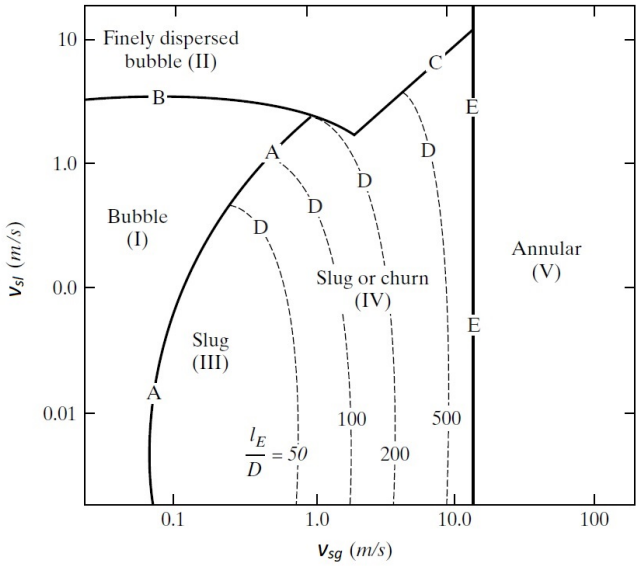

Figure 5: Flow pattern transition lines for upward, cocurrent flow in vertical tubes, 5 cm in diameter [22].

The desired flow pattern is bubbly flow, which occurs at low gas velocities where very small bubbles ($d_b < 1.5$ mm) behave like rigid spheres rising in a rectilinear motion. Larger bubbles ($d_b > 1.5$ mm) rise on randomized trajectories and may coalesce, forming even larger bubbles [20]. Because of this coalescence, the formation of larger bubbles results in a relatively smaller total surface area compared to smaller bubbles so that particles have a lower probability of interacting with the bubbles, and therefore a lower collection efficiency. In Figure 6 below the behaviour of bubbles for the different flow patterns are shown as a function of the volumetric gas flow rate Q_g. It is this parameter that can be set accordingly to achieve bubbly flow.

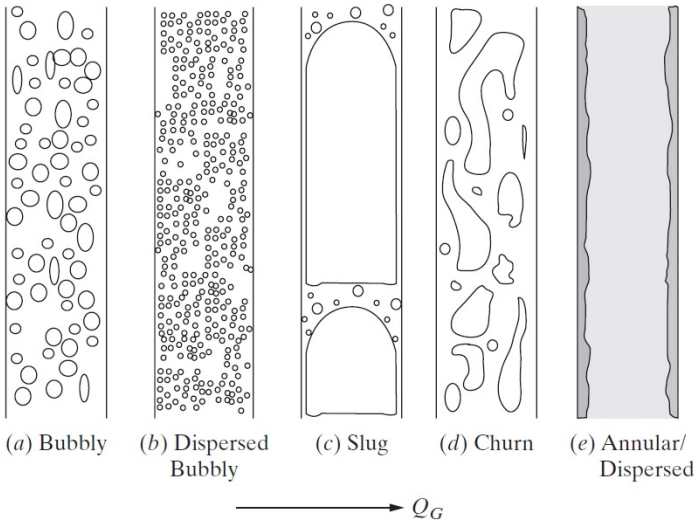

Figure 6: Visual representation of bubbles for the different flow patterns in vertical upward pipe flow [22].

2.1.2 Drift-flux model

In this subsection the behavior of rising bubbles in a liquid is described by investigating their size and velocity as a function of the column height. A useful tool for inspecting this relation is the drift-flux model. The drift-flux model treats the gas-liquid mixture as a pseudo single fluid, yet it allows a slip between the liquid and the gas [23]. Before we get into this model, let's first look at how a rising bubble changes in size. A schematic drawing of the problem at hand is depicted in Figure 7, indicating the chosen coordinate system y as the vertical position from the surface, H corresponding to the column height of the experimental bubbling facility and g to the gravitational constant. To simplify the bubbles are assumed to move in the direction of the flow only so that a one dimensional coordinate system suffices.

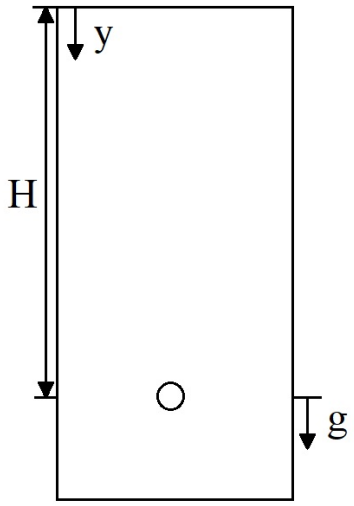

Figure 7: Schematic drawing of a rising bubble in a column.

To clarify, the position of the bubble in Figure 7 is $y = H$ and corresponds to the bottom of the column where the gas flow is injected. When the bubble reaches the surface its position equals $y = 0$. Now consider the bubble to obey the ideal gas law given in equation (6):

$$pV = nRT \tag{6}$$

where p is the pressure of the gas, V is the volume of the gas, n is the amount of gas, R is the gas constant and T is the temperature. The ideal gas law fails at low temperature and high pressure because the volume occupied by the gas is quite small, so the inter-molecular distance between the molecules decreases. Hence, an attractive force can be observed between them [24]. Since the pressure differences of a rising bubble operated at room temperature are extremely low, it is expected that the ideal gas law is a valid approximation. The pressure of the bubble as a function of the position in the column $p(y)$ is determined from equation (7):

$$p(y) = p_0 + \rho_l g y \tag{7}$$

where p_0 is the atmospheric pressure at $y \leq 0$. In the above equation there is also a contribution of the surface tension on the pressure difference: for a bubble this equals $4\sigma/R_b$, where σ is the surface tension between the inside and the outside of the bubble and R_b is the bubble radius. For small bubbles of $R_b = 1$ mm in water with $\sigma = 72.15 \cdot 10^{-3}$ N/m [15], this contribution is 289 Pa, three order of magnitudes lower than atmospheric pressure. Therefore, even for tiny bubbles, the pressure difference due to surface tension is negligible and is not included in equation (7). From this expression it becomes clear that the pressure on the bubble decreases as it is rising. Therefore, when the pressure drops the volume will increase so that the product PV still equals the constant nRT and equation (6) is satisfied. Substituting the bubble radius R_b for the volume of the bubble $V = \frac{4}{3}\pi R_b^3$ and the pressure relation

from equation (7) for the pressure in equation (6) and solving for R_b, equation (8) results:

$$R_b(y) = \left(\frac{3nRT}{4\pi(p_0 + \rho_l g y)} \right)^{1/3} \tag{8}$$

Since nRT is equal to a constant (pV), which can be determined if the initial volume of a bubble at $y = H$ is known, the increase of R_b at $y = 0$ can be calculated. For a column of height $H = 50$ cm and a bubble diameter of $2R_b = 1$ mm at the bottom of the column the bubble is expected to increase only 8.2 µm in size when it reaches the top of the column. Because this increase is so small it is assumed the bubbles rise with a constant size. Whether or not 1 mm is a reasonable estimate for the bubble diameter will be studied in Chapter 4.1.1, where the bubbles used in the experiments are analyzed.

To predict the bubble velocity, a simple drift-flux model is used. The model does not take into account surface tension because, as shown above, its contribution is expected to be some order of magnitudes smaller than the other terms, in this case the drag force F_D acting on the bubble and its driving force due to buoyancy, F_B. Considering the low density and small volume of the air bubbles, gravitational forces due to the mass of the bubbles are irrelevant. A force balance is constructed and given in equation (9):

$$m\frac{v_{bs}}{dt} = F_B - F_D = 0 \tag{9}$$

where m is the bubble mass, v_{bs} is the bubble slip velocity and steady state is assumed. Filling in expressions for the buoyancy force $F_b = \frac{4}{3}\pi R_b^3 \rho_l g$ and the drag force $F_D = \frac{1}{2} C_D \pi R_b^2 \rho_l v_{bs}^2$ a relation between the bubble radius R_b and velocity v_{bs} is found in equation (10):

$$v_{bs} = \sqrt{\frac{8g}{3C_D} R_b} \tag{10}$$

where R_b is given in equation (8), assumed to be constant over the height of the column, and C_D is the drag coefficient. Depending on the model, C_D changes for different bubble Reynolds numbers Re_b as becomes apparent from equation (11):

$$C_D = \begin{cases} \frac{24}{\mathrm{Re}_b} & 0 < \mathrm{Re}_b < 1 \\ \frac{24}{\mathrm{Re}_b^{0.646}} & 1 < \mathrm{Re}_b < 400 \\ 0.45 & \mathrm{Re}_b > 1000 \end{cases} \tag{11}$$

The model chosen for C_D is illustrated in [20]. By trial and error, different bubble Reynolds numbers can be inserted into equation (11), calculating C_D and then v_{bs} using equation (10). Filling v_{bs} back into equation (4) for the bubble Reynolds number with $d_b = 2R_b$, after a few iterations we should get our Reynolds number back. For the situation calculated before where $d_b = 1$ mm, Re_b is determined to be 109, corresponding to bubble slip velocity $v_{bs} = 107$ cm/s. Of course the calculated values are merely theoretical and depend on the size of the bubbles. Whether or not this is a reasonable estimate for the bubbles encountered during the experiments, is discussed in Chapter 4.

Now that a simple description for the behavior of a rising bubble has been established, it is important to make a distinction between the bubble slip velocity v_{bs} and the bubble rising velocity v_b since they can be so easily exchanged. For example, in the above calculation v_{bs} is assumed to be equal to v_b so that Re_b can be determined from equation (4). Since v_{bs} is defined as the difference between the velocity of the bubble v_b and the liquid v_l given in equation (12):

$$v_{bs} = v_b - v_l \tag{12}$$

the above calculation corresponds to the situation where the liquid is completely inert, i.e. $v_l = 0$. The slip velocity can be seen as more of a relative velocity with respect to the liquid also taking into account that the movement of a rising bubble alters the flow of the fluid around it. It is important to make a clear distinction between the two to not get confused later on. Now that the slip velocity is calculated,

let's relate the bubble velocity to the volumetric gas flow rate Q_g introduced in Figure 6, the quantity that describes the total volume of gas passing through a point in a particular period of time. The non-SI unit of Q_g that will be used throughout this report is sccm (standard cubic centimetre per minute) or $\mathrm{cm}^3/\mathrm{min}$. The definition of Q_g is given in equation (13):

$$Q_g = v_{sg} A_t \tag{13}$$

where A_t is the total area of the column and v_{sg} is the superficial gas velocity mentioned in Figure 5, defined as an artificial flow velocity calculated as if the given phase were the only one present. v_{sg} is given by equation (14):

$$v_{sg} = v_b \phi_g \tag{14}$$

where the gas holdup $\phi_g = A_g/A_t$ is the fraction of the area occupied by the gas bubbles and will have to be determined experimentally. Here A_g is the area occupied by the gas bubbles. Equation (15) then relates the true bubble rising velocity v_b to the gas flow rate Q_g as follows:

$$v_b = \frac{Q_g}{\phi_g A_t} = \frac{Q_g}{A_g} \tag{15}$$

This expression will prove useful to determine the bubble velocity v_b once the gas holdup ϕ_g or gas area A_g is known. To summarize, a simple model is established to formulate an estimate of the bubble size and velocity so as to get a feeling for typical values expected to be encountered during the measurements. Furthermore, it is stated that when velocities in multiphase flows are involved, quite some confusion arises between the definition of the slip velocity v_{bs} and the bubble rising velocity v_b.

2.1.3 Particle concentration

A big part of the project is determining the particle concentration, because mapping the distribution essentially describes the particle behavior. Therefore, this subsection is devoted to some simple expressions that calculate the (relative) concentration beforehand, as well as some other parameters like the surface area, number and volume [25].

Since the particles that are investigated have diameters ranging from some micrometers and smaller, they are mixed in a fluid with a certain weight per volume of solution ratio. The denotation is given in equation (16):

$$\mathrm{n}\,\%\ \mathrm{w/v} = \frac{m_p}{V_s} \tag{16}$$

where n is the value determining the percentage of particles present in the solution, w/v indicates that the ratio is calculated as weight per volume, m_p is the mass of the particles in g and V_s is the sample volume of the solution in mL. For example, for a 1 % w/v particle solution with a sample volume of 10 µL, the accumulated mass of the particles in the sample is 0.1 mg. In order to find the total volume occupied by the particles V_p, we make use of equation (17):

$$V_p = \frac{m_p}{\rho_p} \tag{17}$$

where ρ_p is the particle density in $\mathrm{g/cm}^3$. So only making use of given material properties, as depicted in the left hand side of equation (16), and a predetermined sample volume of the solution V_s the total mass and volume of the particles present in the solution can be determined. The relative particle concentration is then the ratio of V_p divided by the volume of the solution. Furthermore, the volume of a single particle V is given in equation (18):

$$V = \frac{\pi}{6} d_p^3 \cdot 10^{-12}\ \mathrm{cm}^3/\mathrm{particle} \tag{18}$$

where d_p is the diameter of the particles in μm. Additionally the number of particles can be calculated from equation (19):

$$N = \frac{6m_p}{\pi \rho_p d_p^3} \cdot 10^{12} \text{ particles} \tag{19}$$

The product NV should equal V_p in equation (17). Finally, the total surface area of the particles can be determined and is given in equation (20):

$$A = \frac{6m_p}{\rho_l d_p} \cdot 10^4 \text{ cm}^2 \tag{20}$$

Since the surface area A is inversely proportional to the particle diameter d_p, A will increase for smaller particles. Here the same reasoning applies as mentioned earlier for bubbles, where the probability of particle-bubble interaction becomes more likely when the surface area is large.

2.2 Bubble-particle interaction model

The collection of particles by rising bubbles is the central process in froth flotation [26]. To study this process, the collection efficiency E of a bubble and a particle is defined in equation (21):

$$E = E_c E_a E_s \tag{21}$$

where E_c is the collision efficiency, E_a is the attachment efficiency and E_s is the stability efficiency of the bubble-particle aggregate. The dissection of the collection efficiency into three process efficiencies was used by Derjaguin and Dukhin [27] and focuses attention on the three zones of bubble–particle collection where, in order, hydrodynamic interactions, interceptional forces and surface forces are dominant, as illustrated in Figure 8. We should note that these zones are not completely discrete, rather they grade into one another. Since surface forces are relatively short range, they do not have any significant influence on the collision step. This is why collision and attachment may be treated as essentially independent processes [28].

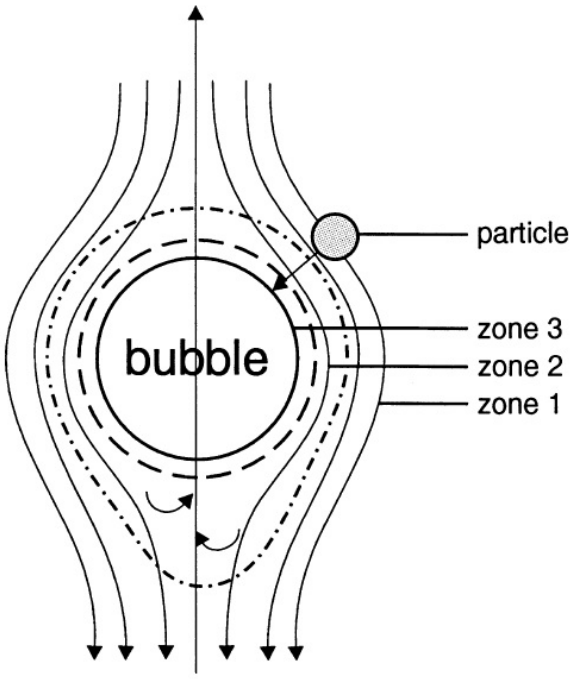

Figure 8: Hydrodynamic force (1), interceptional force (2) and surface force (3) zones of interaction between a rising bubble and a particle. The first two zones roughly correspond to the collision process, whereas the third zone can be regarded as an attachment process [26].

Zone 1 is a region far away from the bubble surface. In this zone, hydrodynamic forces are dominant. The hydrodynamic drag forces act to sweep the particle around the bubble, viscous forces tend to slow down this relative motion between the particle and bubble, while particle inertial and gravitational forces drive the particle towards the bubble surface. The interaction between the particle and the bubble in this zone is a collision process. In Zone 2, the liquid flow around the rising bubble surface creates a tangential stream which sweeps adsorbed ions or surfactants from the upper hemi-surface of the bubble toward the rear of the bubble. Due to their different mobilities, ions are non-uniformly concentrated near the rear of the bubble, which results in a strong electrical field between the upper surface and colliding particles. Therefore, the motion of the particles in Zone 2 is controlled by, in addition to the forces existing in Zone 1, diffusional and electrophoretic forces. These forces are called interceptional and the particle-bubble interaction in this zone also corresponds to the collision process. For sub-micron particles the diffusional and electrophoretic forces are more important than the gravitational and inertial forces and cannot be neglected. In Zone 3, surface forces become important. Depending on the sign of the total force, the rate of thinning of the liquid film between the particle and the bubble may be accelerated or retarded and, therefore, the attachment of particles to the bubble surface may be promoted or prohibited. As a result, particle-bubble interaction in Zone 3 can be regarded as an attachment process [19].

Now that the main forces that play a role in the bubble-particle interaction have been introduced, let's look at how this all contributes to the quantity that describes the overall efficiency of particle impairment. This quantity describes the transport of particles as non-dimensional, meaning the bubble flotation column is considered as a point particle. For a flotation process, the flotation recovery R is given by equation (22) [26]:

$$R = R^* \left(1 - e^{-kt_b}\right) \tag{22}$$

where R^* is the maximum particle flotation recovery, t_b is the bubbling time and k is the flotation rate constant given by equation (23):

$$k = \frac{3Q_g E_c E_a E_s}{2d_b A_c} \tag{23}$$

where the volumetric gas flow rate Q_g was introduced in equation (13) and is a predefined value depending

on the desired flow, and A_c is the cross-sectional area of the column depending on the geometry of the experimental facility. The particle diameter d_b is a property that can be determined experimentally, which leaves us with the product $E_c E_a E_s$, known as the collection efficiency E as stated in equation (21). For the small particles considered in the present work, detachment need not be considered [21], i.e. $E_s = 1$, simplifying the problem a little. Chapters 2.2.1 and 2.2.2 deal with the analytical expressions for the attachment efficiency E_a, where the modified Dobby-Finch model approach is used, and the collision efficiency E_c calculated from the generalised Sutherland equation, respectively.

2.2.1 Modified Dobby-Finch model

The Dobby–Finch attachment efficiency model [29] is based on the relative magnitude of the induction time and the sliding time. The induction time t_i is the time required for bubble-particle attachment to occur and the sliding time t_s is the time that the bubble and the particle are in contact, generally of the order of 10^{-2} s or less. This means that attachment is only possible when $t_i \leq t_s$. The adhesion angle θ_a is defined as the angle at which attachment occurs and the critical angle θ_c is the maximum possible angle at which bubble-particle collision takes place. The attachment efficiency E_a is then the ratio of the area corresponding to θ_a to the area corresponding to θ_c and the resulting expression is given in equation (24):

$$E_a = \frac{\sin^2(\theta_a)}{\sin^2(\theta_c)} = \frac{\sin^2\left\{2\arctan\left(\exp\left[-Ad_p^B \frac{2(v_p+v_b)+(v_p+v_b)\left(\frac{d_b}{d_p+d_b}\right)^3}{d_p+d_b}\right]\right)\right\}}{2\beta\left[\sqrt{1+\beta^2}-\beta\right]} \tag{24}$$

where the induction time $t_i = Ad_p^B$, v_p and v_b are the particle and bubble velocity and d_p and d_b are the particle and bubble diameter. A and B are parameters for the induction time adjusted independently so as to obtain best agreement between calculated and experimental E_a values for each experimental condition. As illustrated in the denominator, an expression for the maximum collision angle θ_c, also known as the angle of tangency, has been obtained [19] and is shown in equation (25):

$$\theta_c = \arcsin\left\{\sqrt{2\beta\left(\sqrt{1+\beta^2}-\beta\right)}\right\} \tag{25}$$

where β is a dimensionless number characterizing particle collision and is determined from equation (26):

$$\beta = \frac{4d_p\rho_p}{3\mathrm{K}d_b(\rho_p-\rho_l)} \tag{26}$$

where ρ_p and ρ_l are the particle and liquid density and K is the particle Stokes number given in equation (3).

2.2.2 Generalised Sutherland equation

Dukhin derived an analytical expression for the collision efficiency and is depicted in equation (27) [26]:

$$\frac{E_c}{E_0} = \sin^2(\theta_c)\exp\left\{3\mathrm{K}_3\left(\cos(\theta_c)\left[\ln\left(\frac{3}{E_0}\right)-1.8\right]-\frac{2+\cos^3(\theta_c)-3\cos(\theta_c)}{2E_0\sin^2(\theta_c)}\right)\right\} \tag{27}$$

and has been termed the generalised Sutherland equation (GSE). It can be seen that the collision efficiencies calculated with the GSE model (E_c) are different than those calculated by the Sutherland model (E_0) by a factor which is the product of $\sin^2(\theta_c)$ and an exponential term. This factor is not simply a correction coefficient. Instead, it characterizes a new collision mechanism, i.e. the coupling of the interception mechanism with the effect of inertial forces. The first term in the exponent represents the inertial positive effect due to the hydrodynamic pressing force while the second term is the negative

inertial effect due to the centrifugal force [19]. The collision efficiency E_0 as proposed by Sutherland is given by equation (28):

$$E_0 = \frac{3d_p}{d_b} \tag{28}$$

According to Sutherland, all particles lying within a collision radius R_c will collide with the bubble and therefore the collision efficiency is determined by the ratio of the cross-sectional area of the stream tube ($\pi R_c^2 = 3\pi d_p d_b/4$) to the projected area of the bubble ($\pi d_b^2/4$), resulting in equation (28). This model laid the basis for the development of later E_c models and is a sufficiently close approximation to the interceptional effect in the case of high flow velocity around the bubble [30]. However, the neglect of particle inertia might not be entirely valid. It has been shown that, below a critical Stokes number, particle inertia has a strong negative effect on particle-bubble collision and that this effect becomes more and more pronounced as the Stokes number approaches this critical Stokes number [31] Therefore, a normalized version of the Stokes number (K_3) appears in equation (27) defined as:

$$\mathrm{K}_3 = \mathrm{K}\left(\frac{\rho_p - \rho_l}{\rho_p}\right) \tag{29}$$

and depends on the Stokes number K, the particle density ρ_p and the liquid density ρ_l.

This chapter started with the behaviour of different flows in bubble columns. It was concluded that the preferred flow pattern is bubbly flow to avoid bubble coalescence and maximize total bubble surface area for the efficient entrainment of particles. Next, an estimate was given of the bubble rising velocity utilizing the drift-flux model. Along with the bubble-particle interaction model introduced above, this theory will serve as a helpful way to compare the experimental results and is applied in Chapter 4.2. Before this is discussed however, first the experimental setup is explained in Chapter 3.

3 Methodology

So far the research topic has been introduced and an analytical analysis of the theory is presented. In this chapter the preparations are explained that will lead to the experimental results. Chapter 3.1 provides information regarding the different phase materials in the MSFR, where the key variables per phase are emphasized. In Chapter 3.2 the various components of the bubble facility are discussed, followed by explaining the necessary steps performed to process grabbed images in Chapter 3.3. Finally, Chapter 3.4 deals with additional experimental requirements and to clarify what parameters need to be determined in order to compare the model to the experimental results. The experimental requirements section is concluded with a measurement schedule.

3.1 Selection of simulant materials

The flotation process is very weakly influenced by the gas used. The equations governing the fluidodynamics of gas bubbles show a dependence on the difference of the density between the liquid and the gas phases. However, the density of the gas is much lower compared to the density of the liquid and it is usually neglected for this reason. Air is typically used for standard processes and also in the experimental setup in this work. An additional consideration for the selection of the gas is the reactivity with the fluid and particles. For molten salt systems, which are very sensitive to water and oxygen levels, an inert gas like helium must be used to avoid reactions such as oxidation [32].

The most important parameters to take into account for the particle selection are the density, particle size and hydrophobicity. As there are a variety of particles in the MSFR and their size (ranging from a few ångströms to a few microns) is still a matter of discussion [33], particles with different size and density have been considered in order to establish the influence of these parameters on the flotation efficiency. The influence of hydrophobicity is difficult to estimate as single factor as this would require a coating of the particles to make them equally hydrophobic (same contact angle) [15]. Nevertheless, some guidelines to predict the behaviour of noble metals can be inferred from the following considerations. The necessary condition for flotation is given by equation (30):

$$\sigma_{lg}\cos(\theta) + \sigma_{ls} = \sigma_{sg} \tag{30}$$

where σ_{lg} is the liquid-gas surface tension, σ_{ls} is the liquid-solid surface tension, σ_{sg} is the solid-gas surface tension and θ is the contact angle defined as follows: under equilibrium, on a plane that is perpendicular to the three-phase contact line, a line tangent to the gas–liquid interphase and passing through the point where all three phases meet forms an angle θ, called the contact angle with the solid surface [22]. Equation (30) determined from the different surface tensions and the contact angle becomes more clear by looking at the schematic representation depicted in Figure 9. It follows that the larger the contact angle the greater the tendency of bubbles to adhere with particles and the more efficient the flotation process. In particular, flotation is only possible when the contact angle θ is greater than zero. This condition is valid for all the metallic particles in molten salts which are hydrophobic if $\theta > 90°$ [34] and have contact angles that were reported to be in the range of 90°-105° [15].

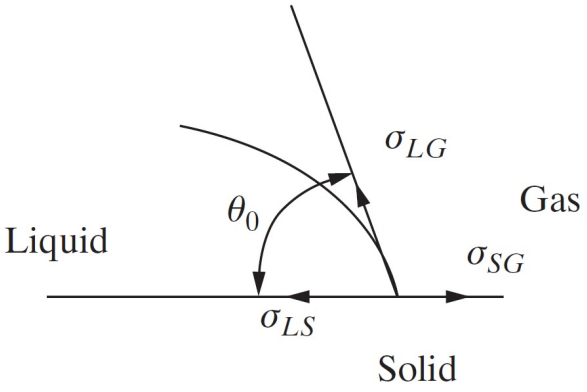

Figure 9: The liquid-gas-solid interface [22].

The particles used in this work to mimic the metallic particles are made of polystyrene because of their hydrophobic behaviour and fluorescent properties. Multiple size ranges are available with a density of 1.05 g/cm^3. The particle weight per volume of solution ratio is 1% w/v. When the initial sample volume of the solution V_s is known, the mass of the particles m_p can be determined according to equation (16). With the help of equations (17) and (19) the volume and number of particles can then be calculated.

The fluids considered as simulant for molten salts should provide similarities for what concerns the flotation mechanism and specifically the bubble-particle collection process. In addition to the properties of particles and bubbles (ρ_p, R_p, R_b), the particle collection efficiency depends on the fluid motion and the velocity fields around the bubbles. The latter parameters are governed by the dimensionless Reynolds number Re and thus strongly depend on the dynamic viscosity of the liquid μ_l. Table 1 shows a comparison of the most important physical properties for molten salt mixtures (FLiNaK, LiF-ThF_4, FLiBe) and for some simulant fluid candidates. Glycerol-water mixtures were selected [32] as they have a close dynamic viscosity to the fuel salt (FLiNaK) with the exact value that can be set by varying the composition. Bubble formation in this liquid can however be quite different as other properties, namely the liquid density ρ_l and the surface tension σ, play a role due to the temperature differences in the fuel salt [15].

Table 1: Physical properties of molten salt and simulant fluids at operational temperature T (K), density ρ (g/cm^3), dynamic viscosity μ (mPa·s), kinematic viscosity ν (mm^2/s) and surface tension (10^{-3} N/m) [15]. *MSBR fuel composition: LiF-BeF_2-ThF_4 (72-16-12 mol%)

Molten salt mixtures	T	ρ	μ	ν	σ
FLiNaK	900	2.018	3.594	1.781	
LiF-ThF_4 (78-22 mol%)	900	4.418	7.622	1.725	277
FLiBe (66-34 mol%)	900	1.707	7.524	4.408	
MSBR* fuel	900	3.342	10.703	3.203	185
Simulant fluids					
Acq. glycerol (41.6 wt%)	293	1.104	3.968	3.594	68
Acq. glycerol (34.2 wt%)	293	1.084	2.882	2.659	
Water	293	0.997	0.891	0.894	72.15

3.2 Experimental setup

In this section the experimental setup that is used for the measurements is explained. The setup consists of three parts, namely the bubble column, the laser and the detector. The method of detecting the fluorescent particles is described on the basis of the excitation and emission spectra.

3.2.1 Bubble column

The bubble column (diameter: 25 mm, height: 605 mm) allows the visual observation of the particle attachment processes as well as the determination of the bubble distribution as a function of the input parameters. The cylindrical column is made of polymethyl methacrylate (PMMA) or Perspex® and the gas required for the experiments is supplied from the compressed air line in the laboratory. A mass flow controller (Bronkhorst EL-Flow Select) is used to accurately control the gas flow during experiments and provides air flow up to 500 sccm, the non-SI unit of cm^3/min under standard operating gas temperature (0 °C) and pressure (1.013 bar) and commonly used for gas flow controllers [35]. The gas is injected into a pressure chamber at the bottom of the column and bubbles are formed through a bubble sparger (metal sintered filter, SIKA-R3 with 26 mm diameter, a thickness of 3 mm and a 3 µm average pore size [14]). At the top of the column, the particle-bubble separation is performed using a Hallimond tube. This device serves as a collector for the particles so that a decrease of particle concentration in the column during bubbling can be observed over time. In Figure 10 the bubble column and the Hallimond tube are presented. The blue cord is the gas flow inlet.

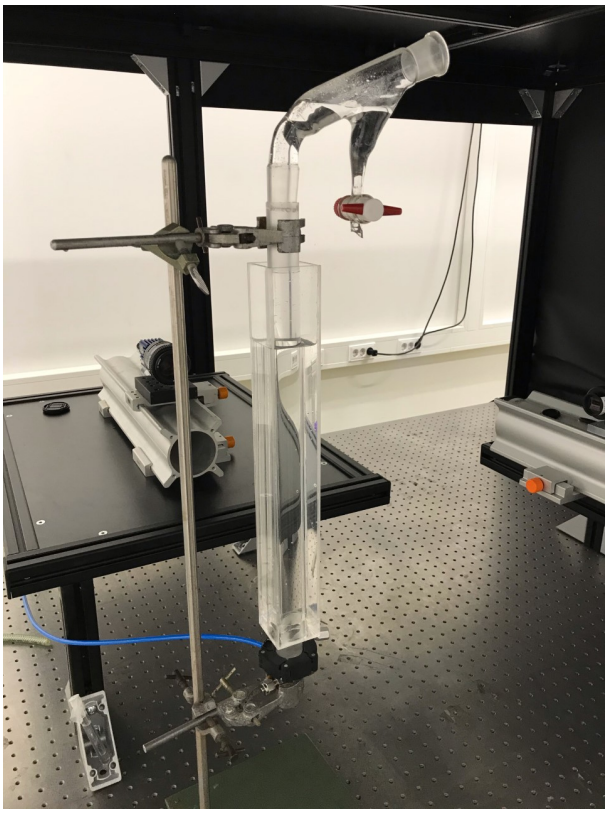

Figure 10: Picture of the bubble column.

Since the measurement detection relies primarily on optics, prior to the project the idea was presented to use a transparent (Perspex) column that is circular on the inside and square on the outside to minimise light signal distortion due to shape and differences in refractive indices. A water-Perspex interface will therefore cause less distortion compared to a Perspex-air interface. Building a transparent, squared container filled with water around a circular flotation column might reduce distortion and increase the accuracy of the measurements. This adjustment to the setup has been realised as displayed in Figure 10 and the absence of distortion was investigated by taping a piece of scaled graph paper on the column. It can be seen in Figure 11 that distortion is present, but only in the region between the cylindrical bubble column and the squared container surrounding it. Since no distortion is present inside the bubble column this is a huge improvement compared to the simple cylindrical glass column, where especially close to the edges distortion was a major issue. In Figure 11 scales of the inside diameter of the bubble column and the height the camera captures are included in mm.

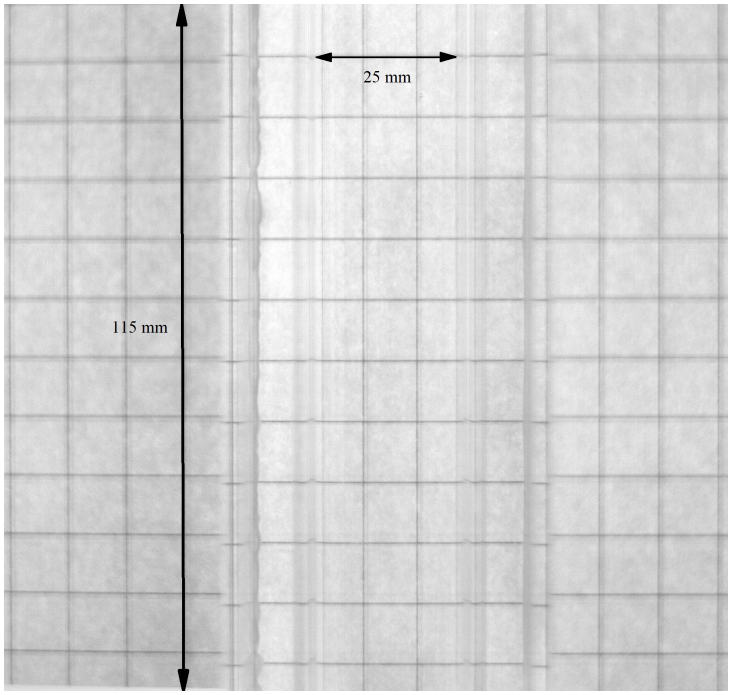

Figure 11: A picture of the column in front of a piece of scaled graph paper to locate possible occurrence of light distortion. No distortion is present in the measurement area.

3.2.2 Laser

The method to detect the position and size of the particles is LIF, or Laser Induced Fluorescence. This is a very sensitive laser imaging technique for species concentration, mixture fraction and temperature measurements in fluid mechanical processes, the former of which is of interest for this research. The principle is a two-step process: absorption of a laser photon followed by isotropic emission of a fluorescent photon from the excited state. In Figure 12 a schematic representation of the LIF principle can be found.

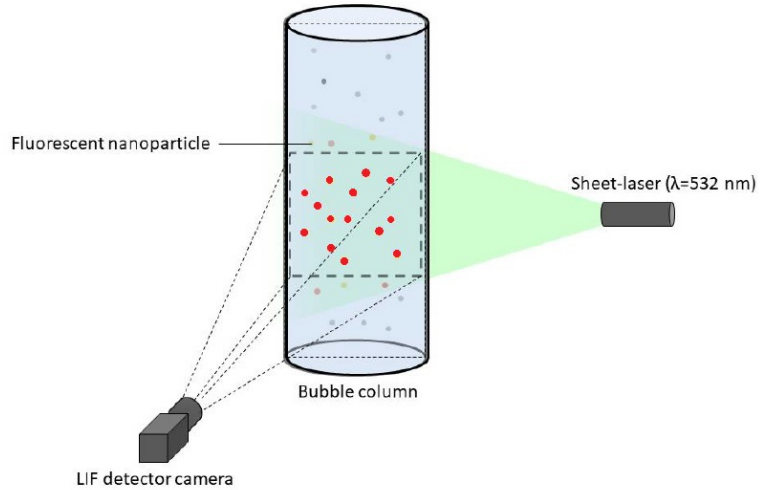

Figure 12: A schematic overview of the fluorescence measurements. The green area represents green light from the laser sheet incident on the fluorescent particles, that due to this emit red light in all directions so that a LIF detector camera is able to detect the particle distribution [14].

The laser model used during the experiments is PSU-H-FDA provided by LaVision (Figure 13). This is a Nd:YAG (neodymium-doped yttrium aluminum garnet; Nd:$Y_3Al_5O_{12}$) laser sending out 532 nm green light. For the different measurement tasks a wide range of output energies up to 400 mJ per pulse are available. Pulse rates of 10 Hz are used for gaseous and liquid fluid applications.

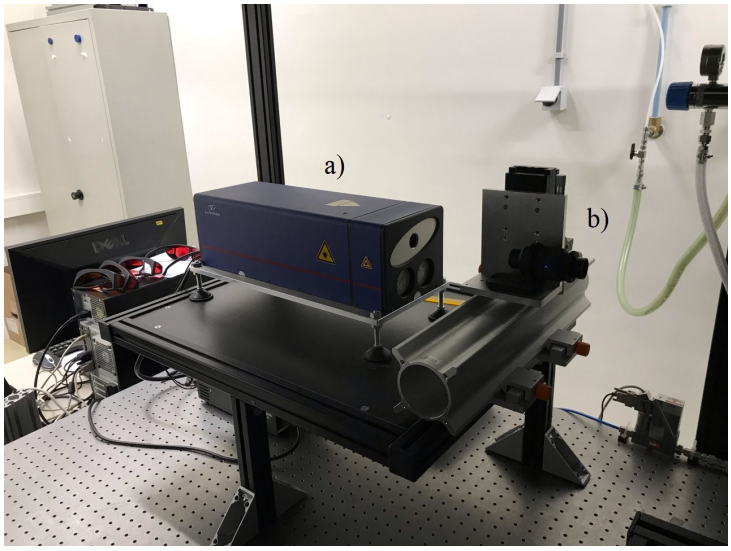

Figure 13: The laser system used to excite the fluorescent particles, consisting of the generation unit a) and the sheet optic b).

In most systems a light sheet is formed by expanding a laser beam in one direction by means of a short-focal-length cylindrical lens. The laser beam usually has a diameter that does not match the desired thickness of the light sheet. Therefore, a second lens, usually a spherical lens with a long focal length, is applied to obtain the desired thickness in the measurement domain [36]. A typical two-lens configuration, called the sheet optic, also used in this laser system given in Figure 13 b), is shown schematically in Figure 14. The laser beam is focused when its width (top view) is as small as possible and its height (front view) matches the field of view of the detector.

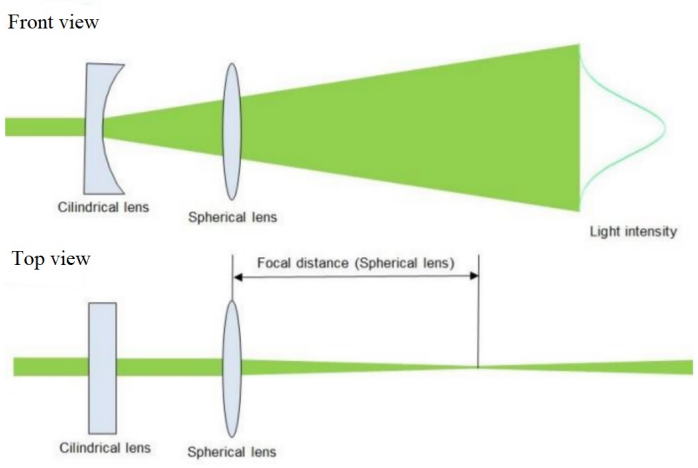

Figure 14: Light sheet formation using a cylindrical and a spherical lens [36].

The laser safety is Class 4, the highest and most dangerous class of laser light. By definition, it can burn the skin or cause devastating and permanent eye damage as a result of direct, diffuse or indirect beam viewing. Therefore, during operation it is necessary to wear laser protective goggles at all times so as to reduce hazardous laser eye exposure.

3.2.3 Detector

When the laser beam is formed to a light sheet it intersects the fluid area of interest. The resulting fluorescent light from excited particles in the light sheet is imaged through a selective filter onto a time-gated digital camera. The conversion of LIF images into meaningful concentration or temperature fields is based on calibration measurements, which will be discussed in the next subsection. The camera model is an Imager MX 4M (2048 x 2048 pixels) that combines high spatial resolution with a high framerate. In Figure 15 the lens of the Imager MX is shown. Here the values ranging from 1.4 to 16 indicate the f-number, defined as the ratio of the system's focal length to the aperture diameter. The smaller the f-number, the higher the aperture diameter and thus the light-gathering area. With the LIF-filter applied, the f-number is always set to its lowest value (1.4) meaning as much light as possible is detected by the CMOS sensor that conveys the information to make an image.

Figure 15: Detector used for grabbing high-speed images. On the camera (right-hand side) a filter can be mounted that detects LIF-active particles.

3.2.4 Excitation and emission spectra

In order to check whether the emitted wavelength of the LIF-active particles due to their excitement by the incident laser beam light corresponds to the transmission of the filter, Spherotech, the company that provides the nanoparticles used for the experiments, provided excitation and emission curves for the particles they manufacture. The curves are depicted in Figure 16, where the particles under investigation in this research are Nile Red.

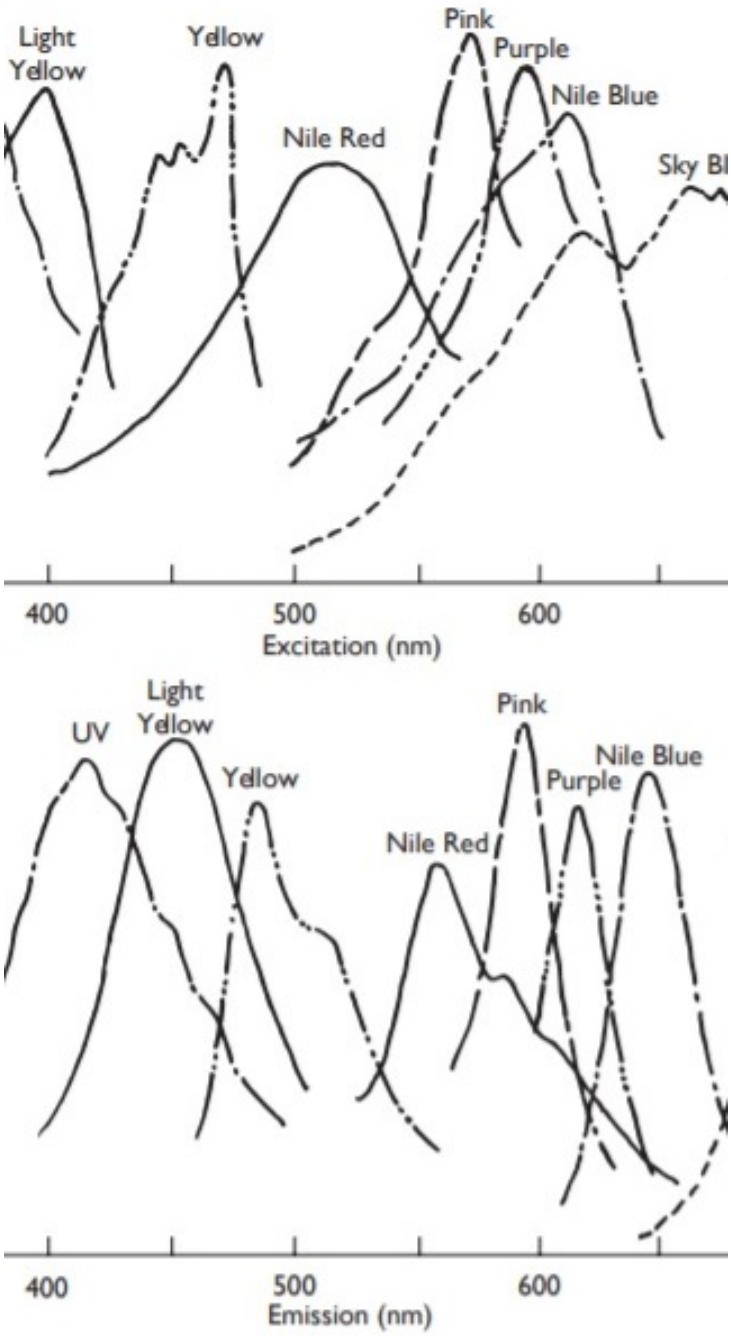

Figure 16: Excitation and emission curves for different fluorescent particles. The excitation peak of Nile Red particles lies at about 530 nm (incident laser light) and the emitted light can be detected by a 600 nm LIF filter [37].

Furthermore, the excitation spectrum of the particles is determined after the laser light is absorbed by the particles. The resulting emission that occurs at a slightly higher wavelength must then correspond to the bandwidth of the filter transmission. This is depicted schematically in Figure 17.

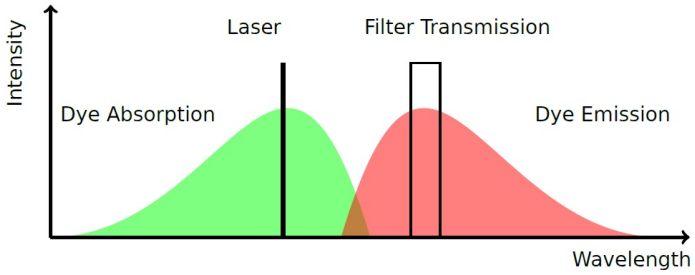

Figure 17: Absorption and emission diagram for the tracers and filters [38].

3.3 Image processing

The processing of the images is divided into two parts. The first part focuses on the bubble characteristics in the column by looking at how the bubble diameter and gas holdup change for different gas flow rates. For this a MATLAB script is compiled that handles the image processing of a large amount of images provided in Appendix A.1. The second part is concerned with quantifying the removal of particles during bubbling. The software that is used for measuring particle concentration is called DaVis and is provided by LaVision. Chapters 3.3.1 and 3.3.2 explain in more detail the image processing steps required for bubble and particle detection.

3.3.1 Bubble detection

As mentioned before, the bubbles facilitate the transport of particles. Therefore it is interesting to investigate the bubble behaviour in the experimental facility. The parameters that have been chosen to display this behaviour are the gas holdup and the bubble diameter. For low gas flow rates applied the regime is bubbly flow. This is the desired flow since small bubbles are formed that are not expected to coalesce to maximize total bubble surface area and as a result maximize particle-bubble interaction. Because for bubbly flow coalescence does not take place and the bubbles are sufficiently small, the surface tension of the surrounding liquid is high enough so that the bubbles can be approximated as spheres [23]. This is the main assumption of the algorithm used for detection of bubbles from grabbed images.

First, the images are loaded so MATLAB recognizes them and are made available for processing. A crop region, or mask, is then specified so that only the area in the column where the bubbles are present can be visualized. Next, the images are converted to grey scale so that a set of morphological operations can be applied to the images that assist in removing small blemishes without affecting the overall shapes of the objects, such as reconstruction-based opening and closing. After these operations the imfindcircles command is called to detect the bubbles that can be clearly distinguished from the surrounding liquid. This command stores the position and size of all the located circles. More specifically, from the two dimensional cross-sectional images of the column the total area occupied by the bubbles will then result in the gas holdup. From the scaling an average bubble diameter can be calculated. The results of the analysis are discussed in Chapter 4.1.1.

3.3.2 Particle detection

Determining bubble properties is only half of the story. Because of their significantly smaller diameter, investigating sub-micron particles is a much more challenging task. In fact, they are so small that a single particle can not be detected by present measurement equipment. However, utilizing the fluorescence technique described above, an agglomeration of particles can be visualized with a certain intensity. Preparing different samples (one sample per experiment) with a pre-determined particle concentration, the amount of detected light, or measured intensity, can be related to the actual concentration. A graph that displays the linear dependence of the form $I = A \cdot C$, where I is the measured intensity, A is a constant characterizing the slope and C is the sample concentration, this first-order approximation between measured intensity and actual concentration is called a calibration curve. The sample concentration is nothing more than the amount of particle solution added to the setup prior to an experiment. The

intensity at various sample concentration values C, say 20, 40, 60, 80 and 100%, provide the data points through which the constant A is calculated to best fit the calibration curve. The curve can then be used to calculate the relative particle concentration during a bubbling experiment by interpolation of the corresponding measured intensity. An example of such a curve is depicted in Figure 18. On the y-axis the measured fluorescent intensity is in units of counts. This is a measure of the average grey level of the pixels.

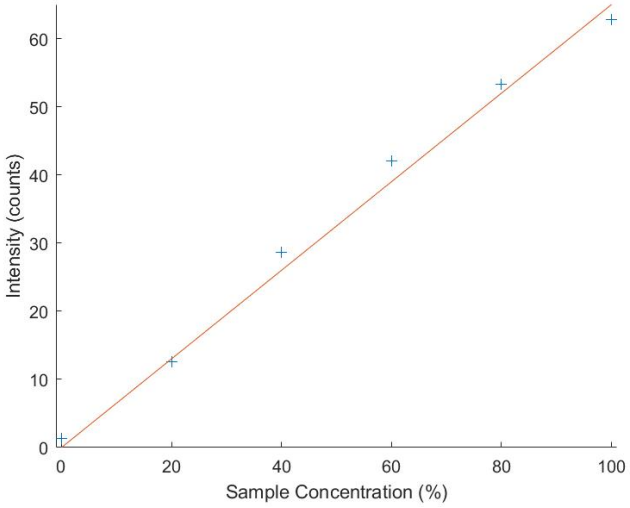

Figure 18: Calibration curve determined prior to an experiment. During a measurement interpolation is performed to calculate the relative particle (sample) concentration.

Once a calibration curve is established, the particle evolution over time during the bubbling process can be quantified in terms of relative sample concentration. Additionally, when the number of particles per volume is known for a given sample concentration, the decrease of the amount of particles can be determined.

During the experiments, images are grabbed in certain time intervals. However, a number of operations need to be performed on the images before appropriate interpretation of the acquired data is possible. The various image processing steps that are taken care of are listed below.

- Background subtraction: the camera's dark current (dark image) and surrounding light (background image) add an offset to the signal from the actual experiment. In order to extract the pure LIF signal these offsets are subtracted in this step.
- Sheet processing: the laser beam exhibits a cross-sectional intensity distribution, which is compressed to a profile perpendicular to the beam axis when being formed to a sheet. These inhomogeneities will decrease the accuracy of the results. Furthermore, the optical components of the detection system will influence the detected signal. These effects will be corrected for in this step.
- Image correction: corrects the image distortion.
- Concentration calculation: calculates the relative particle concentration from the calibration curve.
- Data transfer: the data is stored in a text file, completing the image processing.

Above the different procedures for both enhancement and processing of images grabbed during the experiments are summed up. For more information regarding the image processing steps and appropriate settings the reader is referred to Appendix A.2.

3.4 Experimental requirements

The main focus of the experiments is the behaviour of sub-micron particles of different sizes on the gas flow rate and bubbling time. In order to investigate this process to full extent, an assumption is made

to only measure on one part of the 605 mm long bubble column, specifically the middle. It is expected that the middle part of the bubble column is representative for the whole column. In Chapter 4.1.2 this assumption is researched by inspecting different parts of the column. With an interrogation window size of 40 to 50 mm in height a single window has been chosen to focus on the change of particle concentration for various particle sizes and gas flow rates.

A Hallimond tube is the most common option to extract particles in bubbling systems. An alternative would be to position a metal foam in or above the liquid to collect the particles since they stick to the foam. This has been considered, however some other complications arise when applying this method, the most concerning being the pressure buildup. Besides the pressure, also the accumulation of gas under the filter cause problems. Even though the Hallimond tube can not be added in the reactor to filter out particles, for the experiments it is the preferred method since it allows to apply a boundary condition at the top of the column, where particles are removed at a certain rate. Its efficiency is discussed in Chapter 4.1.3.

From equation (22) it becomes clear that the maximum recovery of particles is achieved at $t = \infty$, meaning that a longer measurement time results in a higher reduction in the measured particle concentration. However, since we expect the recovery to increase the most in the first 20 minutes of the experiment due to the exponential behaviour in equation (22), the bubbling time during a measurement is set to a maximum of one hour.

3.4.1 Validation of the model

Throughout Chapter 2 an overview is given of all the parameters that need to be determined in order to compare the experimental results to the bubble-particle interaction model. They are compared by investigating the particle recovery rate R, governed by equation 22. The various parameters of interest calculated are showcased in Table 2 below. The exact chosen parameter values to predict the recovery of particles observed in the experiments are given in Chapter 4.2.

Table 2: Parameters required to calculate particle flotation recovery R in equation (22).

Parameter	Description
v_p	Particle settling velocity
v_b	Bubble rising velocity in equation (15)
$R_p = d_p/2$	Particle radius
$R_b = d_b/2$	Bubble radius
A	Parameter for the induction time t_i in equation (24)
B	Parameter for the induction time t_i in equation (24)
ρ_p	Density of the particle
ρ_l	Density of the liquid
μ_l	Dynamic viscosity of the liquid
Q_g	Gas flow rate
A_c	Cross-sectional area of the column
R^*	Maximum particle flotation recovery
t_b	Bubbling time

3.4.2 Measurement schedule

After careful consideration of all preliminary requirements, a measurement schedule is constructed, depicted in Table 3 below. The measurements are varied by two parameters, namely the polystyrene particle diameter and the gas flow rate. Firstly, the availability of the particle sizes offer extensive investigation of the effect of particle inertia on the collection efficiency of the bubbling process, with average sizes of $\overline{d_p} = 0.25$ µm (0.1–0.3 µm), $\overline{d_p} = 0.53$ µm (0.4–0.6 µm) and $\overline{d_p} = 0.87$ µm (0.7–0.9 µm) [37]. Secondly, the values of the chosen gas flow rates are the same as those inspected by E. Capelli for comparison with micro-sized particle recovery rates. She conducted similar work on this topic, looking at the extraction efficiency of molybdenum and iron particles with sizes ranging from 3 to 149 µm [15]. In addition to the the measurements indicated in Table 3 that study particle extraction in an aqueous glycerol (34.2 wt%)

solution, this process is also investigated in a less viscous fluid like water to compare to the model.

Table 3: Number of measurements that will be performed for different particle diameters d_p (µm) and gas flow rates Q_g (sccm). $\overline{d_p}$ (µm) is the average particle diameter.

d_p	$\overline{d_p}$	$Q_g = 5$	$Q_g = 10$	$Q_g = 25$	$Q_g = 50$
0.1–0.3	0.25	#1	#2	#3	#4
0.4–0.6	0.53	#5	#6	#7	#8
0.7–0.9	0.87	#9	#10	#11	#12

4 Results

The purpose of this chapter is to show the experimental findings and their comparison to the probabilistic flow model that places emphasis on bubble-particle interaction discussed in Chapter 2.2. The experimental results are presented first in Chapter 4.1, followed by the model results in Chapter 4.2.

4.1 Results of the experiments

A great deal of research has been conducted on particle extraction and bubble evolution in the column. The primary focus lies on the particle distribution over time, however the behaviour of the bubbles is of equal importance, since their presence might to some extent influence particle detection. Therefore, both bubble and particle characteristics are topics of discussion.

4.1.1 Bubble characteristics

Primarily focusing on the bubbles, the gas holdup and the bubble diameter are investigated and how they change for different gas flow rates. To visualize the bubbles, not LIF but the standard imaging mode of the camera is operated. The gas flow rates that have been selected range from 5 to 40 sccm in steps of 5 sccm. For each selected gas flow rate, 60 images are grabbed and the average gas holdup and bubble diameter are calculated with the help of the bubble detection algorithm introduced in Chapter 3.3.1, as well as the standard error of the mean (SEM). The algorithm first loads in the image files and then searches for the bubbles as circles. The detected circles with certain diameter and area can be used to calculate an average diameter and gas holdup. The simulant fluids under consideration are an aqueous glycerol solution (41.6 wt%) and water. More information regarding the exact calculation can be found in Appendix A.1. In Figures 19 and 20, as a function of the gas flow rate, the average bubble size and gas holdup are depicted, respectively.

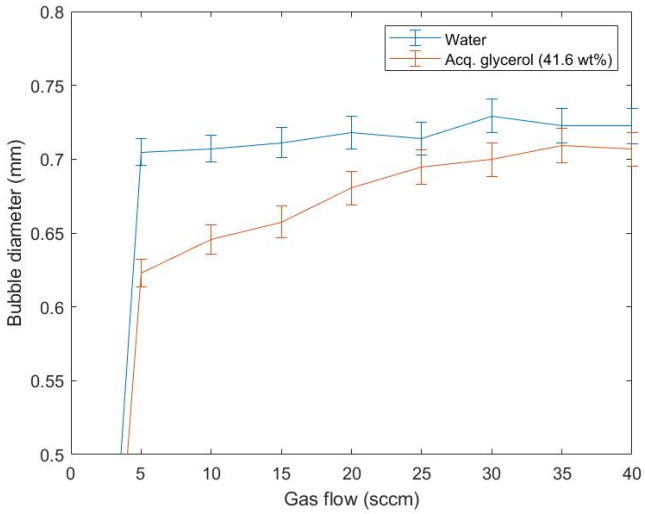

Figure 19: Plot of the bubble diameter as function of gas flow rate for two simulant fluids.

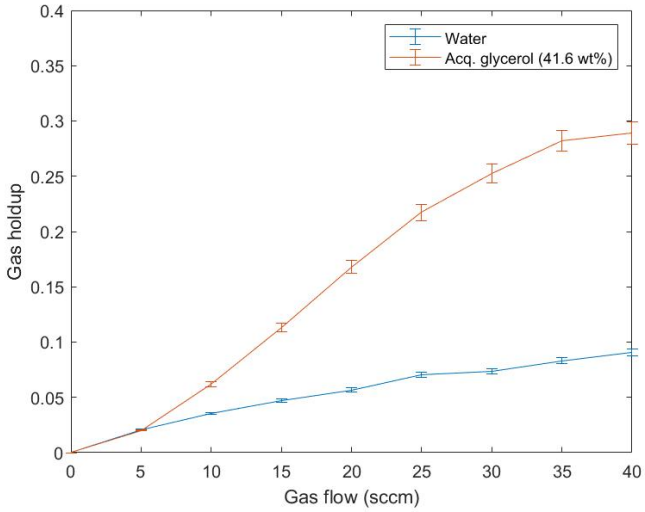

Figure 20: Plot of the gas holdup as function of gas flow rate for two simulant fluids.

Looking at Figure 19, when comparing the aqueous glycerol (41.6 wt%) solution with water, in both cases a small increment is observed when the rate of gas flow increases. In order to understand the change of gas holdup, or volume fraction occupied by the bubbles, the gathered results depicted in Figure 20 are compared to literature [32], shown in Figure 21. Here the superficial gas velocity is proportional to gas flow rate, see equation (13). Both simulant fluids show reasonable agreement with the relationship in literature according to the bubbly flow regime. From Figure 20, at 40 sccm a maximum gas holdup results, indicating the transition from bubbly flow to potential (churn-turbulent) flow. Moreover, it is observed that the aqueous glycerol solution reaches a gas holdup of 30% and water a little less than 10% at a gas flow rate of 40 sccm. A possible reason for this difference could be that the higher viscosity of the glycerol solution increases the bubble residence time, leading to a gas holdup three times as high as in water.

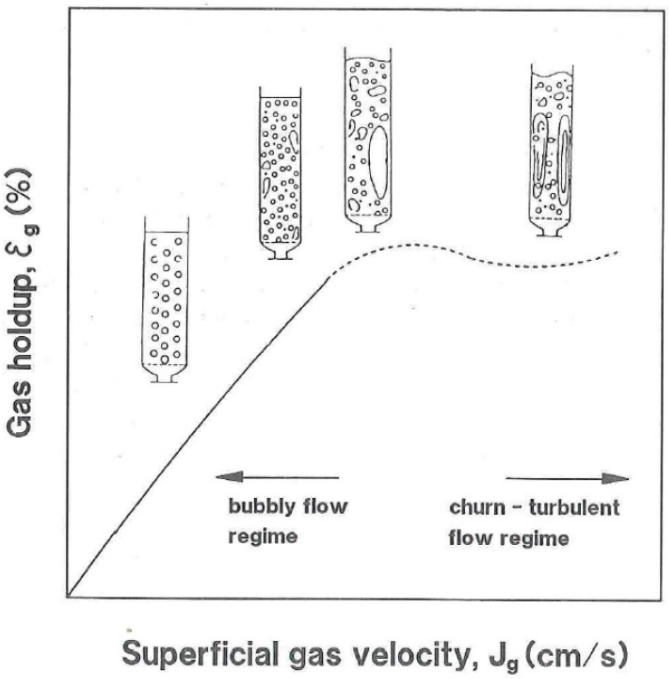

Figure 21: Gas holdup as function of gas flow rate, general relationship [32].

Furthermore, the evolution of bubbles is studied during a time period of one hour for a gas flow rate of

5 and 10 sccm. To this purpose, every five minutes 25 images are grabbed and the average gas holdup is calculated in the same manner as above, where the simulant fluid of choice is an aqueous glycerol (34.2 wt%) solution. The resulting graph is displayed in Figure 22.

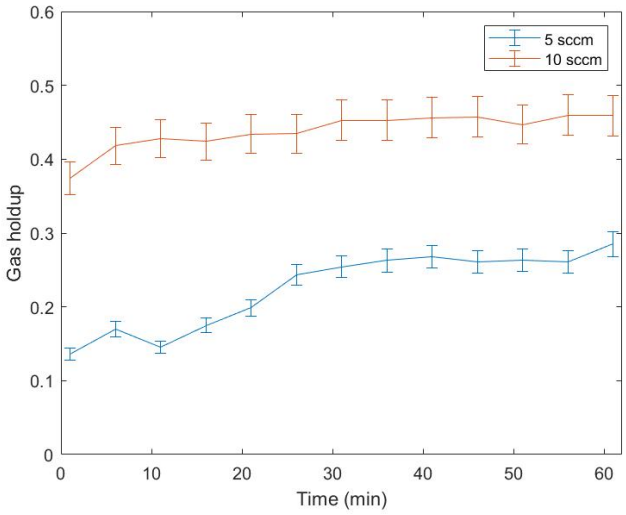

Figure 22: Plot of the gas holdup in an acqueous glycerol (34.2 wt%) solution as function of bubbling time for 5 and 10 sccm gas flow rate.

From this graph it can be visualized that for both inspected gas flow rates a more or less constant gas holdup is reached after 30 min of bubbling. The evolution of the gas holdup over time has also been studied for higher gas flow rates. However, some complications arose with the grabbed images and are therefore not included in Figure 22. The reason for this is that when Q_g is further increased, it becomes more difficult for the bubble algorithm to distinct between the bubbles. An instantaneous image where bubble detection fails at $Q_g = 50$ sccm is shown in Figure 23. From this figure it can be observed that due to the enormous amount of bubbles present in the column, too much light is reflected so that no distinction can be made between bubbles in the center of the image. The intensity of the light emission is too high to detect bubbles in this region.

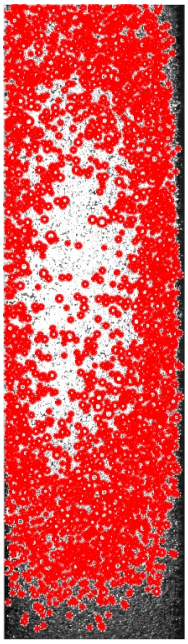

Figure 23: An instantaneous image of the bubble column at $Q_g = 50$ sccm. Due to the large number of bubbles, the measured intensity is too high to properly detect the bubbles in the center of the image.

4.1.2 Height in the bubble column

Prior to the final measurements, the knowledge about the behaviour of bubble-particle transport as a function of the height in the bubble column is of importance to reduce the amount of experiments that are primarily focused on the effect of particle size and gas flow rate. It is assumed that the hydrophobic particles are homogeneously distributed throughout the entire volume of the bubble column after sufficient mixing or stirring of the particle-fluid aggregate. This implies that a single measurement on one part of the column, for example the middle, is representative for what happens in other parts of the column, say the top and the bottom. Of course one can not simply assume something without researching it. Therefore, the validity of this assumption is investigated.

In this section the topic will be the difference in rate of particle concentration between three different regions in the bubble column, namely the top, middle and bottom. Each region corresponds to an interrogation window, which is determined by selecting part of the area captured by the camera. Since both the camera and the laser are elevated relative to the rack that holds the bubble column (see Figure 10), this allows to inspect different height levels in the column. The interrogation window is determined by the area of maximum emitted light intensity caused by the illumination of the laser sheet. In Figure 24 a schematic representation of the bubble column is depicted, with the three interrogation windows presented.

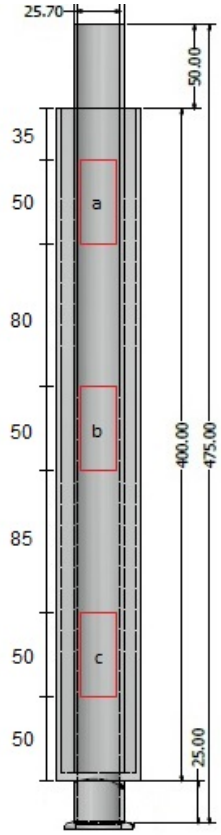

Figure 24: Schematic of the bubble column. The red rectangles represent the interrogation windows at the top (a), middle (b) and bottom (c) position in the column. All values are displayed in mm, and the size of the interrogation windows is 50 x 25 mm.

Throughout the experiments the gas flow rate is set to 25 sccm, the liquid is an aqueous glycerol solution (41.6 wt%) and the particle size of the Nile Red fluorescent polystyrene particles is 0.1–0.3 µm in diameter. Since this series of measurements serves as the first serious concentration experiments, the choices regarding the flow, fluid and particle size have the following purposes, respectively:

- investigating the effect of the amount of bubbles on the accuracy of the measured concentration,
- particle extraction rate behaviour when dealing with a more viscous liquid than water,
- possible complications of particle concentration detection for the smallest size range of particles available.

The measurements are performed during a time period of one hour, where 50 images are grabbed and processed every 5 min to determine the evolution of the measured intensity of the particles over time. The results are displayed in Figure 25. On the y-axis the measured fluorescent intensity in the interrogation window is in units of counts and can be converted to a relative concentration value with the help of a calibration curve (see Figure 18). However, to clearly indicate that it is not particle concentration but fluorescent intensity that is measured here, this conversion is only applied to compare experiments to the model results in Chapter 4.2 below.

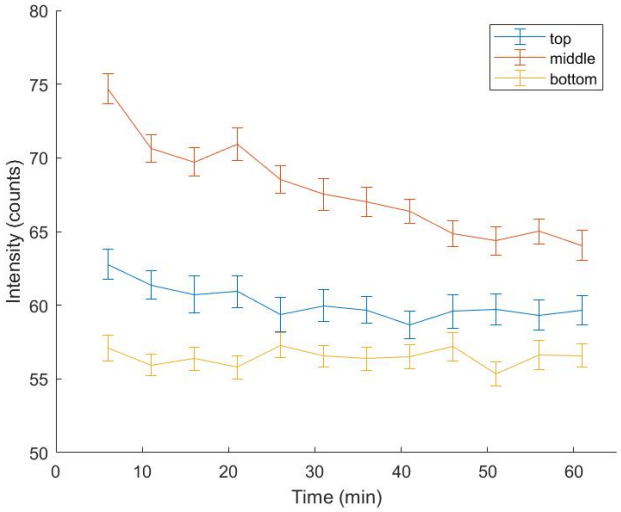

Figure 25: Measured intensity in three different parts of the bubble column during a 60 min bubbling experiment at 25 sccm. The liquid is an aqueous glycerol (41.6 wt%) solution.

The accuracy of the intensity values is determined by their standard deviation. For example, when 50 images are grabbed in rapid succession, then the standard deviation of those 50 images determine the measurement error at a specific time step. For the three repeated experiments investigating three parts of the bubble column, the starting concentration at the top and the bottom was the same. The initial concentration in the middle of the column was slightly higher to check whether this would be noticeable. Indeed, in the middle of the column, more fluorescent intensity is detected than at the bottom and top of the column. For the two inspected interrogation windows at the bottom and the top with the same starting concentration, the gradients of the measured intensity are very similar, with intensity values fluctuating closely around 60 ± 5 counts. This strongly suggests that different parts of the column need not be considered, as the intensity profiles that result show identical behaviour.

4.1.3 Hallimond tube

The Hallimond tube is a device that collects particles that reach the top of the column when entrained by bubbles. Once collected by the tube, the particles are trapped, but how effective is this process? This will be the topic discussed here.

To establish the efficiency of the Hallimond device, an experiment is carried out that shows the amount of particles collected before and after bubbling for 60 min at 15 sccm. The largest fluorescent polystyrene particles with an average diameter of 2.11 µm were used to ensure proper visualization. The extraction of the water-particle mixture present in the Hallimond tube is possible because the tube is equipped with a drain valve. The contents of the collected fluid could thereafter be captured by the LIF detector. With the help of MATLAB, an algorithm is constructed to remove noise and apply thresholding to the grabbed images. The script that is used to perform these operations is given in Appendix A.3. The results for said time intervals are given in Figures 26 and 27.

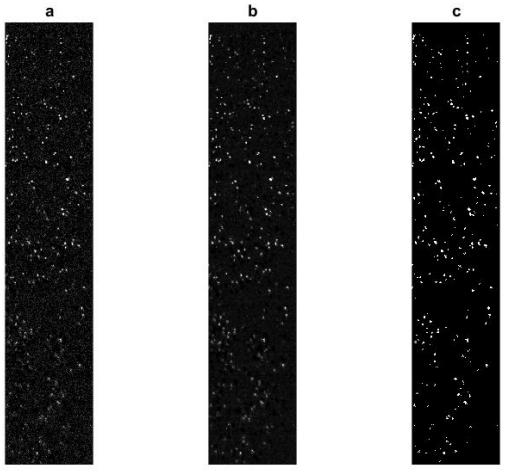

Figure 26: Water-particle solution collected from the Hallimond tube before bubbling ($t_b = 0$). The original image (a) is processed to remove noise (b) and apply thresholding (c).

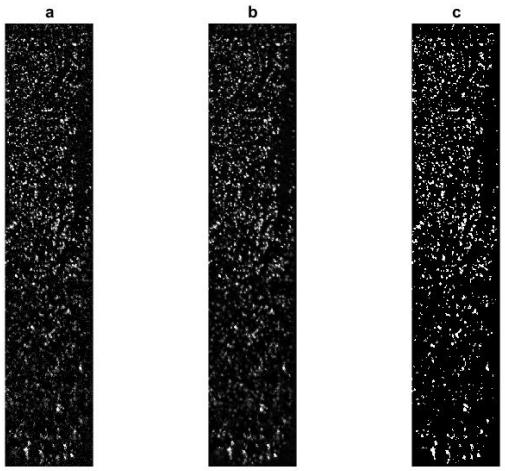

Figure 27: Water-particle solution collected from the Hallimond tube at bubbling time $t_b = 60$ min, gas flow rate $Q_g = 15$ sccm. The original image (a) is processed to remove noise (b) and apply thresholding (c).

It is interesting to see that already at bubbling time $t_b = 0$ quite some particles have accumulated in the Hallimond tube. Therefore, it must be noted that it is the intention that before bubbling begins all the particles are located somewhere in the column. This means that the particles are added to the fluid before the Hallimond tube is attached to avoid as much particles already absent from the column during the bubbling process. Nevertheless, apparently some particles find a way to exit the column without interacting with a single bubble.

To quantify the increase of collected particles after 60 min of bubbling, thresholding is the chosen method. The fluorescent particles, having a higher intensity than the fluid they reside in, can be separated from the background to measure the amount of collected particles as pixels. A relative particle concentration can then be calculated and is determined to increase from 1.6% before to 7.1% after bubbling, implying that the Hallimond tube functions as a device for particle collection.

On a final note, one must be very careful when calculating exact concentration values from fluorescent measurements. The particle sizes studied in this project are sufficiently small that it becomes impossible

to distinct clearly single particles. In fact, the detected light comes from a closely grouped collection or cluster of particles, meaning the dimensional aspect of the particles is lost. Therefore, this method of determining a relative concentration by thresholding is only used to indicate that bubbling accelerates the process with which the Hallimond tube filters out the particles. In the following subsections the method that is introduced here does not work, so for comparison of the data the measured fluorescent intensity is inspected instead.

4.1.4 Particle extraction measurements

The parameters that are investigated to influence particle collection are the gas flow rate and particle size. To study the collection process the measured intensity of the particles in the middle area of the column is tracked during bubbling. It is expected that the intensity will decrease when bubbling time increases since particles are collected and captured by the Hallimond tube at the top, as was confirmed in Chapter 4.1.3. However, here the fluid the particles reside in is not water, but a more viscous aqueous glycerol (34.2 wt%) solution.

The polystyrene particles are fluorescent, meaning LIF is the technique of choice to detect the particles, with the following average diameters: $\overline{d_p} = 0.25$, 0.53, 0.87 µm. Before the experiments were conducted, the prerequisite steps were carefully carried out such that the scaling, background subtraction and sheet processing of the system were performed as thorough as possible (see Chapter 3.3.2). Similar to the bubble measurement depicted in Figure 22, the bubbling is started one minute prior to the first images are grabbed to avoid any largely fluctuating values appearing in the data due to the rapidly changing flow. A possible reason for this could be that the particles are not distributed completely homogeneously in the column prior to bubbling, since the particles are added at the top. From bubbling time $t_b = 1$ min and on, every five minutes 50 images are grabbed during a measurement time of one hour. Figure 28 provides the data of the measured intensity of the smallest researched particle over time for four different gas flow rates, where the fluid under consideration is the aqueous glycerol (34.2 wt%) solution as mentioned. Here, for all investigated gas flow rates it cannot be said if the intensity at $t_b = 1$ min is different or not compared to $t_b = 61$ min, since the intensity gradients seems to be fluctuating around a constant value. This is unexpected because the decrease of particle concentration in the column should be noticeable within a bubbling time period of one hour.

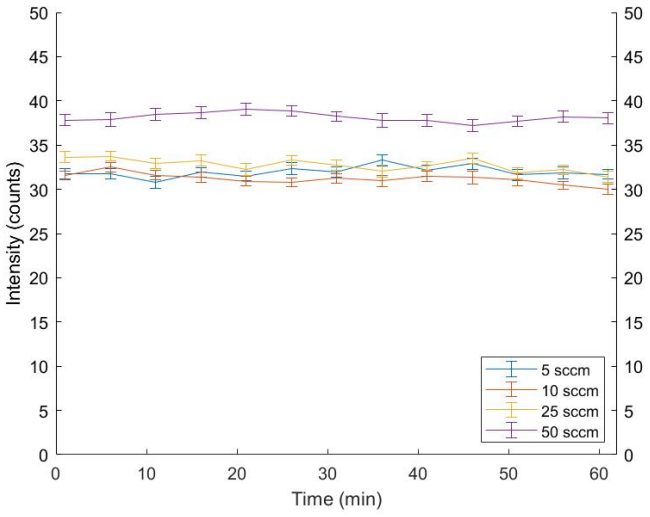

Figure 28: Plot of fluorescent intensity during bubbling at different gas flow rates in aqueous glycerol (34.2 wt%) solution, average particle diameter $\overline{d_p} = 0.25$ µm.

The initial particle concentration prior to bubbling for the four experiments shown in Figure 28 is in each case 12.5 µL diluted in 10 mL water. The solution is added in segments of 2 mL to the column to establish the calibration. The interrogation window that has been set as the area of interest for all 12 measurements is of size 40 mm by 25 mm.

The experiment is repeated for the particle with average diameter $\overline{d_p} = 0.53$ µm. Considerable effort has been put into mimicking the previous experiment so that different outcomes are primarily caused by the change in particle size rather than experimental inaccuracies. What is meant by this is that for every measurement the content of the bubble column needs to be emptied and cleaned in order to start the next experiment with the same starting concentration. After cleaning, it is impossible to place the setup in exactly the same spot it was in, but a serious attempt was made to limit the displacement as much as possible as it might influence the amount of light that is detected. Figure 29 shows the measured intensity of the medium sized nanoparticles during bubbling at multiple gas flow rates.

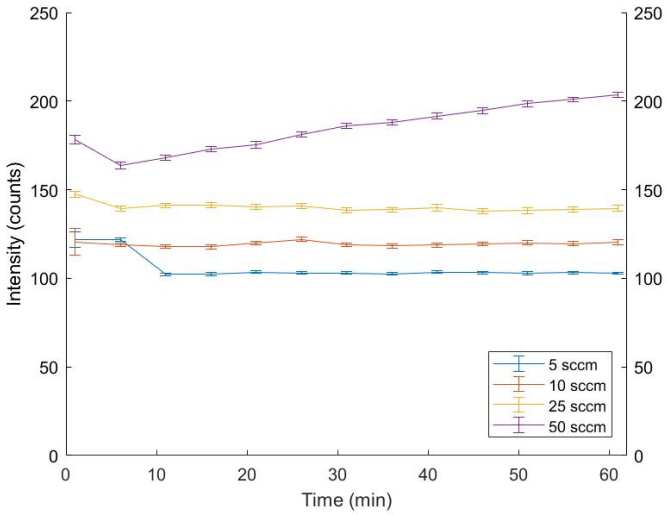

Figure 29: Plot of the fluorescent intensity during bubbling at different gas flow rates in aqueous glycerol (34.2 wt%) solution, average particle diameter $\overline{d_p} = 0.53$ µm.

From this it is observed that similar intensity profiles result for 5, 10 and 25 sccm as in Figure 28 when inspecting the smallest particle size. However, at 50 sccm the measured intensity seems to increase over time. An explanation for this behaviour may be caused by the increase of gas holdup during bubbling for 60 min (see Figure 22), because an increment in the amount of bubbles could cause more bubble surface reflections to add to the detected intensity. Certainly, at larger gas flows such as 50 sccm when a lot of bubbles are present, this phenomena could cause a decrease in the accuracy of the measurements.

Finally, the data of the particles with average diameter $\overline{d_p} = 0.87$ µm is presented in Figure 30. The initial particle concentration set for the experimental results shown below, as well as in Figure 29, is 20 µL diluted in the aqueous glycerol solution. This means that the initial concentration for experiment #5 to #12 is a little bit higher than for experiment #1 to #4, investigating the smallest size of particles.

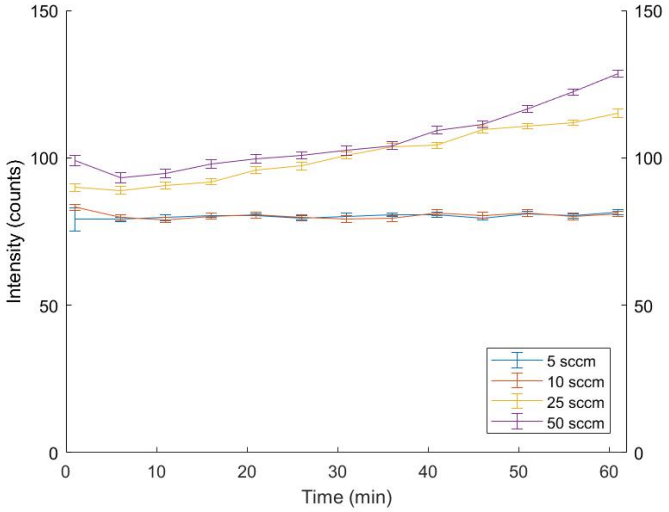

Figure 30: Plot of the fluorescent intensity during bubbling at different gas flow rates in aqueous glycerol (34.2 wt%) solution, average particle diameter $\overline{d_p} = 0.87$ µm.

The observed intensity increment for the medium sized nanoparticles at 50 sccm reoccurs for the largest sized nanoparticles at 25 and 50 sccm (see Figure 30). Although particle size could be of influence, it is more obvious that it is related to other effects such as an increase of intensity contribution due to bubble reflections as a result of the increasing gas holdup mentioned before. However, for the three different nanoparticles this does not seem to play a role at 5 and 10 sccm, since in all cases a more or less constant intensity profile results.

In conclusion, the change in fluorescent intensity of three nanoparticles of different sizes have been investigated when bubbling for 60 min at 5, 10, 25 and 50 sccm. It has come as a surprise that in none of the 12 measurements a decreasing particle concentration is observed. Chapter 5 will go into more detail regarding possible explanations for this counter-intuitive behaviour.

4.2 Results of the model

The model that is used focuses on the interaction between bubbles and particles. To compare the particle flotation recovery R of the analytical model, two experiments were carried out in water at $Q_g = 25$ sccm. The first experiment consists of particles with sizes ranging from 0.1 to 0.3 µm ($\overline{d_p} = 0.25$ µm) and the second experiment investigates particles with sizes ranging from 1.7 to 2.2 µm ($\overline{d_p} = 2.11$ µm). Since the fluorescent intensity serves as the inspected parameter in the experiments, the corresponding value is converted to the relative particle concentration C (%) by means of the calibration. Equation (31) then displays the experimental flotation recovery R (%):

$$R = 100\% - C \tag{31}$$

This equation relates the relative concentration C to the particle recovery R so that the results of the model can be compared to the experimental results. This dependence comes from the fact that R represents the difference between the maximum recovery (100%) and the remaining concentration C.

The model that is introduced in Chapter 2 takes into account various parameters, all of them displayed in Table 2 in Chapter 3. Some of the parameters are material properties (R_p, R_b, ρ_p, ρ_l, μ_l) and others are determined experimentally (R_b, A_c) or set to a certain value (v_p, A, B, Q_g, R^*, t_b). The selected values of the parameters are presented in Table 4 in SI units.

Table 4: Parameters values of the flotation experiments in water. If two values are given, separated by a comma, the first corresponds to the smallest particle size and the second to the largest particle size.

Parameter	Value
v_p	0 m/s
v_b	0.0908 m/s
$R_p = d_p/2$	$0.25 \cdot 10^{-6}/2$ m, $2.11 \cdot 10^{-6}/2$ m
$R_b = d_b/2$	$0.716 \cdot 10^{-3}/2$ m
A	1.25
B	0.6
ρ_p	1050 kg/m^3
ρ_l	1032 kg/m^3
μl	$0.891 \cdot 10^{-3}$ kg/(m $\cdot$ s)
Q_g	$25 \cdot 10^{-6}/60$ m^3/s
A_c	$\pi(25 \cdot 10^{-3})^2$ m^2
R^*	41%, 8.5%
t_b	3600 s

The particle velocity v_p is the most difficult parameter to estimate. Due to the complexity of the flow in the narrow bubble column and the tiny size of the particles, fluctuations in v_b cannot be monitored during the experiments. However, since the bubbles introduce an upwards flow in the center of the column, back-flow at the edges and the small particles following readily the direction of the flow, v_p is assumed to be 0. Even though this might not be entirely accurate, the particle velocity does not have a great influence on the flotation recovery R compared to other parameters in the model. This becomes clear when changing the value of v_p in Appendix C to a disproportionately large value such as 1 m/s, without any change to the shape of the recovery curve. For example, the gas flow rate Q_g, the bubble diameter d_b and the cross-sectional area of the column A_c have a significantly larger impact on the recovery R because they appear directly in the equation for the flotation rate constant (equation (23)).

The bubble velocity v_b is determined by the drift-flux model (equation (12)). The bubble radius $R_b = 0.716 \cdot 10^{-3}/2$ m that is used to calculate v_b is determined from Figure 19 at 25 sccm. The MATLAB script that incorporates the drift flux model and establishes the bubble velocity to be $v_b = 0.0908$ m/s is given in Appendix B.

The parameters A and B determine the induction time and appear in equation (24). A is set to 1.25 and B to 0.6, suggested by J. Ralston et al. [28]. Furthermore, the maximum flotation recovery R^* is set accordingly to agree with the experimental results. Figure 31 below shows the model results of the smallest studied polystyrene particle size (0.1–0.3 µm).

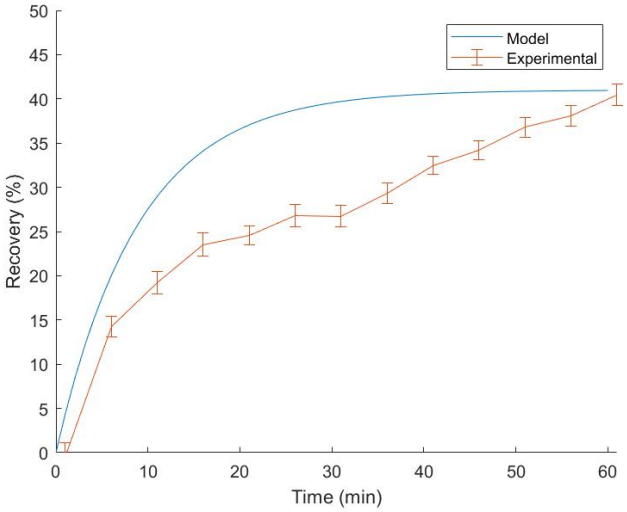

Figure 31: Plot of the particle recovery during bubbling at 25 sccm in water, average particle diameter $\overline{d_p} = 0.25$ µm. The experimental data is compared to a model.

The model that is used to describe the recovery of particles by interacting with bubbles slightly over-predicts the results obtained from the experiment and does not fall within the margin of the error. Additionally, in Figure 32 the experimental and model results of the micro-sized polystyrene particles (1.7–2.2 µm) are depicted.

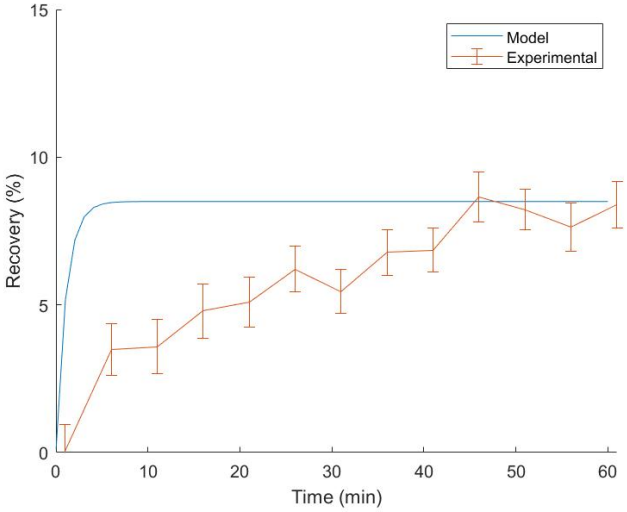

Figure 32: Plot of the particle recovery during bubbling at 25 sccm in water, average particle diameter $\overline{d_p} = 2.11$ µm. The experimental data is compared to a model.

The amount of recovered particles collected by the Hallimond tube is a lot lower for the particles with $\overline{d_p} = 2.11$ µm. Here the model overpredicts the rate of particle recovery even more. To give more insight into how the bubble-particle interaction model is employed, the MATLAB script is provided in Appendix C.

5 Discussion

In this chapter the interpretation of the results of both the experimental bubble and particle experiments are topics of discussion. For this purpose, the discussion is divided into five sections. Chapters 5.1, 5.2 and 5.3 discuss the role that the three separate phases play on the collection efficiency during the experiments. Furthermore, the results of the bubble-particle interaction model and their comparison with experimental data is interpreted in Chapter 5.4. In Chapter 5.5 suggestions are given to improve on the performed experiments for future research.

5.1 Fluids

In the experimental study three different simulant fluids have been selected. For clarification, the liquids and their purpose for the measurements are listed below:

- Demineralized water. The accessibility and low viscosity make this liquid a simple choice to inspect particle and bubble behaviour. Therefore water is used to compare the model results.
- Aqueous glycerol (34.2 wt%) solution. This liquid is used to investigate entrainment of the three fluorescent nanoparticles during bubbling.
- Aqueous glycerol (41.6 wt%) solution. Its high viscosity serves as a useful liquid to study the influence of viscosity on bubble properties like gas holdup and bubble diameter. Also the measured fluorescent intensity during bubbling is studied in different parts of the bubble column with this glycerol solution.

Before the measurements were conducted, it was believed that the aqueous glycerol (34.2 wt%) solution matched the dynamic viscosity of the FLiNaK molten salt. From Table 1 we learn that this is not the case, but that the dynamic viscosity of this solution is considerably lower than of the molten salt composition. This means that the selected fluid is not viscous enough to compare to FLiNaK, and the reason for this mistake is due to a misinterpretation of the simulant fluid data suggested by L. Rozing [14].

5.2 Bubbles

Concerning the bubble measurements, first the gas holdup as a function of the gas flow rate in the bubbly flow regime is inspected when bubbling in water and aqueous glycerol (41.6 wt%) solution. It is observed from Figure 20 that the gas holdup in the more viscous glycerol solution is three times as high as the gas holdup in water at the maximum investigated gas flow rate of 40 sccm, because of the higher bubble residence time in viscous fluids. According to literature [32], the gas holdup increases linearly with gas flow rate in bubbly flow (see Figure 21). Although reasonable agreement with literature is achieved, a perfect linear behaviour is not detected. However, especially for the glycerol solution, a maximum in the gas holdup is visible in Figure 20 around 40 sccm, indicating the transition between bubbly and potential flow.

The bubble diameter for different gas flow rates is studied, because the bubble size is of importance for the model that calculates the particle recovery. From Figure 19 it becomes clear that in water, the bubble diameter has a more or less constant value of $d_b = 0.71$ mm for a gas flow rate ranging from 5 to 40 sccm. In the more viscous glycerol solution this constant bubble size is not observed, but rather a small increment when increasing gas flow. The liquid surface tension could play a role on the detected average bubble size. Since there is no conclusive correlation between the surface tension and the viscosity of the fluids [22], it is difficult to state why a smaller average bubble size is observed in the glycerol solution.

The algorithm that was created takes care of the image processing steps to detect the bubbles as circles. This implicates that the use of this algorithm is only valid for bubbly flow. More information regarding the script for bubble detection can be found in Appendix A.1. Moreover, there is a limit to the algorithm accuracy with which bubbles can be detected, namely 5 pixels in diameter. From empirical observation of the bubbles in the column, also tiny bubbles are present during the bubbling process. Since these bubbles simply cannot be captured it is difficult to include them in the above calculations for the gas holdup and bubble diameter. The gas holdup is not expected to change that much since it concerns small

bubbles, but for the average bubble diameter it could make a difference if the tiny bubbles are present in large quantities.

5.3 Particle extraction

Figure 25 displays the data of particle concentration in different parts of the column when bubbling at 25 sccm. Three interrogation windows are therefore focused on to study possible differences in particle entrainment, their locations presented in Figure 24. When inspecting the measured intensity at the top and bottom of the column, very similar intensity profiles are measured. Their initial concentration is the same, so it makes sense that not much difference is observed. In the middle of the column a slightly higher starting concentration is chosen to check if this would be noticeable. Looking at Figure 25 this can indeed be confirmed. When dealing with narrow vertical bubble columns in the bubbly flow regime, it is expected that the flow over the height of the column will not change drastically [39]. Therefore, it is believed that the occurring variation is due to the different initial concentration used.

The particle concentration during bubbling has also been researched for different particle sizes and gas flow rates. A total of 12 measurements are performed and the intensity profiles are presented in Figures 28, 29 and 30. In most cases the measured intensity remains constant. However, especially when the gas flow is set to 25 and 50 sccm, in some cases the particle concentration seems to increase over time. This is the opposite effect of what is expected and two possible reasons that could account for this lack of declining measured intensity over time are discussed below. But first another observation from the results is addressed. Looking at the collected data, for all three particles a similar trend is emerging. This trend can most clearly be seen in Figure 29, and it concerns the subtle increase in measured intensity when gas flow is increased. A possible reason for this is that reflections by the bubbles intensify the amount of fluorescent light that is received by the detector. Increasing the gas flow means more bubbles are present, which leads to a higher measured intensity.

The discussion regarding the absence of a decreasing measured fluorescent intensity over time gives rise to investigation of the change of gas holdup during the measurement time of one hour. In Figure 22 this is displayed for 5 and 10 sccm, and during the first 30 minutes of both experiments a steady increment of the gas holdup is recognizable, after which the gas holdup remains constant. Moreover, this behaviour is also expected to occur at 25 and 50 sccm, but could not be presented due to overexposed grabbed images for said gas flow rates. This limitation could be caused by the larger viscosity of the glycerol solution increasing the bubble residence time significantly, since the algorithm has no issue with detection of bubbles up to 50 sccm when water is selected as liquid. The reason that the bubble residence time, or bubble rising time, increases with liquid viscosity comes from the theory of the drift-flux model discussed in Chapter 2.1.2. As viscosity increases, there is a linear increase in drag force that appears in equation (9). The increase in drag force shows an opposition to the motion of the bubbles through the liquid acting parallel to the direction of relative motion, hence causing the bubbles to rise at a much slower rate.

Another reason that could cause the lack of decreasing measured intensity over time is the gas inlet temperature. Because the gas flow is injected at $T = 0$ °C [35] and the starting liquid temperature is room temperature, the liquid is expected to cool down when gas flow is introduced at the beginning of the experiment. A consequence of this temperature difference that has been completely overlooked, is that the viscosity increases with a decreasing temperature [40]. When the viscosity increases, the gas holdup rises due to a longer residence time of the bubbles, as suggested by the previous point made. Another explanation could be that the bubbling system does not provide the same amount of bubbles all along. After the experiments it is observed that some liquid seeps through the bubble sparger into the gas chamber, which may affect the gas flow. As mentioned previously, more bubbles mean more measured intensity because of the bubble reflections. Furthermore, the more viscous the fluid, the more sensitive it is to temperature change [40]. The use of the investigated aqueous glycerol (34.2 wt%) solution, being much more viscous than water, could explain why the measured intensity remains constant or even increases and a decrease in measured particle intensity is not observed.

5.4 Model

A model is constructed to compare the experimental results. Two experiments with the smallest and largest inspected polystyrene particles are carried out in water at 25 sccm. The results are depicted in Figures 31 and 32. In both experiments the model overpredicts the experimentally determined particle recovery. The particle recovery is calculated by first converting the measured intensity to a relative concentration by means of a calibration curve, and with the help of equation (31) the flotation recovery R is computed. The agreement between model and experiment is better for the smallest particle. The larger particle with sizes ranging from 1.7–2.2 µm show a less steep gradient than the model estimates, especially in the first five minutes of the measurement. The reason that this curve is steeper compared to the model relation for the particle with sizes ranging from 0.1–0.3 µm, is because bubble-particle interaction becomes most effective when the ratio d_b/d_p approaches unity [21].

5.5 Recommendations

To enhance the experience of future researchers conducting experimental work in this research area, some suggestions are presented. The influence of temperature variation on the fluid, due to the lower gas inlet temperature, changes the evolution of bubbles over time and thus measured particle intensity. The resulting increase in fluid viscosity needs to be carefully considered and should not be neglected. The measured increase in gas holdup depicted in Figure 22 suggests that it takes a considerable time for the temperature change to stabilize the gas holdup. It is therefore advised that before the start of an experiment, bubbling is performed for some time without placement of the Hallimond tube. As soon as the change in temperature is small enough such that a constant gas holdup results, The Hallimond tube may be applied and the outcome of the experiment will most likely be more accurate and meaningful. Prior to concentration measurements however, it would be interesting to investigate the temperature and viscosity change of the fluid during the bubbling process.

Throughout this work a lot of emphasis has been placed on the investigation of particle concentration behaviour as a function of the bubbling time. Parameters that have been considered are the particle size and gas flow rate for different simulant fluids. When focusing on a large number of parameters, time management is of importance, especially for measurements that take one hour to set up and calibrate and one hour for the experiment itself. If the change in viscosity and temperature is showed to have a negligible contribution on the particle collection process, it will be more productive to measure for a shorter period of time, say 30 min. It is expected that most particles are collected right after bubbling. This is substantiated by both model and experimental results (see Figures 31 and 32).

The mass balance of particles leaving the bubble column (and possibly reentering from the Hallimond tube) has not been studied in this research. It would be interesting to calculate the amount of particles that exit the column during a certain bubbling time. These particles should then reside in the Hallimond tube. An experimental check could confirm if this is indeed the case and to what extent. This would show how efficient the Hallimond tube really is. On the topic of the Hallimond tube, since there is no option to include this device in the MSFR, more sophisticated particle extraction devices could be researched that serve as a realistic replacement for the Hallimond tube and have the ability to be implemented in the MSFR.

6 Conclusion

Nanoparticles created during the fission process in the MSFR could poison the reaction, cause corrosion, agglomerate on the cold parts of the reactor core and can, to some extent, be prevented by helium bubbling. Therefore, this thesis focuses on an experimental and analytical analysis of particle entrainment in a flotation column. More specifically, how does the recovery efficiency of sub-micron particles change as a function of time and gas flow rate in a bubble column? Extensive research has been conducted to investigate this behaviour.

The introduction of bubbles to remove small particles has two opposite effects. On one hand the particles are filtered out and are collected by the Hallimond tube device so that a decrease of particle concentration can be observed. On the other hand, the low gas inlet temperature of the bubbles cause viscosity fluctuations that oppose this expected declining behaviour, as well as contribute to a less accurate measured particle intensity due to bubble surface reflections. During the first 30 minutes of bubbling these effects play a prominent role, which has become apparent by studying the gas holdup as a function of bubbling time. Inspecting a liquid with a low viscosity (say water) omits this flaw, but the better approach would be to start bubbling until the fluid temperature is constant and then conduct the experiment, such that particle entrainment in viscous liquids can be studied for comparison with molten salt compositions.

Furthermore, a bubble-particle interaction model is compared to particle concentration measurements in water. Looking at the particle recovery rate for two particles with different size ranges, in both cases the model overestimates the rate of particle recovery. For the largest investigated particles of size 1.7–2.2 µm the recovery rate after one hour of bubbling is 8.5%, while the smallest particles of size 0.1–0.3 µm results in a recovery of 41% in the same time period.

This work explains the difficulties regarding understanding of the complexity of the flow in a narrow cylindrical bubble column and discusses the method with which particle concentration experiments are carried out using the LIF technique. Additionally, analysis on the properties of bubbles is performed as a function of gas flow and bubbling time for different simulant fluids. But the real question that remains: will the helium bubbling process be applied in the MSFR to remove unwanted nanoparticles from the reactor core? Since the MSFR is scheduled for operation in 2050, only time will tell.

References

[1] Argonne National Laboratory. Nuclear engineering division: Reactors designed by argonne national laboratory. https://www.ne.anl.gov/About/reactors/early-reactors.shtml, September 2011.

[2] J. J. Duderstadt and L. J. Hamilton. *Nuclear Reactor Analysis*. Wiley, 1976.

[3] G. J. Suppes and T. S. Storvick. The future in nuclear power. Sustainable Power Technologies and Infrastructure. https://www.sciencedirect.com/topics/engineering/natural-uranium, December 2016.

[4] World Nuclear Association. Physics of uranium and nuclear energy. https://world-nuclear.org/information-library/nuclear-fuel-cycle/introduction/physics-of-nuclear-energy.aspx, November 2020.

[5] H. Armstrong, J. Hanania, C. Pomerantz, K. Stenhouse, and J. Donev. Uranium enrichment. Energy Education. https://energyeducation.ca/encyclopedia/Uranium_enrichment, September 2019.

[6] Spring Power & Gas. The pros & cons of nuclear energy: Is it safe? https://springpowerandgas.us/the-pros-cons-of-nuclear-energy-is-it-safe/, December 2018.

[7] Office of Nuclear Energy. 3 reasons why nuclear is clean and sustainable. https://www.energy.gov/ne/articles/3-reasons-why-nuclear-clean-and-sustainable, March 2021.

[8] Nuclear Energy Institute. Land needs for wind, solar dwarf nuclear plant's footprint. https://www.nei.org/news/2015/land-needs-for-wind-solar-dwarf-nuclear-plants, July 2015.

[9] Nuclear Energy Institute. Nuclear fuel. https://www.nei.org/fundamentals/nuclear-fuel/, 2015.

[10] International Atomic Energy Agency. World's uranium resources enough for the foreseeable future, say nea and iaea in new report. https://www.iaea.org/newscenter/pressreleases/worlds-uranium-resources-enough-for-the-foreseeable-future-say-nea-and-iaea-in-new-report, December 2020.

[11] World Nuclear Association. Supply of uranium. https://www.world-nuclear.org/information-library/nuclear-fuel-cycle/uranium-resources/supply-of-uranium.aspx, December 2020.

[12] S. Fetter. How long will the world's uranium supplies last? Scientific American. https://www.scientificamerican.com/article/how-long-will-global-uranium-deposits-last/, January 2009.

[13] SAMOSAFER. Project. https://samosafer.eu/project/, October 2019.

[14] L. Rozing. Out-of-core helium bubbling in the molten salt fast reactor. Master's thesis, Delft University of Technology, August 2020.

[15] E. Capelli. Report static column. Technical report, Delft University of Technology, June 2018.

[16] A. V. Nguyen, P. George, and G. J. Jameson. Demonstration of a minimum in the recovery of nanoparticles by flotation: Theory and experiment. *Chemical Engineering Science*, 61(8):2494–2509, 2006.

[17] N. Mishchuk, J. Ralston, and D. Fornasiero. The analytical model of nanoparticle recovery by microflotation. *Advances in Colloid and Interface Science*, 179-182:114–122, 2012.

[18] Lior C. Goldenberg, Ian Hutcheon, and Norman Wardlaw. Experiments on transport of hydrophobic particles and gas bubbles in porous media. *Transport in Porous Media*, 4(2):129–145, 1989.

[19] Zongfu Dai, Daniel Fornasiero, and John Ralston. Particle-bubble collision models - a review. *Advances in Colloid and Interface Science*, 85(2):231–256, 2000.

[20] C. Kleinstreuer. *Two-Phase Flow: Theory and Applications*. Taylor & Francis, 2003.

[21] R. H. Yoon and G. H. Luttrell. The Effect of Bubble Size on Fine Particle Flotation. *Mineral Processing and Extractive Metallurgy Review*, 5(1-4):101–122, 1989.

[22] S. M. Ghiaasiaan. *Two-Phase Flow, Boiling and Condensation in Conventional and Miniature Systems*. 2010.

[23] J. R. Thome. The drift flux model. World Scientific. https://www.worldscientific.com/doi/10.1142/9789814623216_0007.

[24] D. Lincoln. Why ideal gas law is not that ideal. The Great Courses Daily. https://www.thegreatcoursesdaily.com/why-ideal-gas-law-is-not-that-ideal/, October 2019.

[25] Spherotech. Characteristics of polystyrene particles. https://www.spherotech.com/particle.html, December 2019.

[26] J. Ralston and S. S. Dukhin. The interaction between particles and bubbles. *Colloids and Surfaces A: Physicochemical and Engineering Aspects*, 151(1-2):3–14, 1999.

[27] B. V. Derjaguin, S. S. Dukhin, and N. N. Rulyov. Kinetic Theory of Flotation of Small Particles. *Surface and Colloid Science*, (2):71–113, 1984.

[28] John Ralston, Daniel Fornasiero, and Robert Hayes. Bubble-particle attachment and detachment in flotation. *International Journal of Mineral Processing*, 56(1-4):133–164, 1999.

[29] G. S. Dobby and J. A. Finch. Particle size dependence in flotation derived from a fundamental model of the capture process. *International Journal of Mineral Processing*, 21(3-4):241–260, 1987.

[30] H. J. Schulze. Hydrodynamics of Bubble-Mineral Particle Collisions. *Min. Process. Extractive Metall. Rev.*, 5(1-4):43–76, 1989.

[31] Z. Dai, S. Dukhin, D. Fornasiero, and J. Ralston. The Inertial Hydrodynamic Interaction of Particles and Rising Bubbles with Mobile Surfaces. *J Colloid Interface Sci .*, 197(2):75–92, 1998.

[32] E. Capelli. Notes on flotation. Technical report, Delft University of Technology, December 2016.

[33] R. J. Kedl. The migration of a class of fission products (noble metals) in the molten-salt reactor experiment. Technical report, Oak Ridge National Laboratory, December 1972.

[34] D. T. Limmer, A. P. Willard, P. Madden, and D. Chandler. Hydration of metal surfaces can be dynamically heterogeneous and hydrophobic. Proceedings of the Natural Academy of Sciences. https://www.pnas.org/content/110/11/4200, March 2013.

[35] Bronkhorst. Thermal Mass Flow Meters and Controllers: Instruction manual. EL-FLOW® Select series. https://www.bronkhorst.com/getmedia/257147fc-7f5d-4628-9a47-0533cf68ac08/917099-Manual-EL-FLOW-Select, November 2020.

[36] R. J. Adrian and J. Westerweel. *Particle Image Velocimetry*. Cambridge, 2011.

[37] Spherotech. SPHERO^{TM} fluorescent particles. https://www.spherotech.com/2020%20Product%20Detail%20Pages/Spherotech%20Fluorescent%20Particles.pdf, December 2019.

[38] LaVision GmbH. LIF in Liquid Fluids: Product-manual. DaVis 8.4. https://www.lavision.de/en/downloads/manuals/, October 2016.

[39] G. Besagni, F. Inzoli, and T. Ziegenhein. Two-Phase Bubble Columns: A Comprehensive Review. *Chem En.*, 13(2):1–79, 2018.

[40] K. S. Lee and J. H. Lee. Chapter 6 - hybrid thermal recovery using low-salinity and smart waterflood. In K. S. Lee and J. H. Lee, editors, *Hybrid Enhanced Oil Recovery using Smart Waterflooding*, pages 129–135. Gulf Professional Publishing, 2019.

Appendices

A Image processing

In this section the image processing steps of both bubble detection and particle concentration measurements are explained. For the determination of the bubble gas holdup and sizes a MATLAB script is constructed that detects small bubbles of the 2D images as circles. The script is included in Appendix A.1. In Appendix A.2 a walk-through of the complete list of image processing operations is shown as part of the DaVis 8.4 software package used during the experiments. Additionally, in Appendix A.3 the MATLAB script is given that performs the calculations of particle extraction rates during the Hallimond tube measurements.

A.1 Bubble detection

```
%Script for determining bubble statistics inside the bubble column used
    during experiments
clear all
listing = '<directory>';%set directory
FileNames = dir(char(fullfile(listing,'*.bmp')));%find all .bmp files in
    current directory.

%define cells and crop region
image = cell(length(FileNames),1);
imagecropped = cell(length(FileNames),1);
greyscale = cell(length(FileNames),1);
SE = cell(length(FileNames),1);
Ie = cell(length(FileNames),1);
Iobr = cell(length(FileNames),1);
Iobrd = cell(length(FileNames),1);
Iobrcbr = cell(length(FileNames),1);
bw = cell(length(FileNames),1);
totalbubblearea = cell(length(FileNames),2);
gasholdup = cell(length(FileNames),2);
averagebubblediameter = cell(length(FileNames),2);%second column is
    standard deviation
bubbles = cell(length(FileNames),1);
numberofbubbles = cell(length(FileNames),1);
rect = [780 0 580 2047];%crop region
totalarea = 581*2048;%crop area in pixels^2
conversion = 25/580;%conversion factor from pixels to mm

for i=1:length(FileNames)
  image{i} = imread(FileNames(i).name);%read all images in directory
  imagecropped{i,1} = imcrop(image{i},rect);%crop all images in directory

  %morphological operations
  greyscale{i,1} = rgb2gray(imagecropped{i});%convert image to greyscale
  SE{i} = strel('disk',1);
  Ie{i,1} = imerode(greyscale{i},SE{i});
  Iobr{i,1} = imreconstruct(Ie{i},greyscale{i});%opening-by-reconstruction
      is an erosion followed by a morphological reconstruction
  Iobrd{i,1} = imdilate(Iobr{i},SE{i});
  Iobrcbr{i,1} = imreconstruct(imcomplement(Iobrd{i}),imcomplement(Iobr{i})
      );
```

```
    Iobrcbr{i,1} = imcomplement(Iobrcbr{i});%reconstruction-based opening and
        closing are more effective than standard opening and closing at
        removing small blemishes without affecting the overall shapes of the
        objects
    bw{i,1} = imbinarize(Iobrcbr{i});%thresholding operation

    %detect circles
    [centers,radii] = imfindcircles(bw{i,1},[5 15],'ObjectPolarity','bright',
        'Sensitivity',0.95);%find circles in range [5 15] pixels
    imshow(imagecropped{1,1})
    h = viscircles(centers,radii);%show circles on first cropped image

    %determine gas holdup, average bubble diameter and number of bubbles
    bubblearea = pi*radii.^2;
    totalbubblearea{i,1} = sum(bubblearea);
    gasholdup{i,1} = totalbubblearea{i,1}/totalarea;%gas holdup of 1 image
    averagebubblediameter{i,1} = mean(radii)*2*conversion;%average of all
        bubble sizes in 1 image, in mm (1 pixel = 25/543 mm)
    numberofbubbles{i,1} = length(radii);%number of detected bubbles per
        measurement

    %standard deviation (std) of gas holdup
    totalbubblearea{i,2} = length(bubblearea)*std(bubblearea);%multiply std
        value of bubblearea in each image by number of bubbles (length(
        bubblearea)) in each image
    gasholdup{i,2} = totalbubblearea{i,2}/totalarea;%determine std of
        gasholdup for each image by dividing by the total area of the crop
        region

    %standard deviation (std) of bubble diameter
    averagebubblediameter{i,2} = std(radii)*2*conversion;%add std of radii in
        each image to 2nd column of averagebubblediameter and convert radius
        in pixels to diameter in mm

    %determine bubble distribution
    bubbles{i} = centers;
end

%average over 60 images
meangasholdup = mean(cell2mat(gasholdup(:,1)));%average gas holdup over all
    images at constant gas flow
meanbubblediameter = mean(cell2mat(averagebubblediameter(:,1)));%average
    bubble diameter over all images at constant gas flow
meannumberofbubbles = mean(cell2mat(numberofbubbles));

%standard error of the mean (sem) of gas holdup
std_gasholdup = cell2mat(gasholdup(:,2));%std as calculated in gas holdup
sem_gasholdup = sqrt(sum(std_gasholdup.^2)/length(FileNames)^2);%sem is
    standard error of the mean

%standard error of the mean (sem) of bubble diameter
std_bubblediameter = cell2mat(averagebubblediameter(:,2));%std as
    calculated in for loop
sem_bubblediameter = sqrt(sum(std_bubblediameter.^2)/length(FileNames)^2);%
    sem is standard error of the mean

%standard deviation (std) of the number of bubbles
```

```
std_bubblenumber = std(cell2mat(numberofbubbles));%std of number of bubbles
    in every image
```

A.2 Particle concentration

This section of the appendix explains the different steps that are necessary to perform image processing on data gathered from particle extraction measurements, the primary objective of this research. It includes 32 screenshots of the DaVis 8.4 software operation list, where all actions are carefully explained in order. Moreover, this section serves as a user-friendly guide for future researchers making use of the LIF setup. Personally, I found the manual provided by LaVision thorough but confusing at times. However, it must be said that the enormous amount of operations that the DaVis software package offers for various research purposes simply cannot be discussed in a single manual. Therefore in this guide the focus lies on fluorescent particle concentration measurements in fluids, also denoted as LIF-C. Experiments regarding temperature measurements (LIF-T) have not been investigated and will not be focused on in this discussion, but the consecution will most likely be the same.

The walk-through is divided into five tasks. The subsequent subsections demonstrate these tasks and are respectively: scaling, background subtraction, sheet processing, concentration calibration and experiment. For all the steps discussed below the f-number of the camera is set to its lowest value, namely 1.4. The reason for this is that with this setting the most amount of light reaches the CCD, a desirable scenario considering that the LIF filter blocks most of the light. However, during the scaling part the filter is not used. Try not to operate the laser with high beam intensity when the lowest f-number is selected, for too much light could enter the CCD and the chip might get oversaturated, resulting in a broken camera.

A.2.1 Scaling

Images consist of pixels, which is a universal yet not preferred unit of length. The first step of the image processing is converting the size of the pixels in the images to the actual size of the setup, say in mm. The reason this is done is to make sure that for every measurement an interrogation window (IW) of constant size can be determined. When working with LIF, for scaling of the setup an imaging project should be created. Figure A1 shows the home screen of the DaVis program. An imaging project is marked, named 'scaling'. Left-click on it twice to open the program.

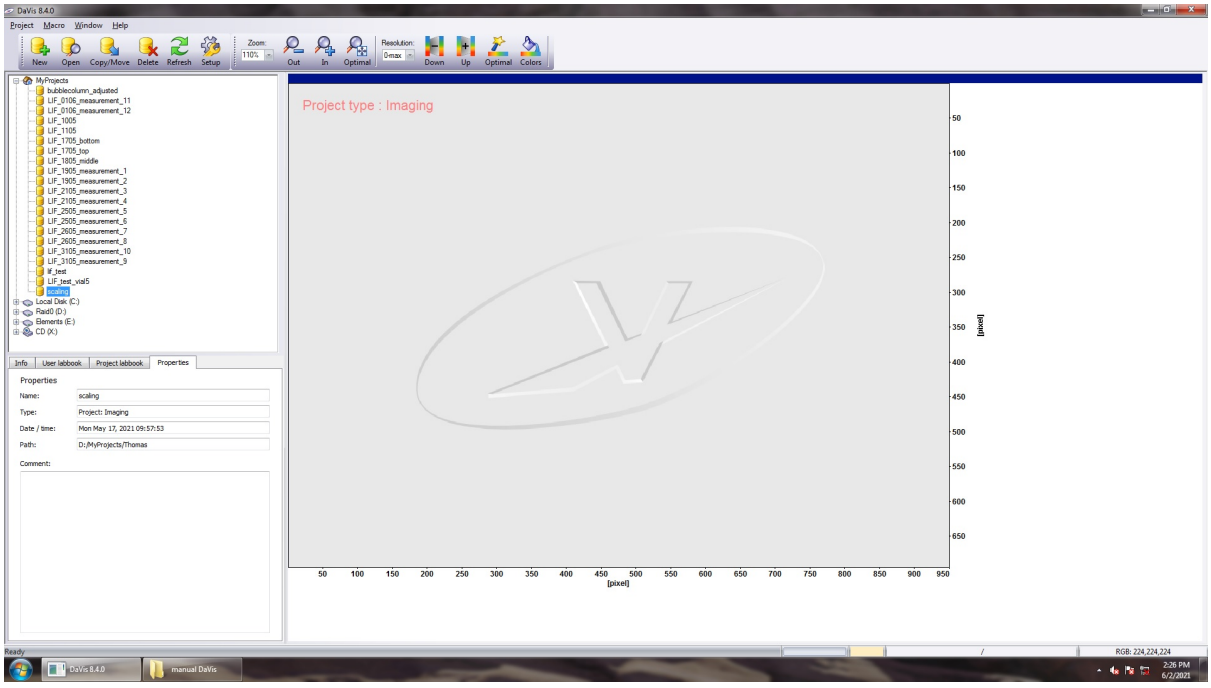

Figure A1

Figure A2 depicts the 'scaling' project, where images of the setup have been taken for multiple experiments. In order to verify the size of the setup a piece of graph paper is taped on the back of the column from the side of the camera. Although use of a calibration plate is a more sophisticated way to capture the size of the system, the square blocks of 10 mm by 10 mm provide a decent measure for scaling.

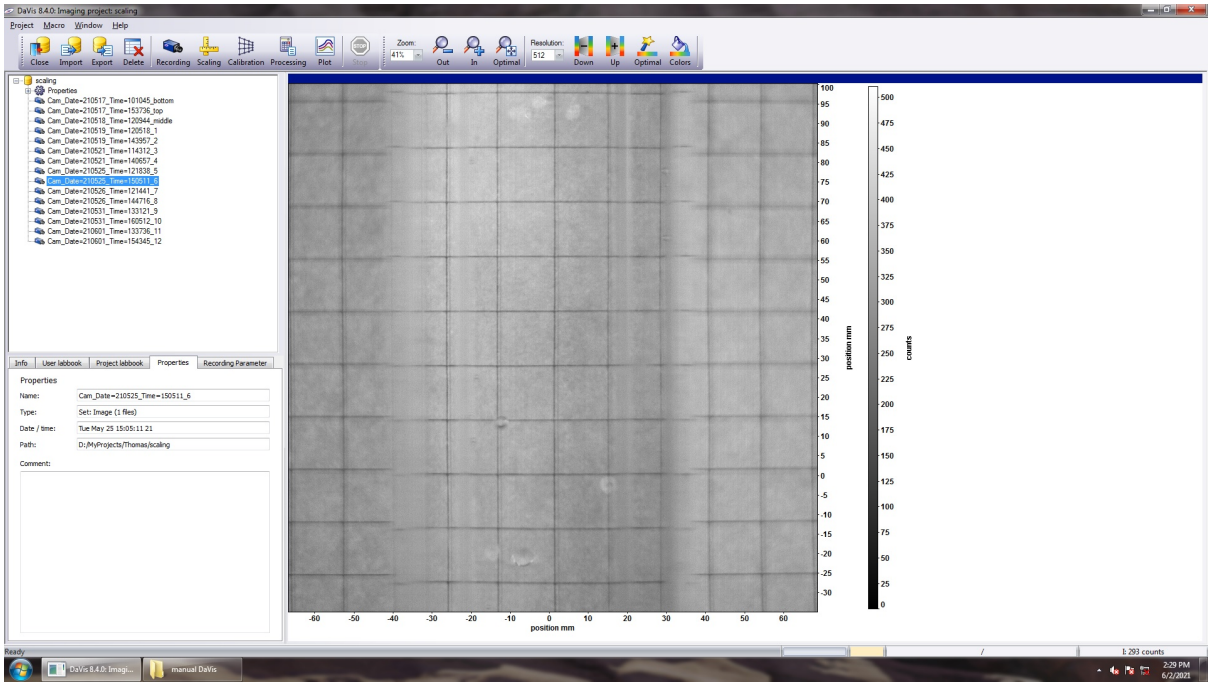

Figure A2

To take an image for scaling, press Recording in Figure A2, the menu that will appear can be seen in Figure A3. Here there is an option to choose either Live Mode or Recording. When selecting Live Mode, it is possible to continuously take new images so that the image can be focused on the blocks on the graph paper by rotating the focus ring.

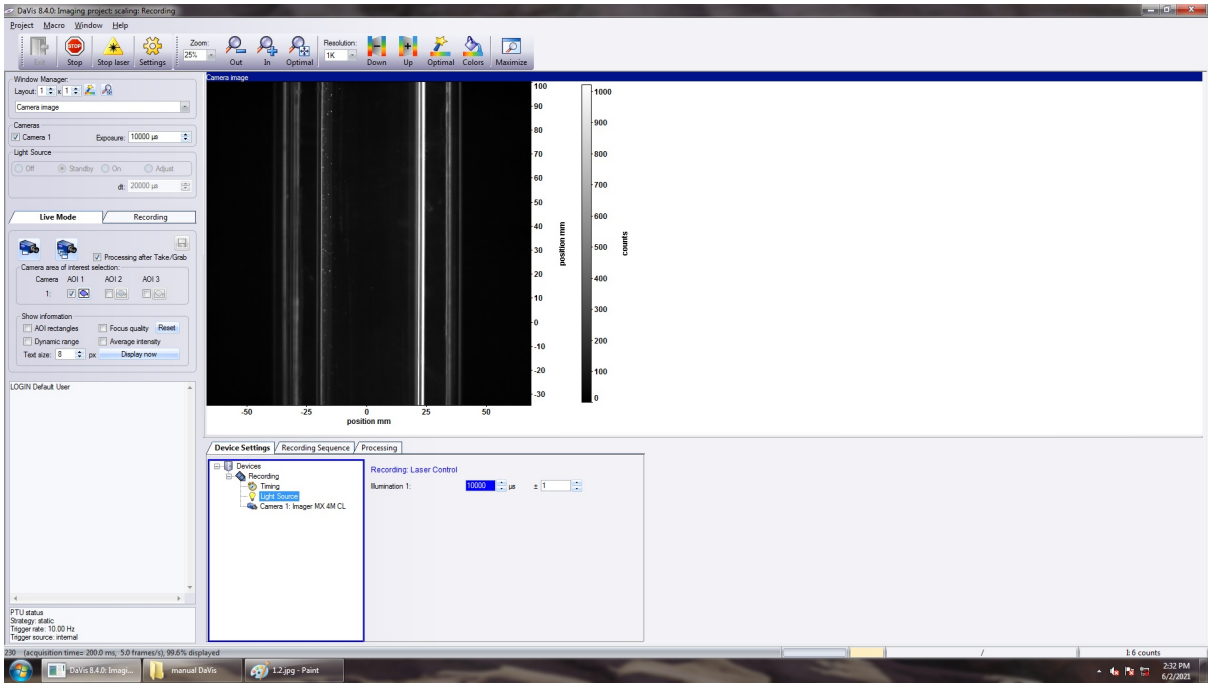

Figure A3

When you are satisfied with the result, select recording. From here you can grab and save images by pressing the selected 'Start the image recording' button in Figure A4. Pressing Exit takes you back and brings you to the place where all grabbed images are collected.

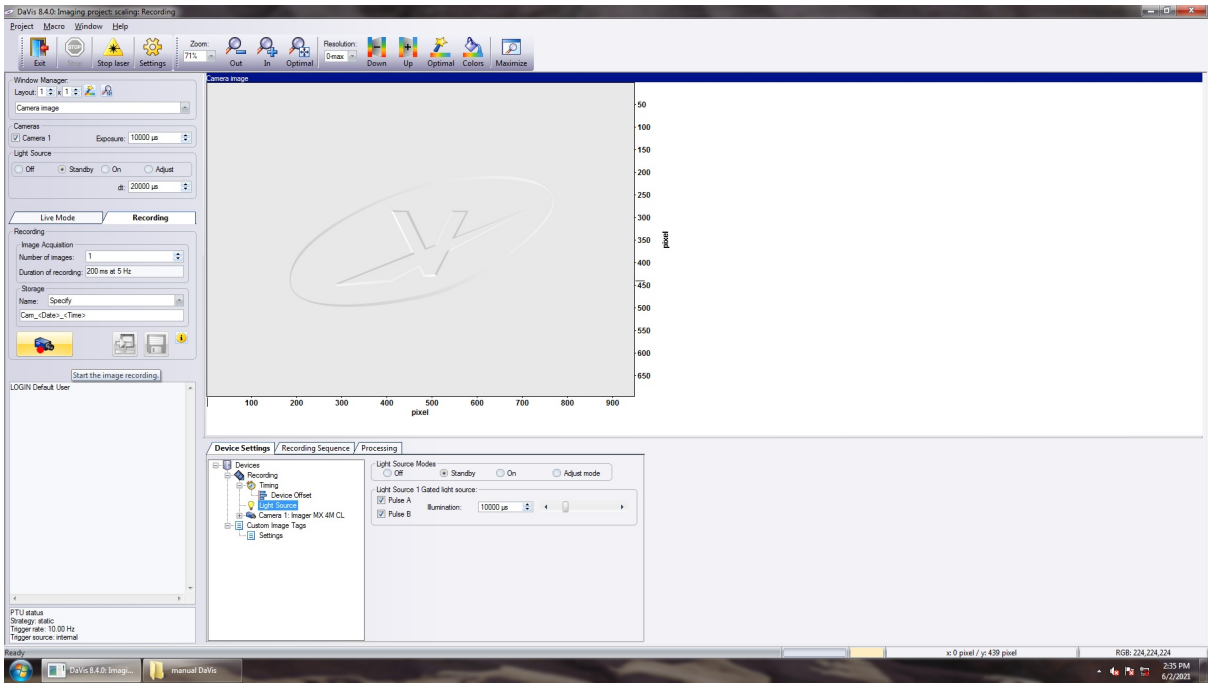

Figure A4

Now that the scaling image has been taken, select a new LIF project. The menu that appears is very similar as before, but because a LIF project is selected, more image processing techniques are available. An example of the full operation list of a performed measurement is depicted in Figure A5.

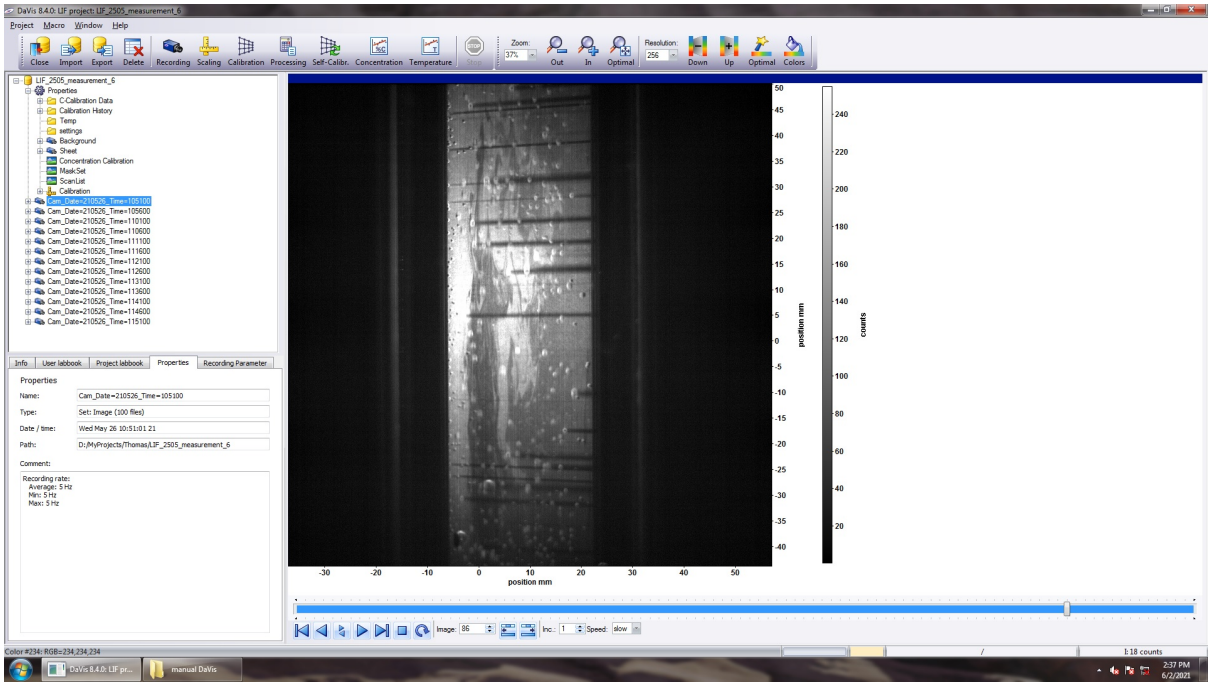

Figure A5

Select Scaling to set the proper scale. From the image directory icon in Figure A6 the image taken in

the 'scaling' directory can be selected. The two yellow dots in the image eventually set the proper scale by left-clicking the most left icon next to 'Scale'. By calculating the pixel distance between the two diagonals of a block and setting this distance to $\sqrt{10^2 + 10^2} = 14.14$ mm the scaling step is complete.

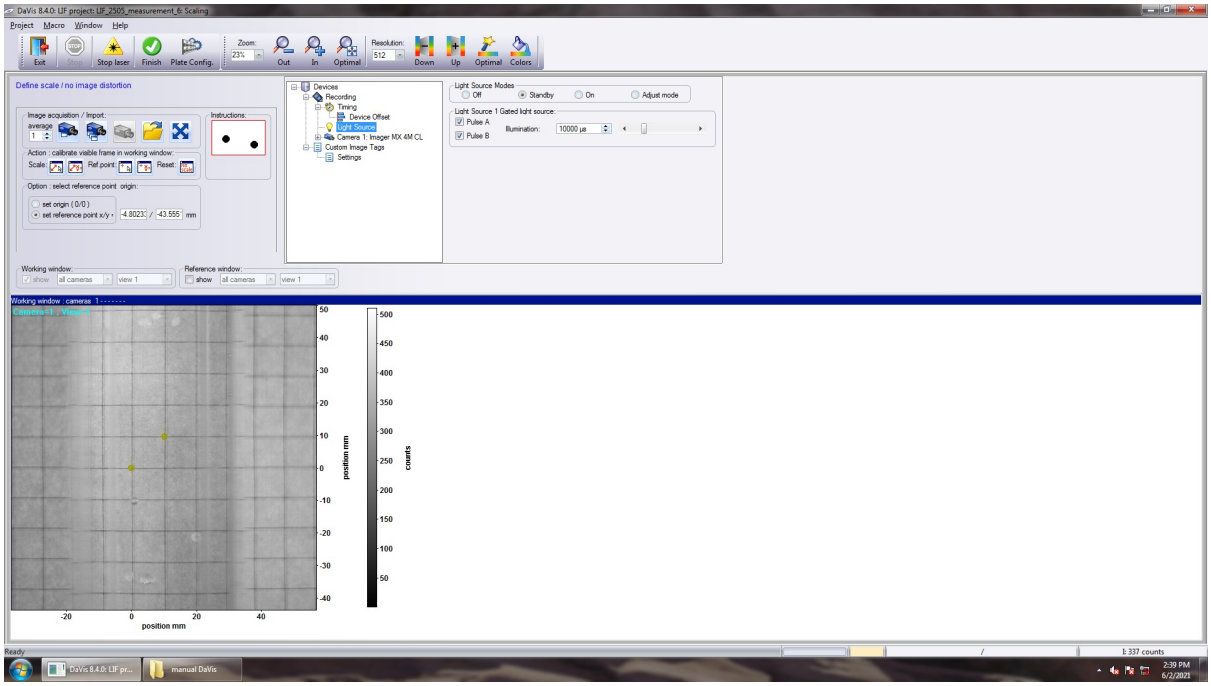

Figure A6

A.2.2 Background subtraction

The next step is to deal with background noise. The camera's dark current and surrounding light add an offset to the signal from the actual experiment. In order to extract the pure LIF signal these offsets are subtracted by grabbing an image with the lens cap on. In order to achieve this, select Recording in Figure A5. As before, the menu that appears is depicted in Figure A7. Under the Recording tab select the following Recording mode: Background images. Now it is possible to grab images for background subtraction with the 'Start the image recording' button. During the experiments 10 background images were grabbed per measurement.

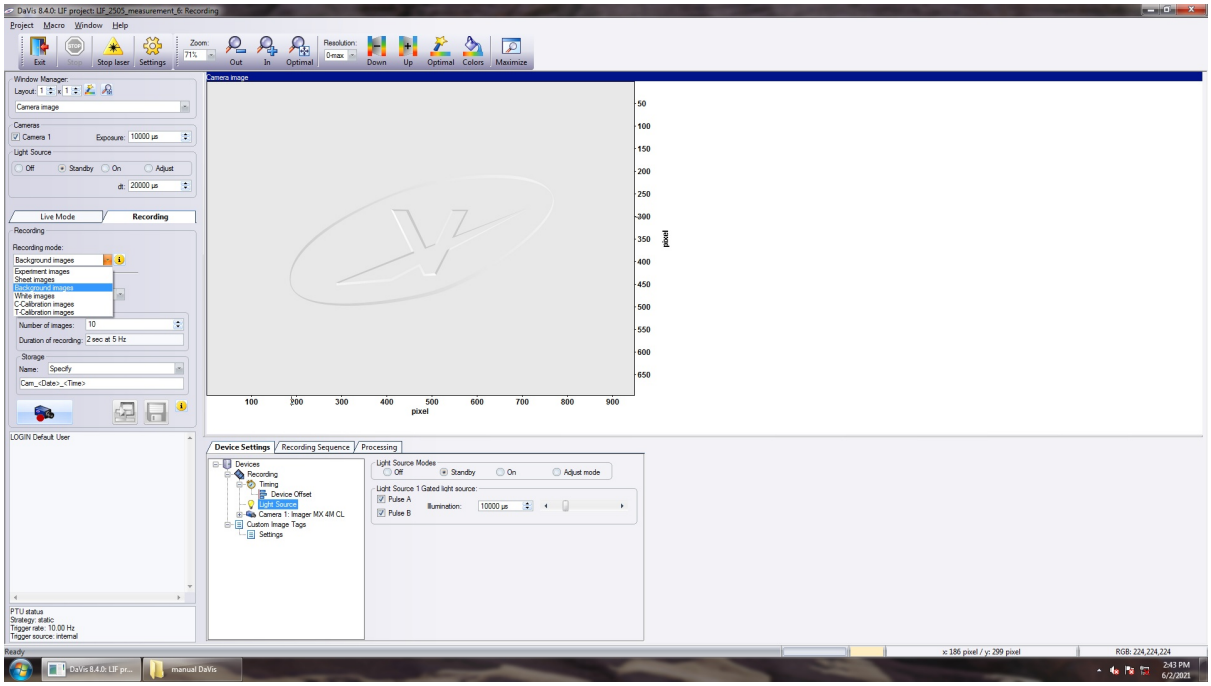

Figure A7

Click exit and in the operation list, under Properties, right-click on Background as indicated in Figure A8. Left-click on Processing.

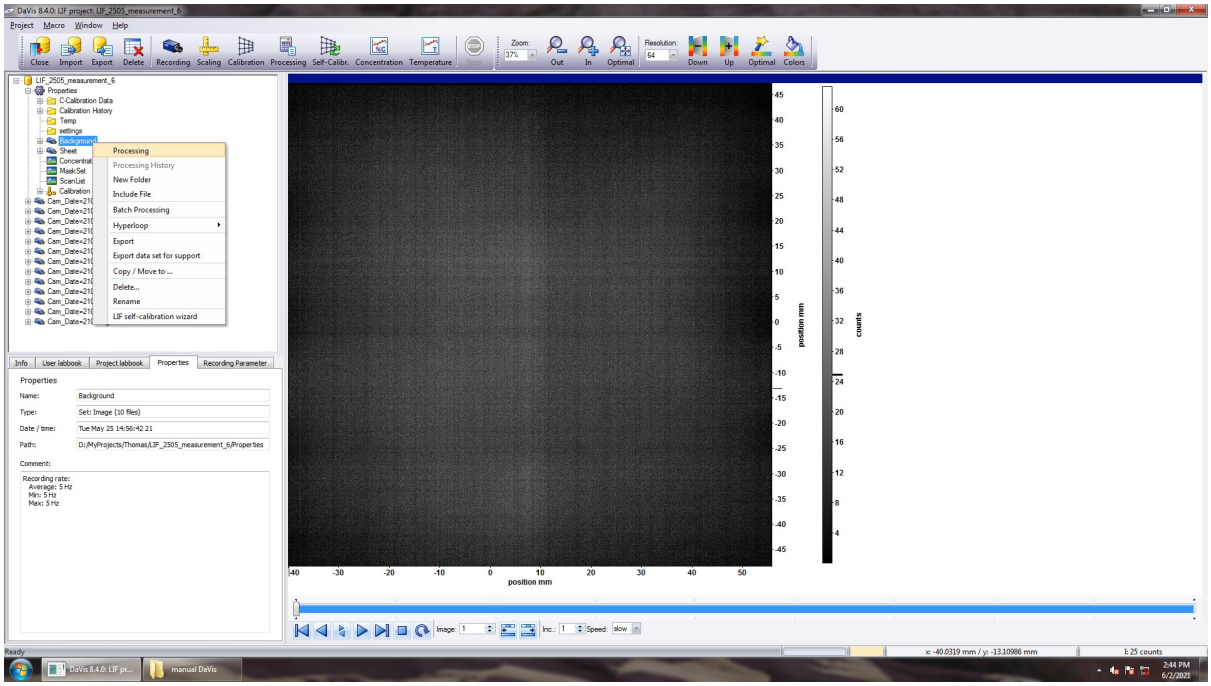

Figure A8

This will take you to the Processing window, shown in Figure A9. From the 10 images that were grabbed, averaging of the background noise is performed. Right-click in the Operation list and hover with the mouse over the following items:

- set operation
- statistics

- sum, average, standard deviation, min, max

Now select Start Processing to start the averaging.

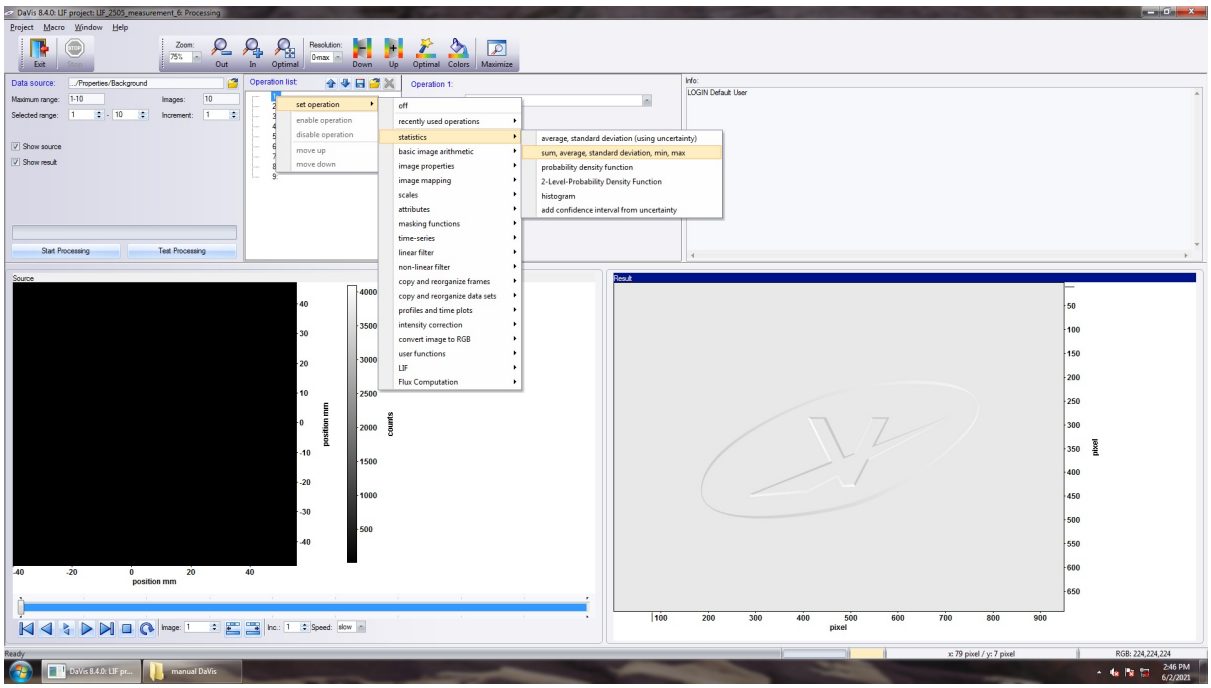

Figure A9

Once complete, press Exit and in the Background folder the averaged image should be present, denoted as Avg. This is shown in Figure A10 below. The image will be used as subtraction of the background noise for all the subsequent steps.

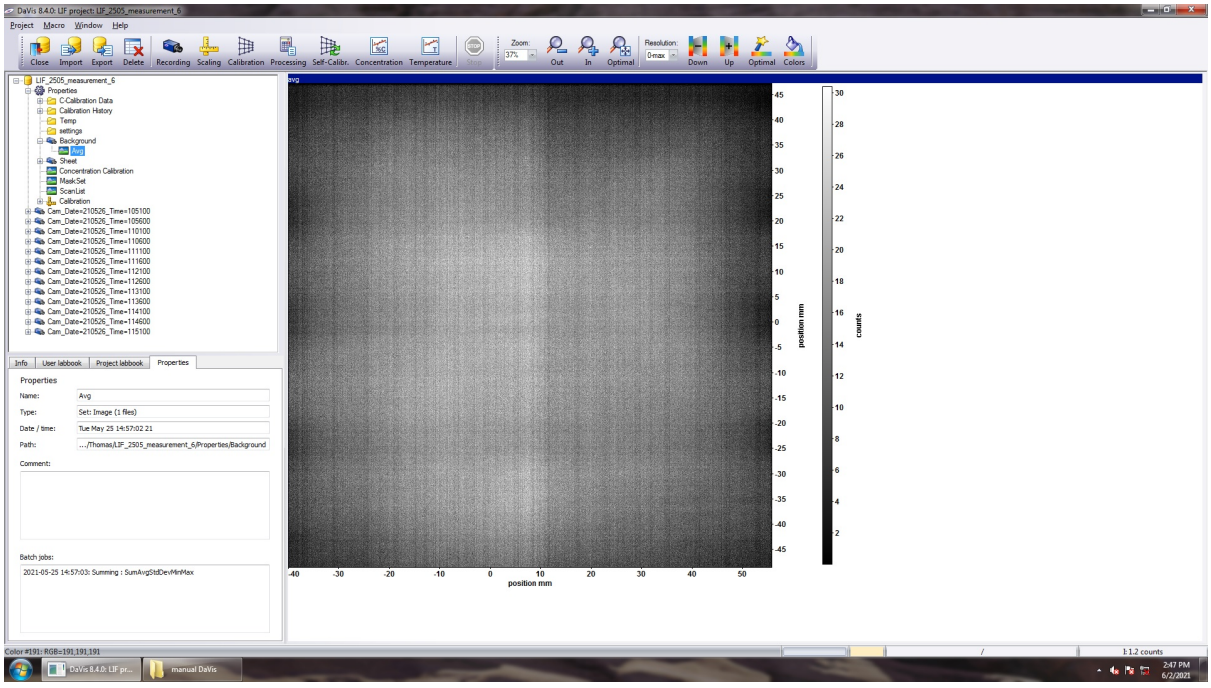

Figure A10

A.2.3 Sheet processing

The third step takes into account the non-uniformity of the laser illumination. In Figure 14 the light intensity distribution is shown to have a Gaussian profile, where in the centre of the light sheet the illumination is maximal. To take care of this non-uniformity, the following steps are carried out. Press Recording again and under the Recording tab select Sheet images as Recording Mode. This is illustrated in Figure A11. Make sure the laser is turned on and the lens cap used for the previous processing step is removed. Also mount the LIF filter on the camera before the image recording is started. Again 10 images for this step will suffice.

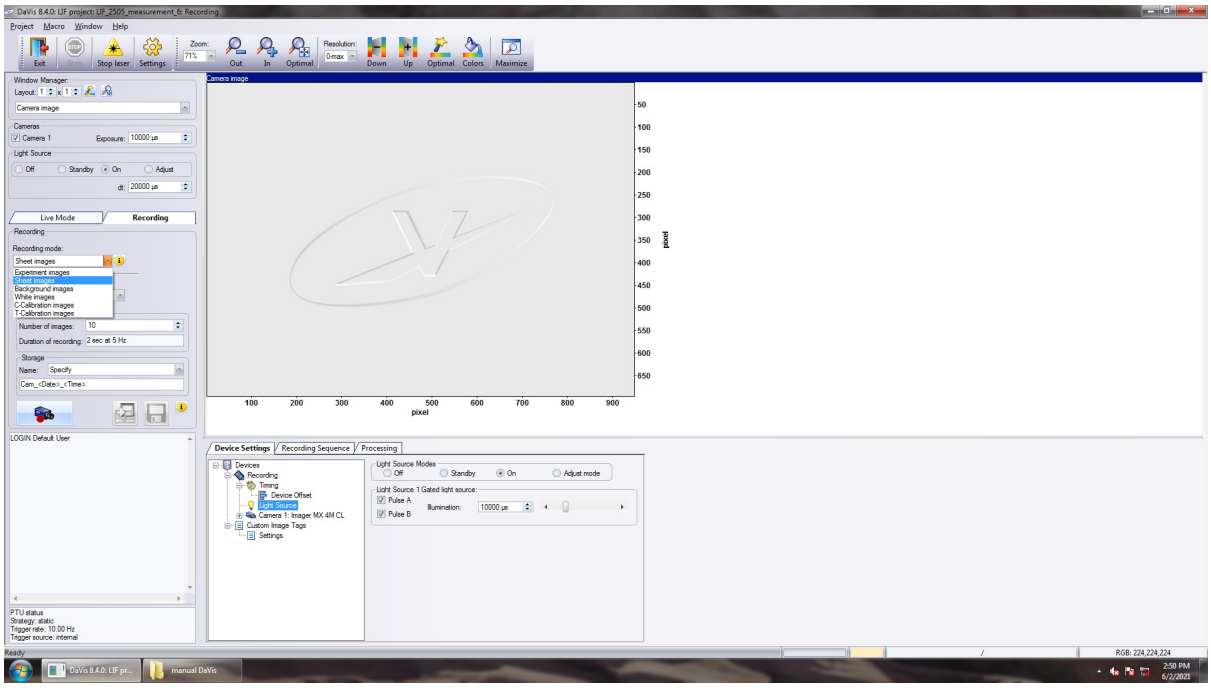

Figure A11

When the sheet images are grabbed, press Exit and right-click on the Sheet folder under Properties and select Processing, see Figure A12.

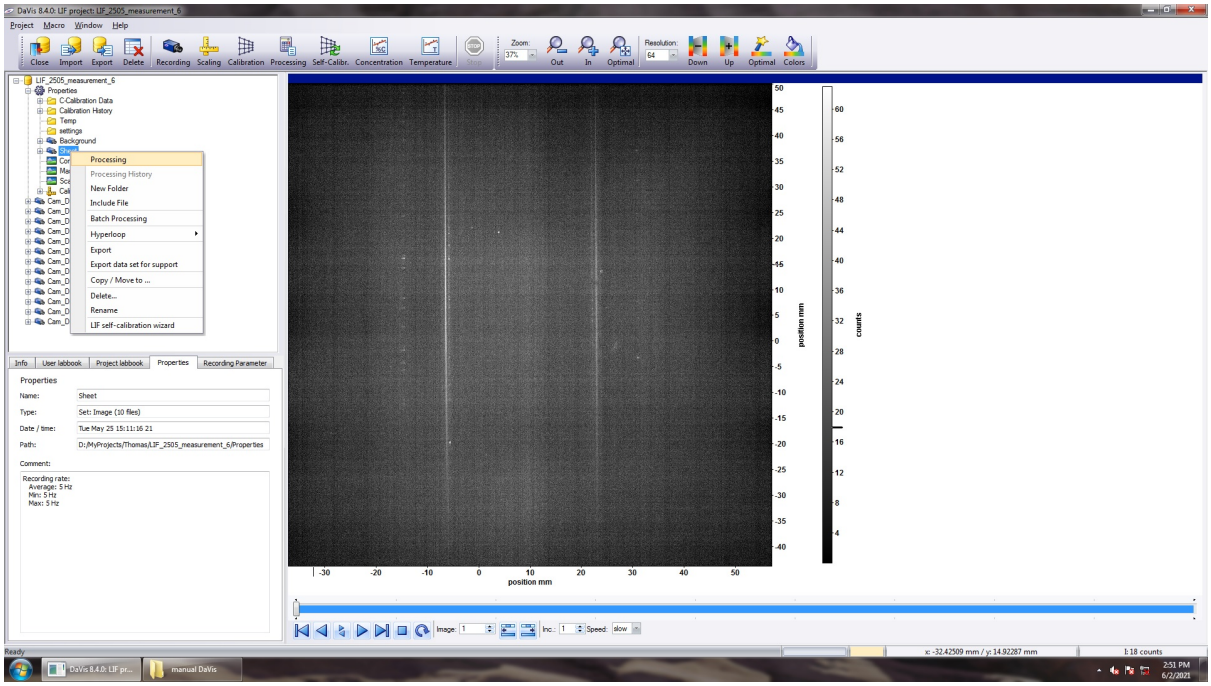

Figure A12

The first operation will again be the averaging of the 10 images, and the second operation introduces the background subtraction. To choose this operation, see Figure A13.

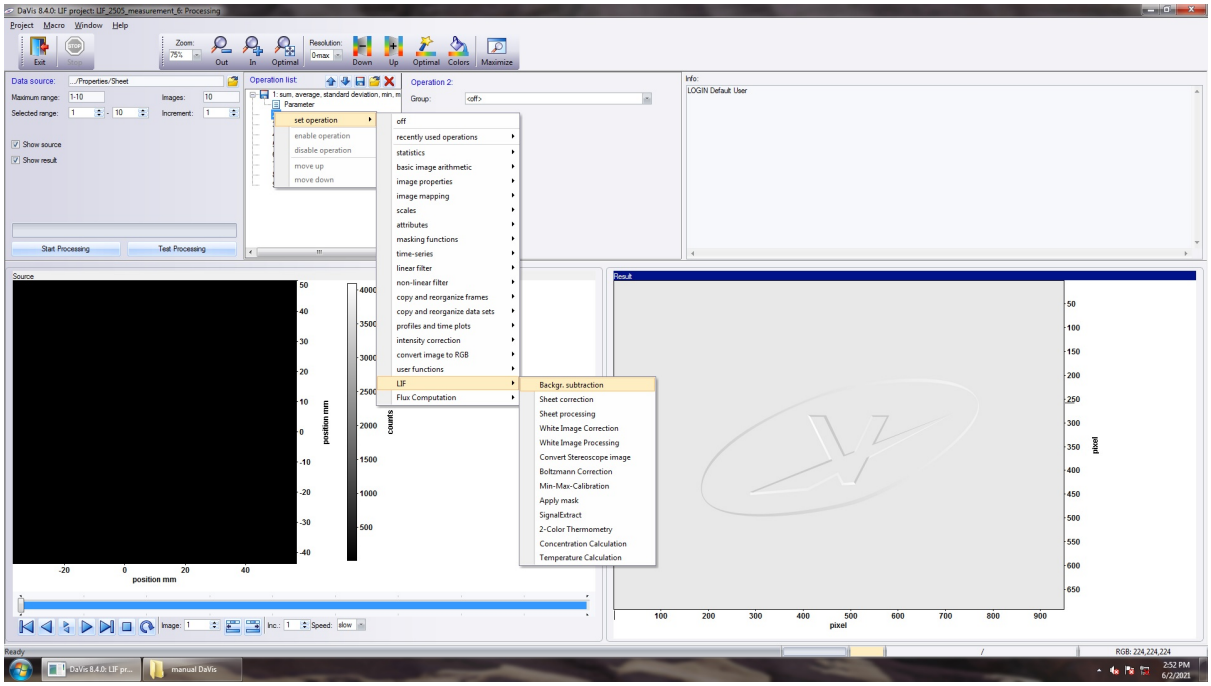

Figure A13

The third operation is processing of the light sheet, and is selected as depicted in Figure A14.

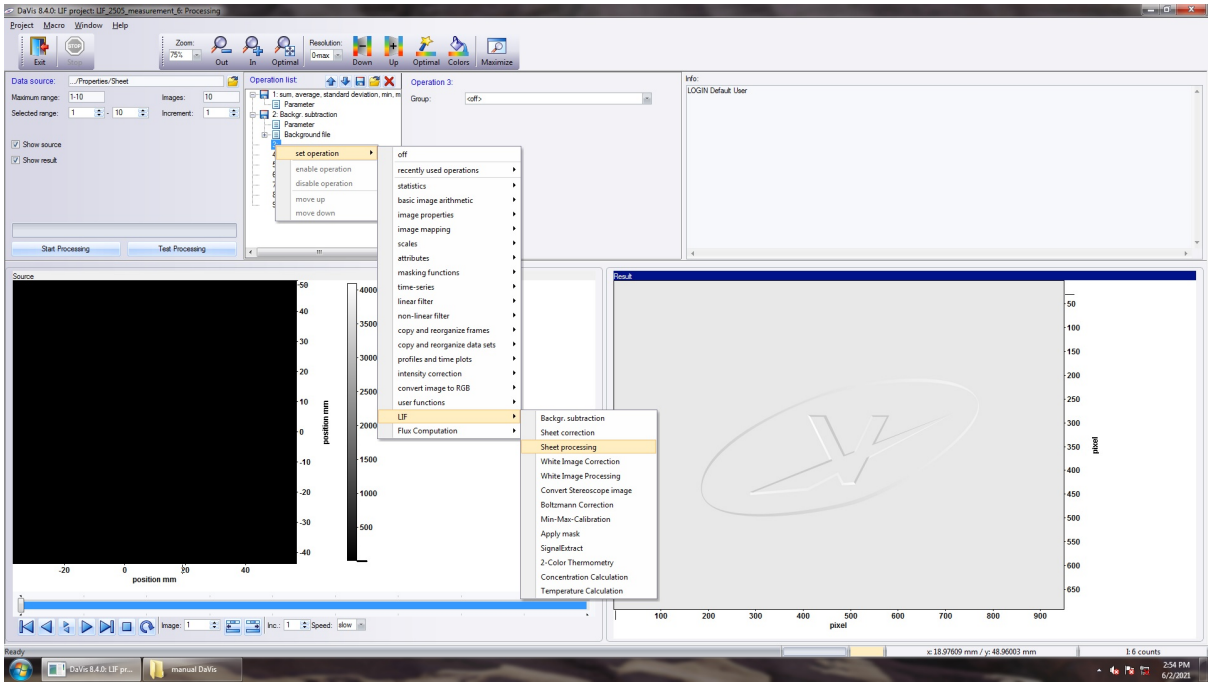

Figure A14

Now that the three operations are selected, press Start Processing. When done press Exit and in the Sheet folder the file SPM-SF is the processed light sheet image, given in Figure A15.

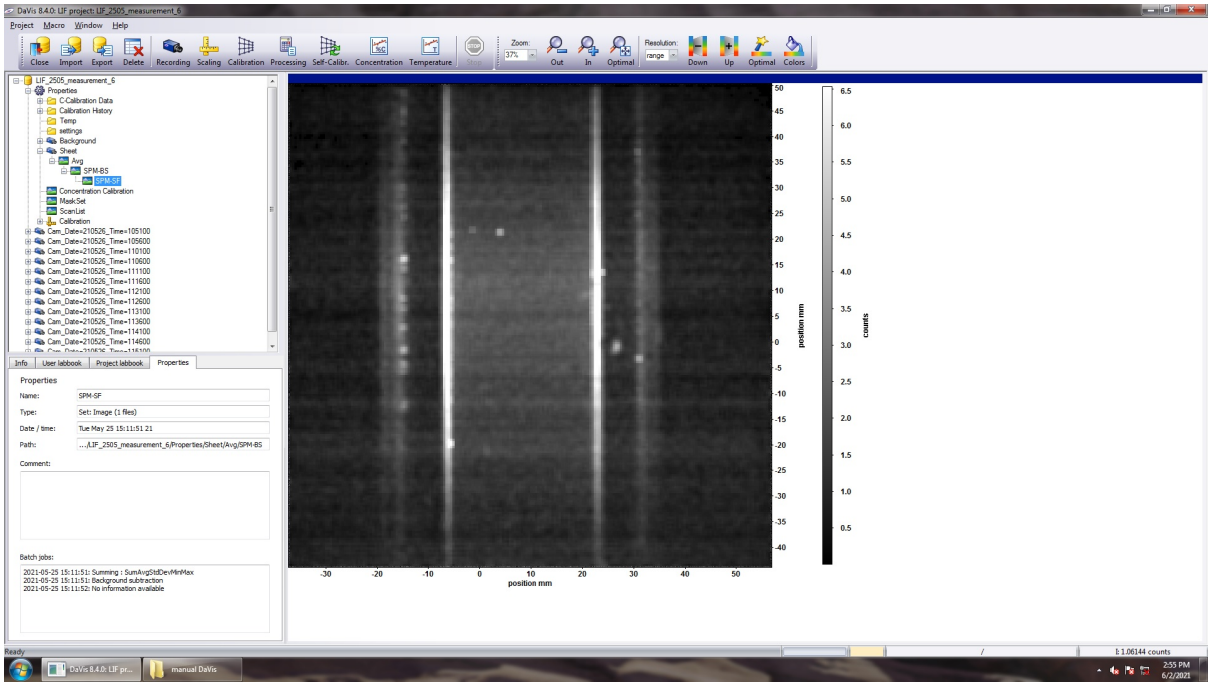

Figure A15

A.2.4 Concentration calibration

Similar as before, head over to the Recording tab and now choose the Recording mode: C-Calibration images. The calibration step is by far the most important and time consuming step. It is important because the predetermined particle concentration is related to the measured intensity that the fluorescent

particles emit as a result of the excitation of the laser light. It is time consuming because essentially the same process is repeated six times. But first let's start at the beginning. As illustrated in Figure A16, select the correct Recording mode.

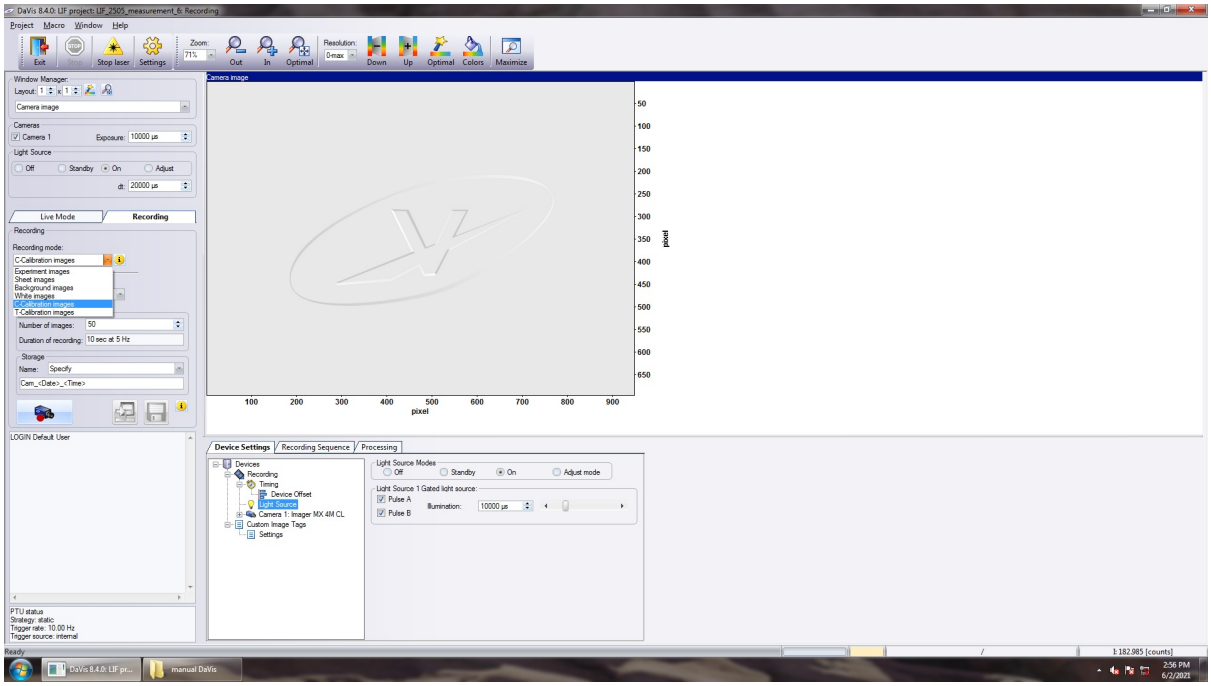

Figure A16

Press Exit and head over to the C-Calibration Data folder. This is where all the calibration images are stored. An example of such a filled directory is shown in Figure A17. Here 6 image recordings with each 50 images are located, the difference between them being the relative added particle concentration to the setup. The aim is to establish a linear (first-order approximated) calibration curve so that during the experiment we can keep track of the relative particle concentration over time. To achieve this, the particle concentration in the column is gradually increased in the following way: 0, 20, 40, 60, 80 and 100% relative particle concentration. Since the volume of added particles (100%) is known, the calibration curve relates the measured intensity to the actual concentration. First, head over to the menu in Figure A16 and start the image recording without any particles present in the column. Make sure the laser is turned on. For the experiments an illumination time of 10 ms is used.

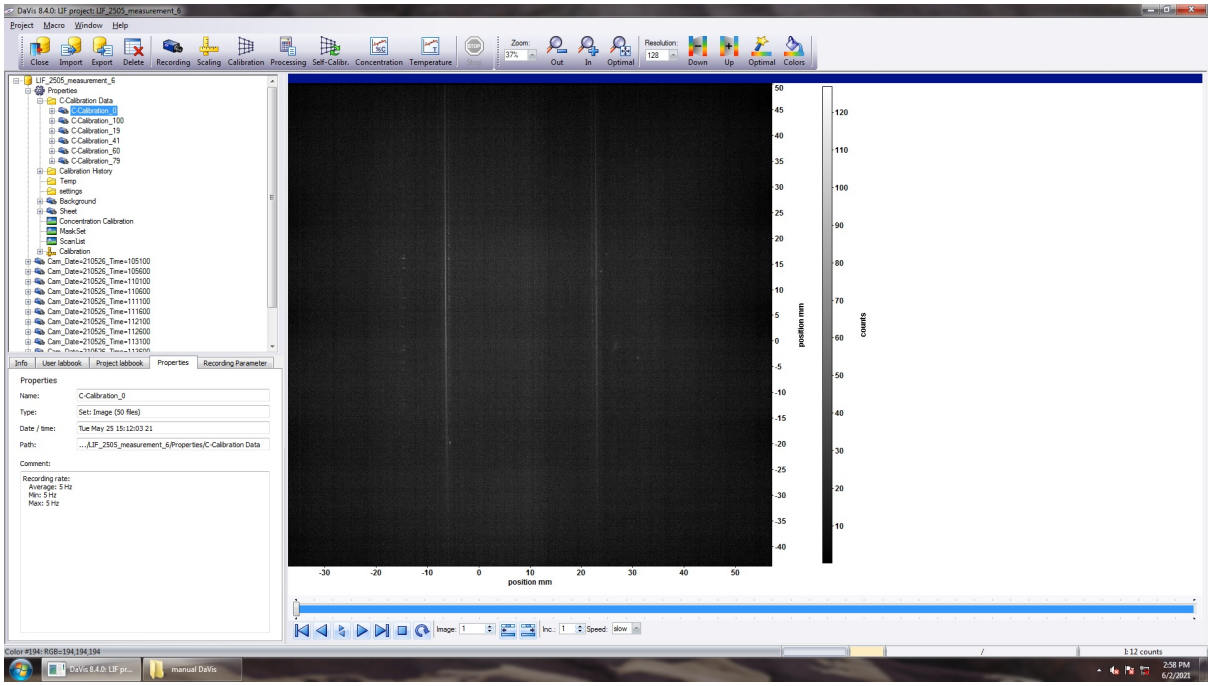

Figure A17

Now 20% of the particle solution is added to the column and either by bubbling or stirring the particles are mixed so that they distribute homogeneously in the fluid. When successful, repeat the image recording. You might find it useful to rename the different files so that it is clear which image recording corresponds to which relative concentration. An example of an image recording with 19% relative particle concentration is given in Figure A18. I always aim for 20% but sometimes it is difficult to achieve this.

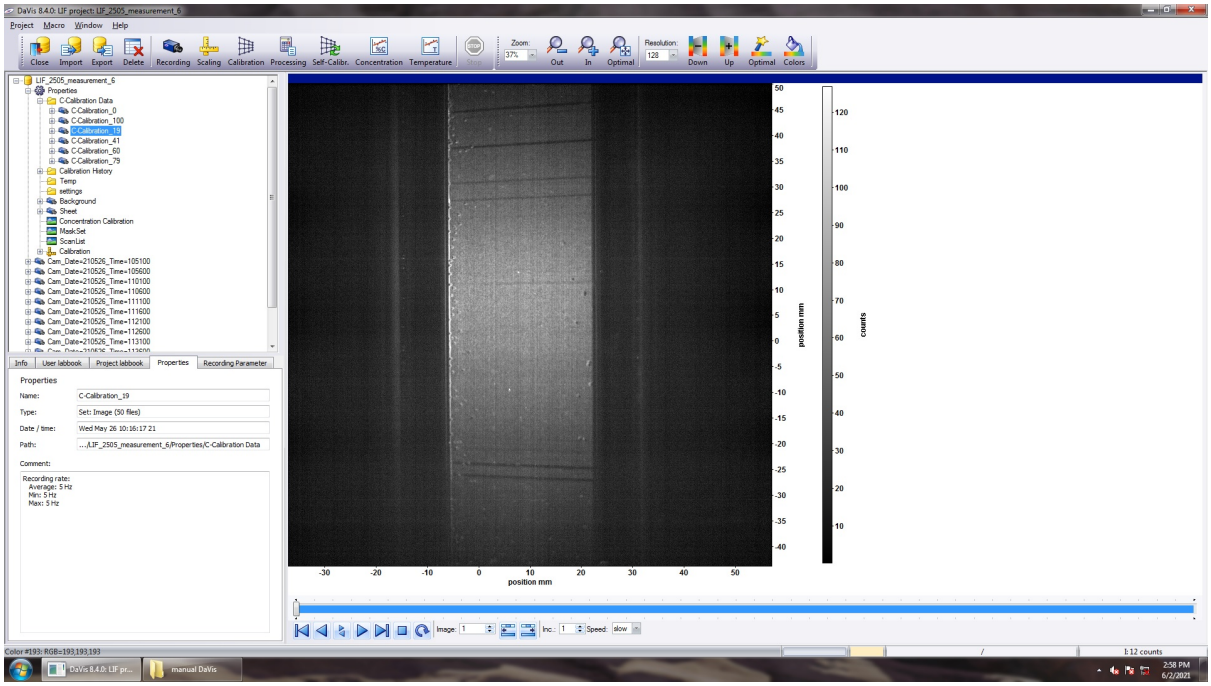

Figure A18

At this moment it is time to choose the IW. The IW is the area of the image that we are interested in, and it corresponds to the brightest part of the image. Select the 20% image and left-click on Concentration

in the bar at the top. This takes you to the menu as shown in Figure A19.

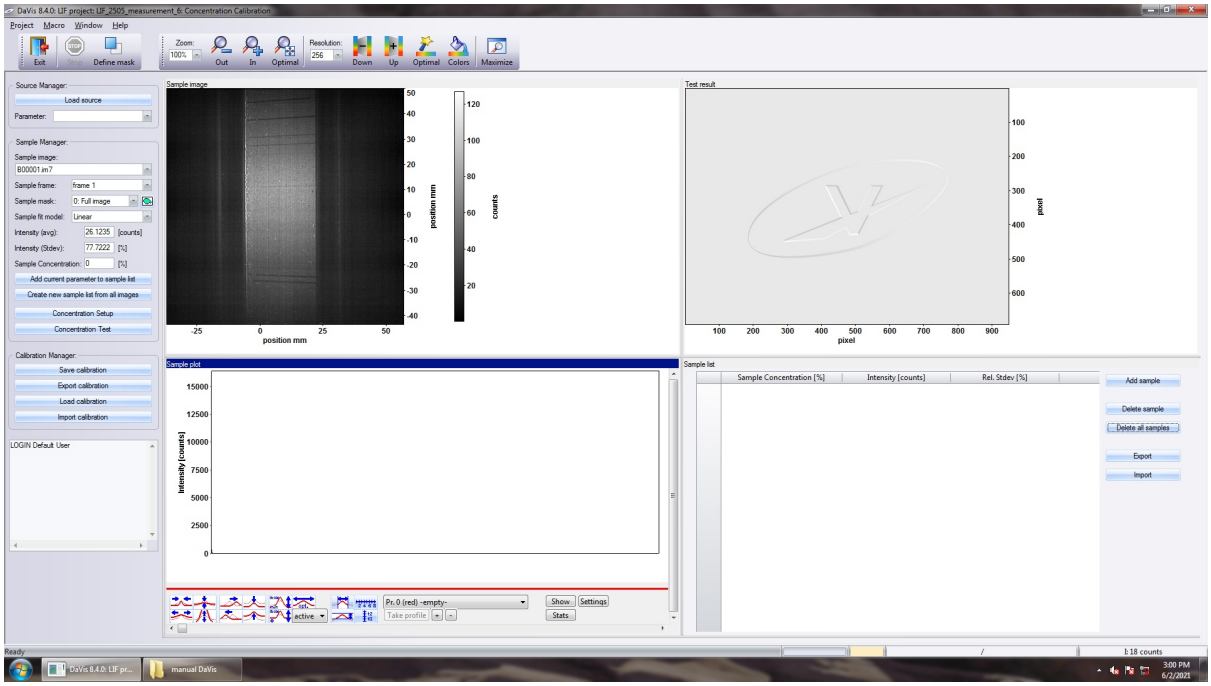

Figure A19

Click on Define mask and the resulting window is depicted in Figure A20. The mask that is chosen is essentially the IW.

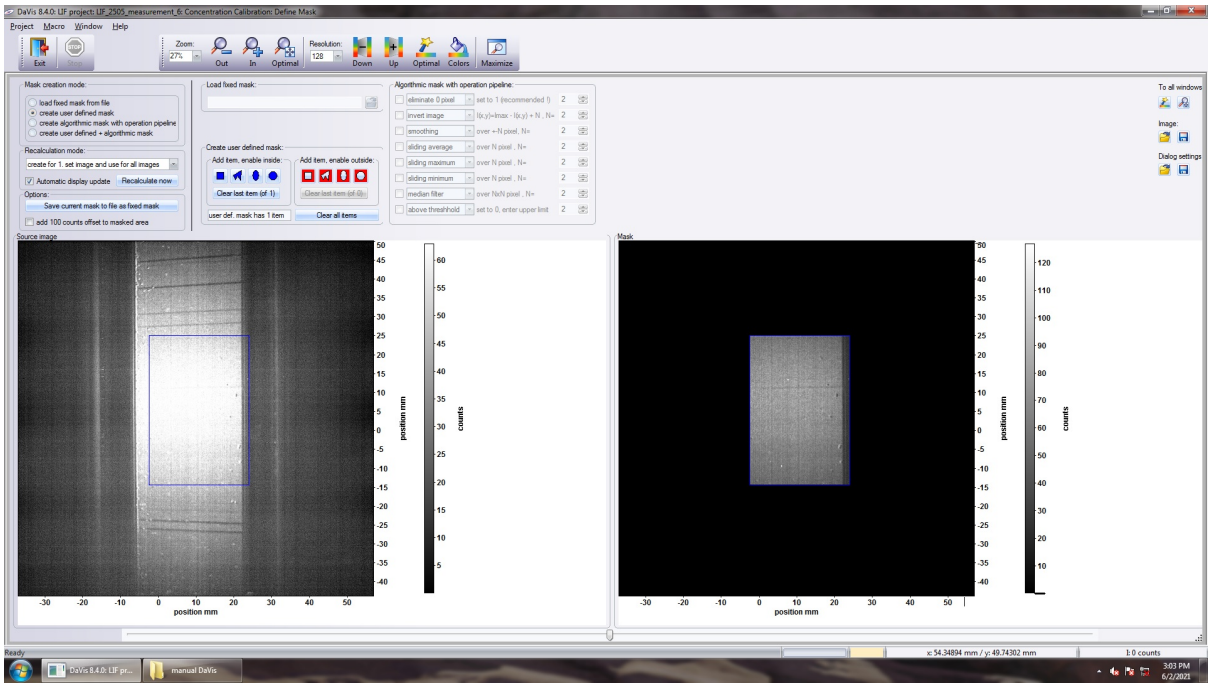

Figure A20

When a mask from a previous measurement appears, press Clear all items. Here the various icons display the preferred shape of the mask. For all experiments a rectangular mask is selected of size 4 cm by 2.5 cm in the area that lights up the most. To investigate this difference in contrast most clearly, the resolution can be changed at the top of the window by selecting Down. When satisfied with the result, left-click

on Exit and you will be asked to save the mask for this LIF project. You are taken back to the menu in Figure A21, but now the correct mask is displayed.

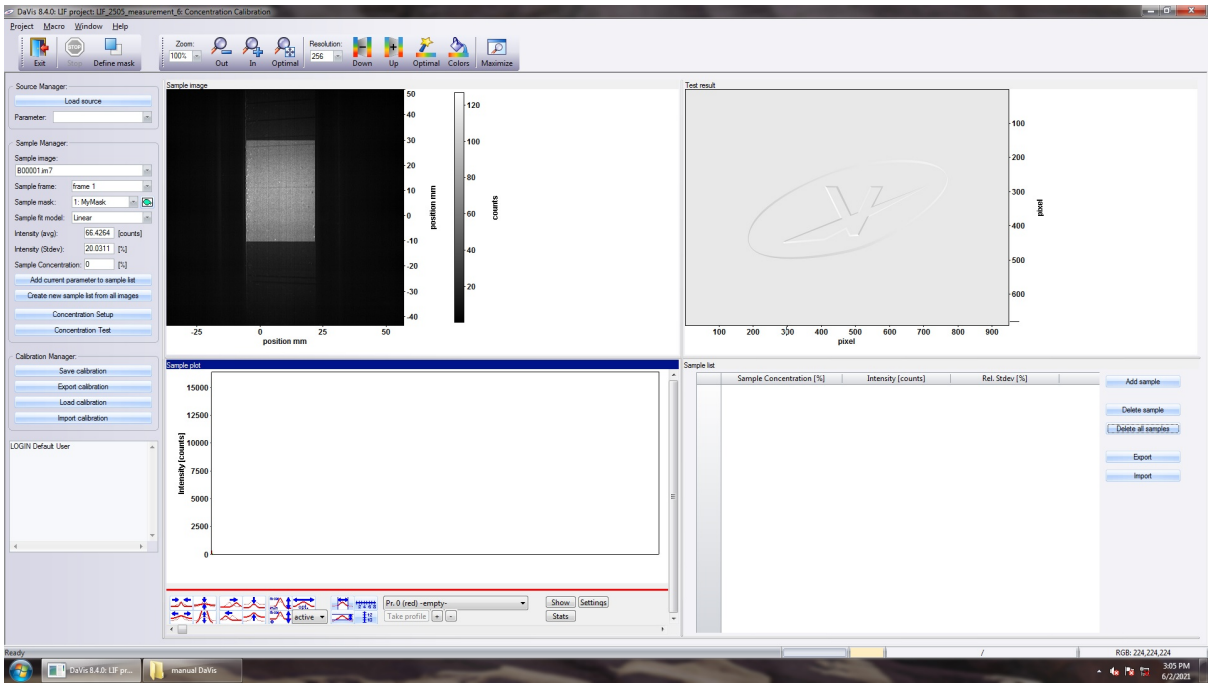

Figure A21

Press Exit again and you are taken back to Figure A22. Now that an IW is defined, processing of the calibration images can begin. Right-click on the image recording of choise and choose Processing.

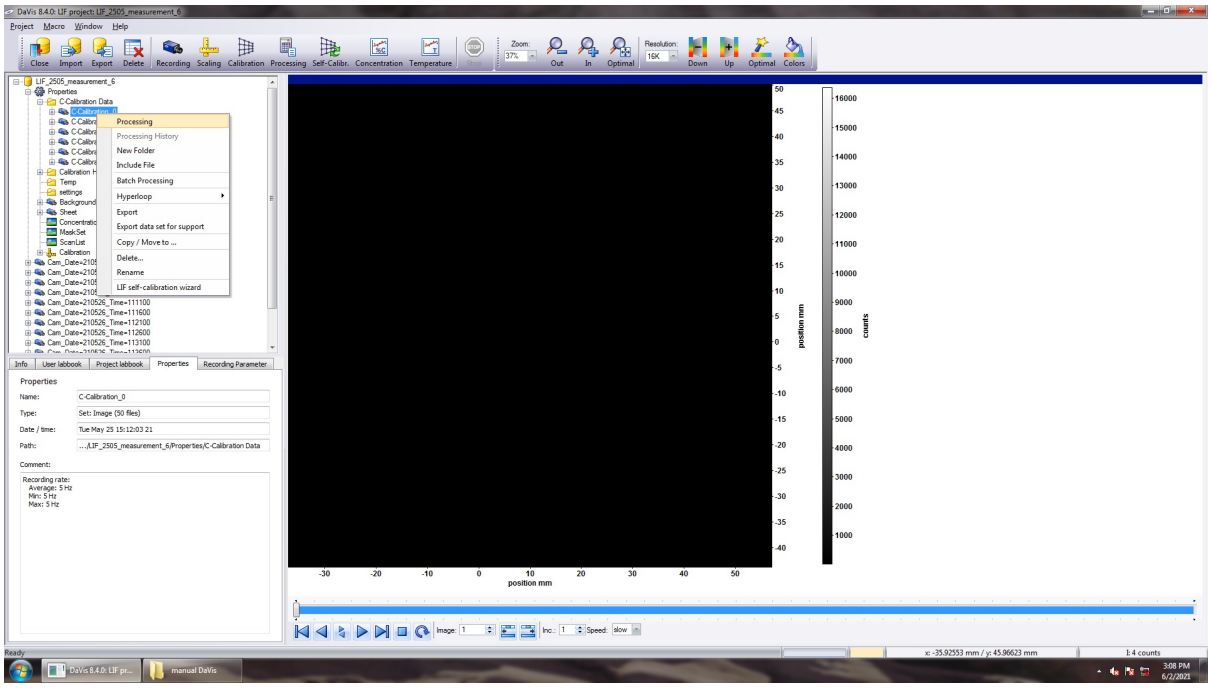

Figure A22

The three operations selected before remain to ensure averaging, background subtraction and sheet processing are utilized. The fourth operation that is necessary is image correction (raw → world) and

its location in the operation list becomes clear from Figure A23. This operation focuses the calculations on the mask area that was set previously. When ready, select Start Processing.

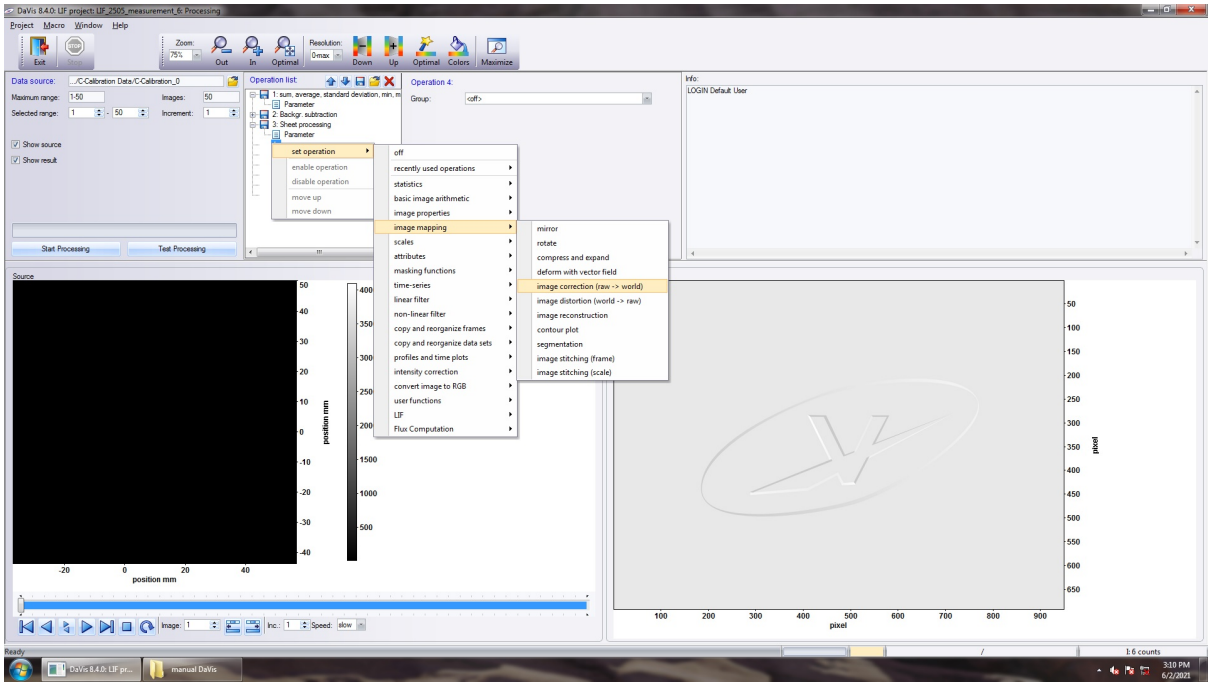

Figure A23

Press exit and head over to the file named Correction under the processed image recording folder, as shown in Figure A24. Left-click on it and then left-click on Concentration in the top bar. It is very important not to forget to select the Correction file, otherwise further calculations are performed on non- or wrongfully-processed images.

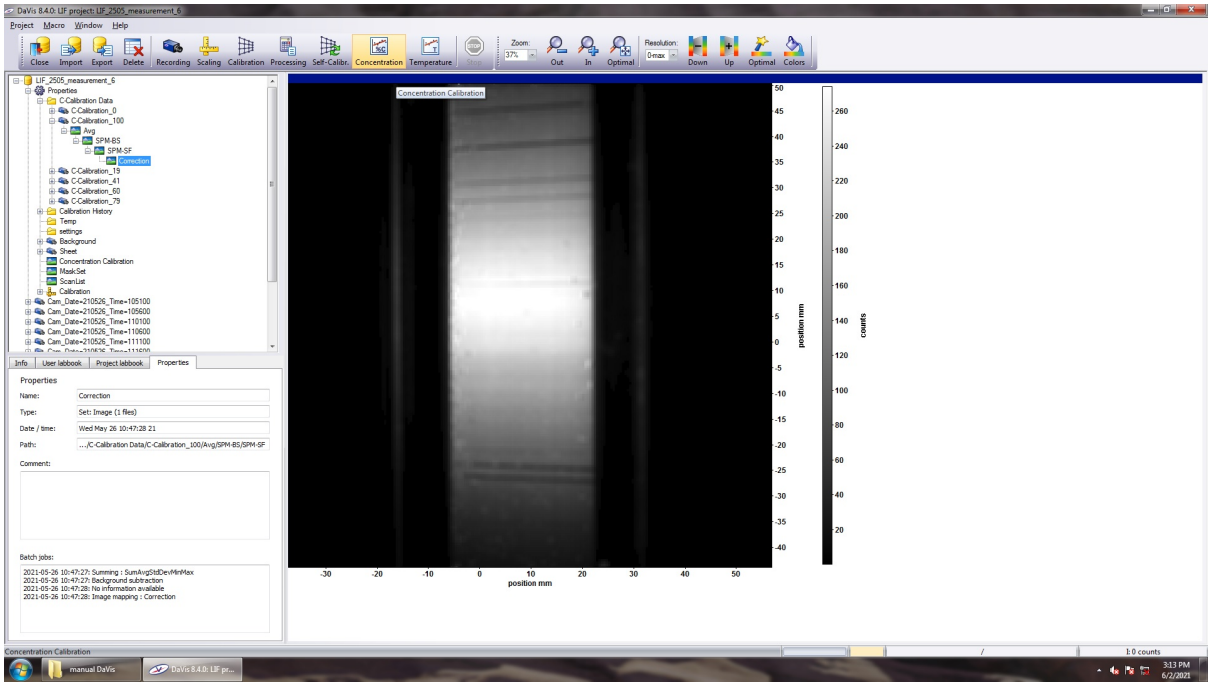

Figure A24

The window that appears is depicted in Figure A25. Here the intensity of the detected light is displayed

in counts, and also the standard deviation is provided. For the sample concentration, type the relative concentration value of the calibration measurement. Press Add the current sample to the sample list, and do this for all the calibration measurements. The program will than fit a linear calibration curve. Make sure to press Save calibration before pressing Exit otherwise the calibration is not saved.

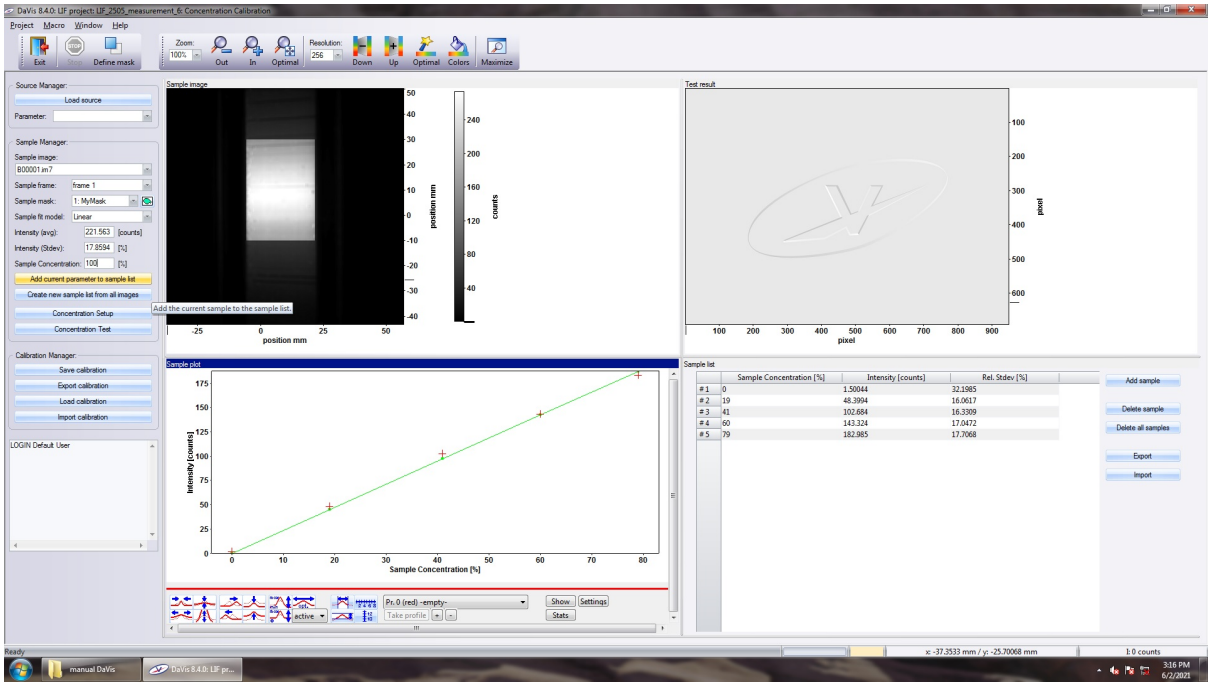

Figure A25

In the Properties folder, click on Concentration Calibration to view the data points and the fitted curve, as illustrated in Figure A26. This completes the calibration step.

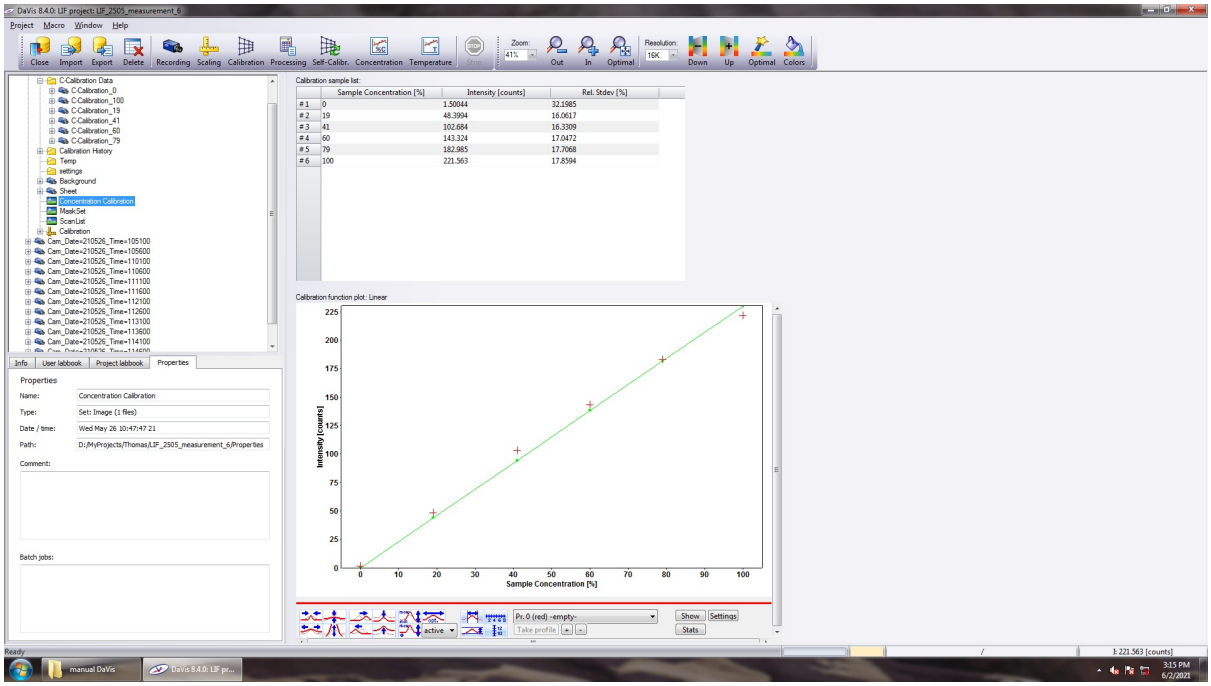

Figure A26

A.2.5 Experiment

With the calibration step complete, we are ready to carry out the experiment. Navigate to the Recording tab and select Experiment images from the Recording mode as in Figure A27. It is now possible to grab images of the experiment by clicking on the camera recording button. In my case, I decided to grab 100 images every 5 minutes to keep track of the particle concentration during the bubbling process.

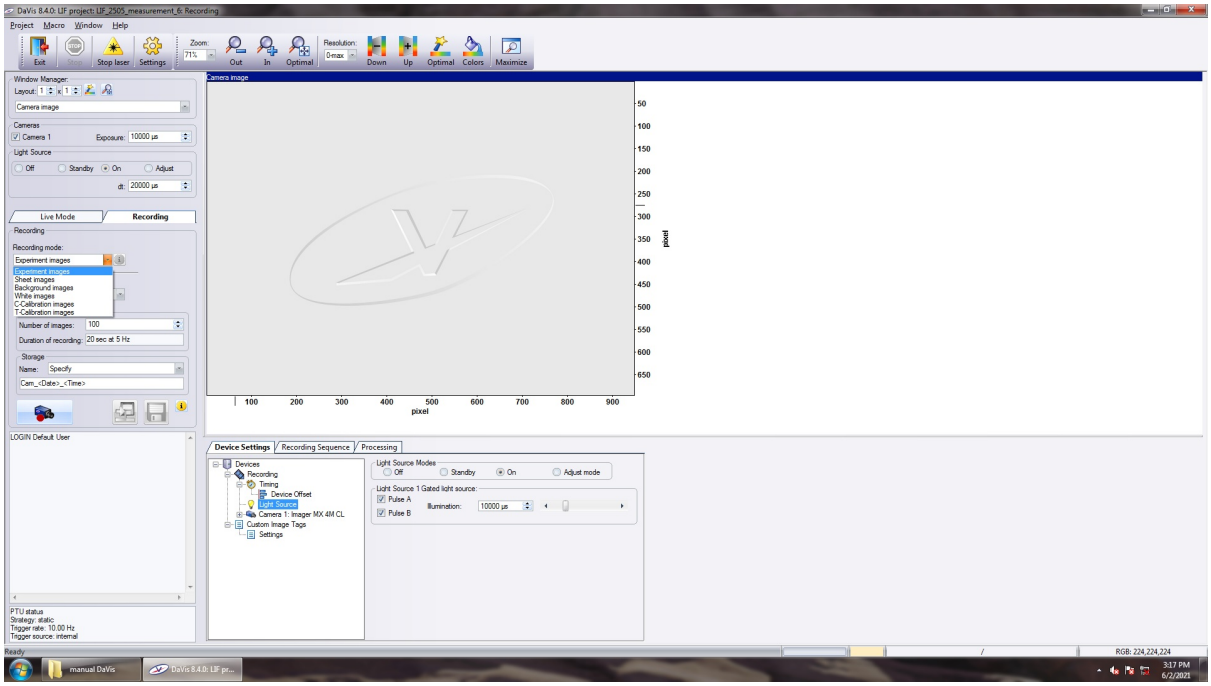

Figure A27

The image recordings are saved in separate folders in the LIF project, as becomes apparent from Figure A28. The shown image is an example of a picture taken during the measurement. Right-clicking on the experiment image recording and selecting Processing initiates the last step of the image processing sequence.

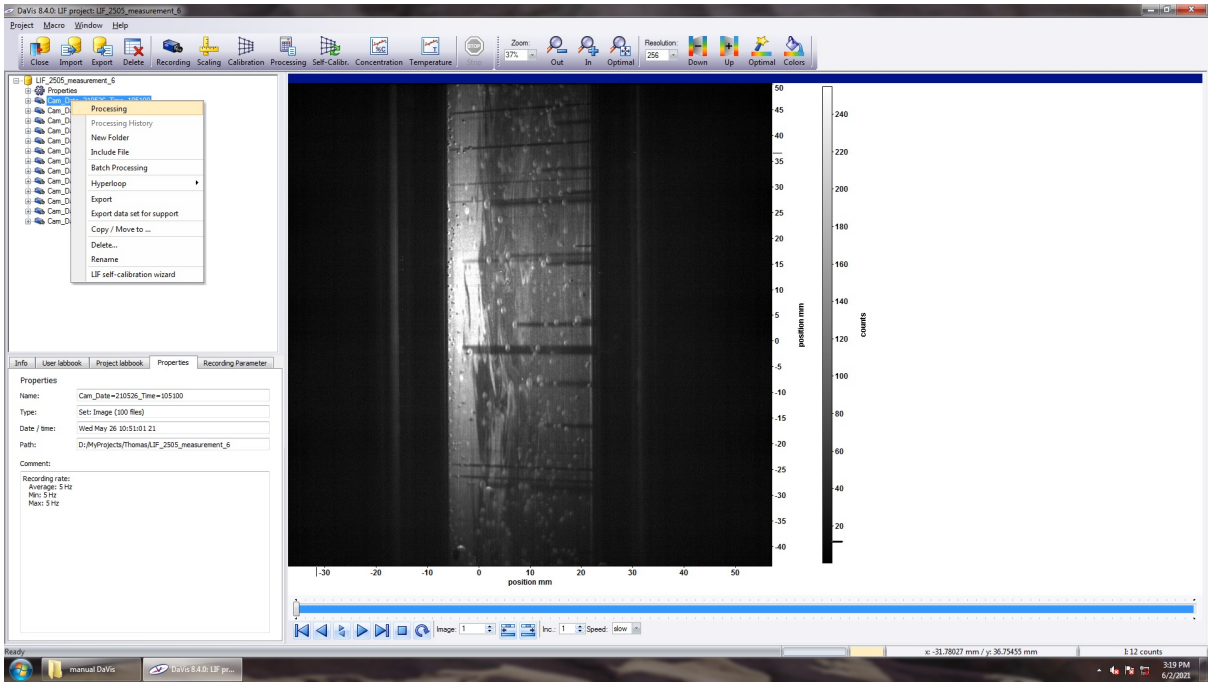

Figure A28

The resulting window is depicted in Figure A29. Right-click on the first operation and select disable operation. The reason for this is that, unlike for background subtraction, sheet processing and concentration calibration, all grabbed images need to be processed individually rather than calculating an average. This is a personal preference and helps to gain more insight in the concentration calculation process. The other three operations stay the same. Moreover, a fifth operation is added to the list, called Concentration Calculation, the location of which can also be found in Figure A29. This operation relates the measured intensity to the relative particle concentration.

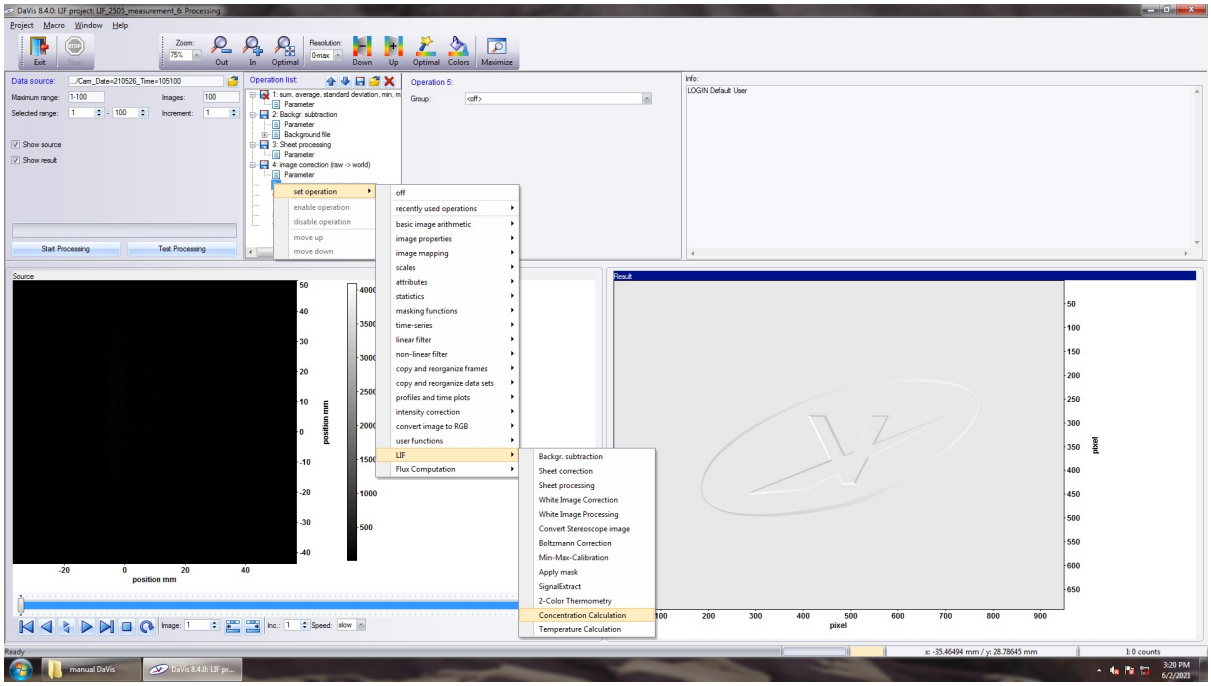

Figure A29

A sixth and final operation is required to nicely plot the data. Figure A30 shows where it is located.

After selecting the last operation, press Start Processing.

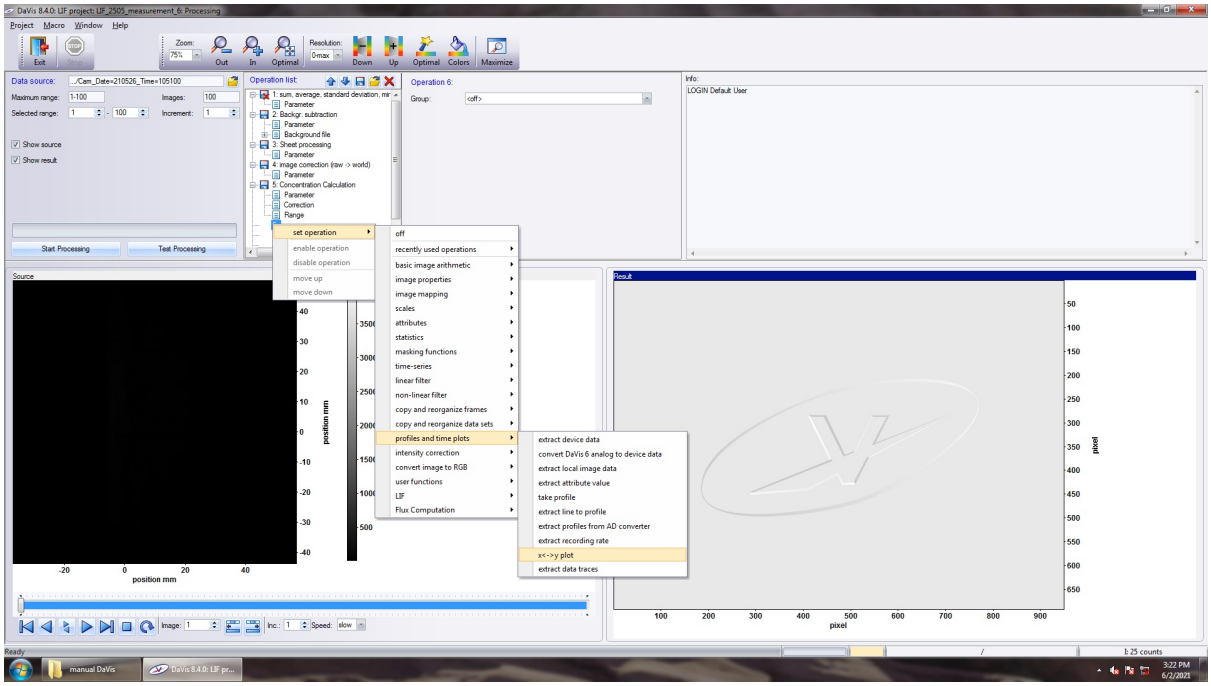

Figure A30

The x-y plot function can be found after pressing Exit and just like in the previous steps looking for the file (Plot_AvgRect_vs_file) in the experiment image recording folder, as shown in Figure A31. The plot relates the relative particle concentration to the number of grabbed images over time. Right-clicking on the file allows to choose the option Export.

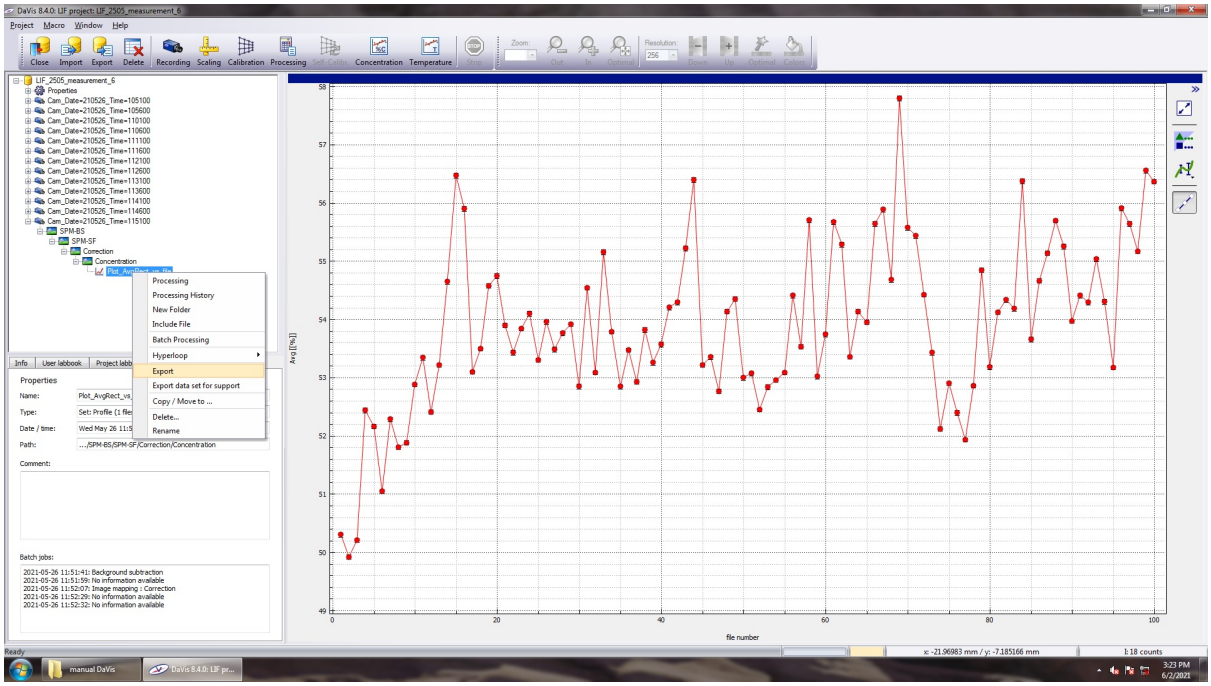

Figure A31

Finally, the data can be exported in any given format. The export type chosen saves the data of the measurement in a text file. This is illustrated in Figure A32. This allows for further analysis of the data.

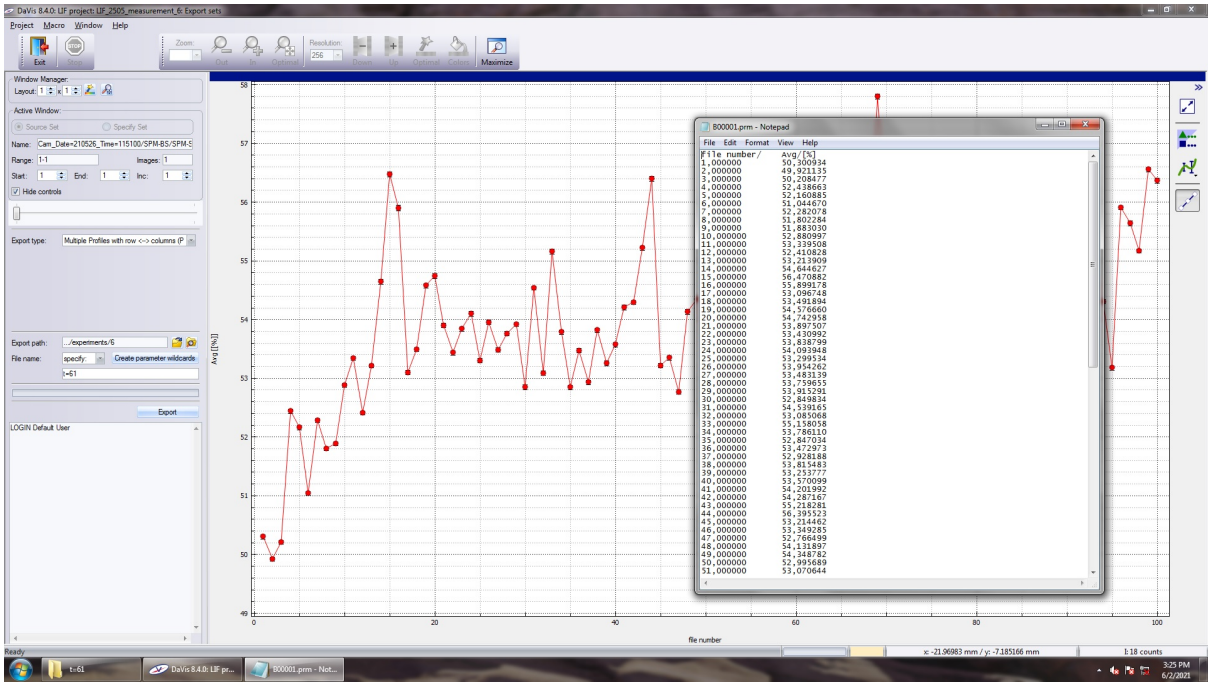

Figure A32

That concludes this rather lengthy guide of operation of the DaVis 8.4 software for concentration measurements using LIF. Hopefully this adds effectively to the LIF in Liquid Fluids manual [38] provided by LaVision. For more information regarding the precise steps taken during the above procedure the reader is referred to this manual.

A.3 Investigation of particle extraction

The purpose of this section is to show the MATLAB script that is used to quantify a relative particle concentration observed in the Hallimond tube before and after bubbling to study the efficiency of this device. The images that are loaded in are .bmp files. A mask is than defined to focus on the flask carrying the fluorescent particles. By means of thresholding the bright fluorescent particles are separated from the dark background and a relative particle concentration is established.

```
% Thresholding of concentrations in flasks to determine functionality of
    hallimond tube
clear all
listing = '<directory>';
FileNames = dir(char(fullfile(listing,'*.bmp')));%look for .bmp files
rect = [843 504 258 1300];%mask region for measurements
totalpxls = 259*1301;

%Preallocation
image = cell(length(FileNames),1);
imagecropped = cell(length(FileNames),1);
nonoise = cell(length(FileNames),1);

%Particle concentration algorithm
for i=1:length(FileNames)
  image{i,1} = imread(FileNames(i).name);%read all images in directory
  imagecropped{i,1} = imcrop(image{i},rect);%crop all images in directory

  %Remove noise
  noise = cell2mat(imagecropped(i,1));
```

```
    for layer=1:3
        removenoise(:,:,layer) = wiener2(noise(:,:,layer), [4 4]);%lowpass
            filters an intensity image that has been degraded by constant
            power additive noise
    end
    nonoise{i,1} = removenoise;

    %Convert to greyscale
    imagegrey{i,1} = rgb2gray(nonoise{i,1});

    %Thresholding
    [T(i,1),EM(i,1)] = graythresh(imagegrey{i,1});%threshold value T and
        effectiveness metric EM, which indicates the effectiveness of
        thresholding of the input image
    bw1{i,1} = imbinarize(imagegrey{i,1});

    %Seperate foreground and background
    bg(i,1) = sum(bw1{i,1}(:) == 0);%assign all values 0 to vector bg
    fg(i,1) = sum(bw1{i,1}(:) == 1);%assign all values 1 to vector fg
    ttlpxls(i,1)=bg(i,1)+fg(i,1);
end

%Show greyscale image
figure(1)
subplot(1,3,1)
imshow(imagecropped{1,1})
title('a')%Original Image

%Show image with removed noise
subplot(1,3,2)
imshow(imagegrey{1,1})
title('b')%Removed Noise Image

%Show thresholded image using Otsu's method
subplot(1,3,3)
imshow(bw1{1,1})
title('c')%Thresholded Image

%Average concentration (percentage of foreground pixels)
concentration = mean(fg)/totalpxls;

%Average effectiveness of thresholding on data set
eff = mean(EM);
```

B Drift flux model

The drift flux model introduced in Chapter 2 serves as an iterative scheme to determine the bubble rising velocity analytically. Following the derivation outlined in Chapter 2.1.2, a MATLAB script is provided on the performed calculations.

```
clear all
p_atm=1.01325*10^5;%atmospheric pressure [Pa]
rho_l=1032;%density of demineralized water at 20 degrees Celsius [kg / m3]
mu_l=0.891*10^(-3);%1.03*10^(-3);%dynamic viscosity of demineralized water
    at 20 degrees Celsius [Pa s]
g=9.80665;%gravitational acceleration on Earth [m / s2]
```

```
R_bottom=0.7160*10^(-3)/2;%average bubble radius measured [m]
y_bottom=0.605;%position in bubble column at bottom [m]
H=605*10^(-3);%height of bubble column [m]

C=(p_atm+rho_l*g*y_bottom)*4/3*pi*(R_bottom)^3;%constant from ideal gas law
    [J]

y=0;%position in bubble column (0 at top, 605 mm at bottom) [m]
R_b=(3*C./(4*pi*(p_atm+rho_l*g.*y))).^(1/3);%bubble radius as function of
    height y [m]

Re=109.0783;%initial bubble reynolds number [-]

if Re>0&&Re<=1%drag coefficient model [-]
    C_D=24/Re;
elseif Re>1&&Re<=400
    C_D=24/(Re)^(0.646);
elseif Re>=1000
    C_D=0.45;
end

v_b=sqrt(8*g*R_b/(3*C_D));%bubble rising velocity [m / s]
Re_b=rho_l*v_b*2.*R_b/mu_l;%bubble reynolds number [-]
t_b=H./v_b;%bubble rising time [s]
```

C Bubble-particle interaction model

In Chapter 2 the bubble-particle interaction model that is used to compare to experiments is explained. Furthermore, the results of the model are depicted in Figures 31 and 32. The curves displayed there follow the derivation outlined in Chapter 2.2 and the MATLAB script that speeds up the calculations is presented below for the case of the smallest investigated nanoparticles ($\overline{d_p} = 0.25$ µm) at a gas flow rate of 25 sccm.

```
%% comparison with the model
%Probabilistic model for bubble-particle attachment
%(modified Dobby-Finch model)

%% Attachment efficiency
v_p=0;%particle settling velocity [m / s]
v_b=0.0908;%bubble rising velocity [m / s]
R_p=0.25*10^(-6)/2;%particle radius [m]
R_b=0.716*10^(-3)/2;%bubble radius [m]
A=1.25;
B=0.6;
t_ind=A*(2*R_p)^B;%induction time (time required for bubble-particle
    attachment to occur) [s]
rho_p=1050;%particle density [kg / m3]
rho_l=1032;%liquid density [kg / m3]
mu_l=0.891*10^(-3);%liquid dynamic viscosity [Pa s]
K=2*rho_p*v_b*(R_p)^2/(9*mu_l*R_b);%Stokes number [-]
beta=4*R_p*rho_p/(3*K*R_b*(rho_p-rho_l));%dimensionless number
    characterizing particle collision [-]

%Attachment efficiency
E_a=(sin(2*atan(exp(-t_ind*(v_p+v_b)*(2+(R_b/(R_p+R_b))^3)/(2*(R_p+R_b))))
    )^2/(2*beta*(sqrt(1+beta^2)-beta));
```

```
%% Collision efficiency
E_0=3*R_p/R_b;%Sutherland efficiency [-]
K_3=K*(rho_p-rho_l)/rho_p;%normalized Stokes number [-]
theta_c=asin(sqrt((2*beta*(sqrt(1+beta^2)-beta))));%critical collision
    angle [rad]

%GSE (Generalised Sutherland Equation)/collision efficiency
E_c=E_0*(sin(theta_c))^2*exp(3*K_3*(cos(theta_c)*(log(3/E_0)-1.8)-(2+(cos(
    theta_c))^3-3*cos(theta_c))/(2*E_0*(sin(theta_c))^2)));

%% Stability efficiency
E_s=1;

%% Collection efficiency
E=E_a*E_c*E_s;



%% Particle recovery
Q=25*10^(-6)/60;%cm3/min to m3/s
A_c=pi*(25*10^(-3)/2)^2;
k=3*Q*E/(4*R_b*A_c);
R_0=41;
t2=linspace(1,3600,60);
R=R_0*(1-exp(-k*t2));


%plot of particle rate of recovery
figure(1)
hold on
plot(t2/60, R)
legend('Model')
xlabel('Time (min)')
ylabel('Recovery (%)')
xlim([0  61])
ylim([0  50])
title('Recovery of 250 nm particles')
hold off
```